



HAL
open science

Measurement of the Dark Energy Equation of State Using the Full SNLS Supernova Sample

Patrick El Hage

► **To cite this version:**

Patrick El Hage. Measurement of the Dark Energy Equation of State Using the Full SNLS Supernova Sample. *Cosmology and Extra-Galactic Astrophysics [astro-ph.CO]*. Université Pierre et Marie Curie - Paris VI, 2014. English. NNT : 2014PA066382 . tel-01127401

HAL Id: tel-01127401

<https://theses.hal.science/tel-01127401>

Submitted on 7 Mar 2015

HAL is a multi-disciplinary open access archive for the deposit and dissemination of scientific research documents, whether they are published or not. The documents may come from teaching and research institutions in France or abroad, or from public or private research centers.

L'archive ouverte pluridisciplinaire **HAL**, est destinée au dépôt et à la diffusion de documents scientifiques de niveau recherche, publiés ou non, émanant des établissements d'enseignement et de recherche français ou étrangers, des laboratoires publics ou privés.



DOCTORAL THESIS
OF THE UNIVERSITÉ PIERRE ET MARIE CURIE

presented by

Patrick El-Hage

To obtain the title of

DOCTEUR EN SCIENCES
DE L'UNIVERSITÉ PIERRE ET MARIE CURIE

Measurement of the Dark Energy Equation of State Using the Full SNLS Supernova Sample

To be defended to the following jury on September 26th, 2014 :

Julien	GUY	Thesis advisor
Rick	KESSLER	Referee
Emmanuel	BERTIN	Referee
Christophe	YÈCHE	Examiner
Jacques	DELABROUILLE	Examiner
Michael	JOYCE	Examiner
Reynald	PAIN	Guest



A little knowledge that acts is worth infinitely more than much knowledge that is idle.
Gibran Khalil Gibran

Acknowledgements

My journey at the **Laboratoire de Physique Nucléaire et de Hautes Énergies** (LPNHE) began a few months before my thesis did, during my Master's degree (NPAC) internship. My first memories at the laboratory are those of Julien Guy and Pierre Astier talking over each other in an attempt to explain to me the objectives of my internship. In the short hour I spent with them, I was bombarded with details on topics ranging from supernova cosmology as a whole to the finer details of manipulating a Fisher matrix for optimization purposes. Needless to say, I left that office confused and intimidated. That meeting, however, set the tone for the next 3 years of my life, in that the LPNHE cosmology team would treat me not as an underling but as a colleague, albeit a slightly inexperienced one.

After that first encounter with the dynamic duo of French cosmology, my circle of collaborators would only grow. While my own research often focused on minute technical details, I could always count on the rest of the group for friendly discussions regarding broader topics in cosmology. Here I would like to thank in particular Pierre Astier, Nicolas Regnault, Sébastien Bongard, Laurent Le Guillou, and Augustin Guyonnet for the time they took in imparting some of their technical expertise regarding the bigger picture of supernova cosmology. I would also like to thank Reynald Pain, our fearless leader, for his wisdom regarding the challenges and outlooks of being a graduate student and his frank discussions of the current state of fundamental physics.

As time progressed, so too did my responsibilities as a member of the SNLS collaboration. As the third year of my thesis came around, it was time for me to process and analyze the final SNLS supernova sample. Here I must extend my sincerest gratitude to Marc Betoule for his time, patience, and software, all of which greatly facilitated this part of my research. In particular, by exploiting his previous experience with the JLA analysis he allowed me to focus my attention on the more pressing scientific questions I was facing rather than spend time dealing with pipeline issues. His help in this regard was so significant that I was even willing to overlook his unintelligible code writing style. Here I would also like to thank Delphine Hardin and Christophe Balland for their crucial help in core aspects of the SNLS analysis, in particular for having adapted their timelines to my thesis requirements despite their exceedingly busy schedules.

Throughout it all, there was my advisor, Julien Guy, whose enthusiasm for science and all its gory details can only be described as infectious. During our time together he has done more than merely invigorate my passion for cosmology, though he has certainly done that as well. I knew that I was always welcome in his office, and as such we would regularly discuss matters ranging from the direction of my thesis to the optimal choice of revision control software for our next project. Indeed, we regularly spent hours on the same computer screen, often times even passing the keyboard back and forth to each other. In those moments he imparted upon me a

work method that will stay with me well beyond my years as a graduate student. While a love of science is commonplace, Julien has taught me how to love details without drowning in them, and how to appreciate the importance of expertise without ever forgetting the bigger picture.

I would like to add that while Julien was my official thesis advisor, both Marc Betoule and Pierre Astier were also a constant source of support during my thesis, despite having no formal obligations towards me whatsoever. In addition, help came from well beyond the walls of the LPNHE, as the many international researchers I had the opportunity to collaborate with proved to be a rich source of intellectual stimulation. In particular, I would like to thank Rick Kessler for his warm welcome during my visit to Chicago.

Beyond the cosmology team, there were many people that made the LPNHE the welcoming environment that it was. I would like to thank Véronique Joisin, Vera Varanda, and Magali Carlosse for their organizational efforts which make the life of an LPNHE researcher possible, as well as François Legrand, our systems administrator, for always helping me out when I was in a bind. During my years at the LPNHE, Eli Benhaim was my graduate “godfather”, a job he took very seriously by regularly checking up on me to ensure that all was well. He provided me with a safe space to air both my joys and my concerns with regards to the progress of my thesis, and for that I am very grateful. I would also like to thank Sophie Trincaz-Duvoid both for her help during my Master’s degree, as well as the support she shows all graduate students of the LPNHE.

Of course, no graduate student experience would be complete without other graduate students who suffer alongside you. I would likely not have survived these last 3 years were it not for the friendship and solidarity of my fellow NPAC graduates, as well as the students I befriended along the way. While it may have led to a diploma, it would have been a sad thesis indeed without the cheerfulness of Guillaume Lefebvre, Aurélien Demilly, Pierre Morfouce, Agnès Ferté, Matthieu Roman, and Tania Garrigoux.

I would not have even contemplated pursuing my passion without the constant support of my family. I would not be the passionate geek I am today were it not for my brother and the childhood we spent building legos together. Today, my sister is the biggest fan of my work, despite not understanding much of it, and I am eternally grateful for her fascination with the universe which serves to remind me of the ultimate purpose of scientific pursuits. Of course, were it not for my parent’s encouragement that I pursue my dreams regardless of how odd they seemed to those around me, the very concept of becoming a cosmologist would not have even occurred to me. And while we may not be technically related, Raja Salamé’s unwavering friendship is what has allowed me to enjoy the ride in this pursuit, and to me that makes him as good as family.

This pursuit was also greatly aided by a number of scholarships. The first of these was the Philippe Jabre scholarship which allowed me to attend the Research Science Institute at MIT while still in high school. The second was the Fayez Sarofim Scholarship which covered the complete cost of my undergraduate tuition while at Rice University. And finally, the last of these was the French government grant that made this thesis possible. I will strive for a career as a researcher that lives up to the expectations of these financial benefactors.

Also during that pursuit, I encountered many professors which played a crucial role in making me the person I am today. I will start by thanking Jean Baptiste Fourest, my middle school math teacher, for teaching me that a passion in life is something to be treasured and nurtured. I would then like to thank professor Paul Padley for introducing me to the world of research by granting me the opportunity to work at CERN for a summer, as well as his willingness to talk about life and all things physics during his invaluable office hours. I would also like to thank

everyone at NPAC, teachers, students, and administrators, for making me feel so welcome when I first got to France, as well as for their availability in my times of need.

Last, and most certainly not least, special mention must be made of the role Laura Cottard played in shaping my academic career. Had I not decided to follow her to France after graduating from Rice University, I would not have discovered NPAC. Had I not discovered NPAC, I would not have discovered cosmology, the field that I was always meant to pursue. Had I not pursued cosmology, I would have likely ended up in the field of particle physics, or worse yet in applied physics. On the whole it goes to show that even when it tells you to cross an ocean, your heart always knows best.

Acknowledgements

Contents

Introduction	1
1 Physical Cosmology and the Acceleration of Expansion	3
1.1 A Historical Overview of Relativity	3
1.1.1 Galilean Relativity	3
1.1.2 Special Relativity	4
1.1.3 General Relativity	5
1.2 Theoretical Basis of Modern Cosmology	7
1.2.1 The Friedmann Equations	7
1.2.2 Cosmological Redshift	9
1.2.3 The Hubble Diagram	10
1.3 Constructing the Λ CDM Model	11
1.3.1 On the Astrophysical Need for Dark Matter	11
1.3.2 The First Acceleration Observations From SN	12
1.3.3 Concordance With Other Probes	13
1.4 Theoretical Explanations of Observations	17
1.4.1 Corrections to General Relativity	18
1.4.2 The Impact of Inhomogeneities	18
1.4.3 Quintessence Models	19
2 Supernovae as Standard Candles	21
2.1 Empirical Properties of SNIa	21
2.1.1 Spectroscopic Properties	21
2.1.2 Photometric Properties	23
2.1.3 Peculiar SNIa	24
2.2 Proposed Physical Mechanisms	25
2.2.1 The Single Degenerate Model	26
2.2.2 The Double Degenerate Model	26
2.3 SNIa Modeling	27
2.3.1 Standardizing the Distance Modulus	27
2.3.2 On the Need for K-Corrections	27
2.3.3 Overview of Model Training	29
2.3.4 Accounting for Data Holes	30
2.4 Hints of New Standardization Parameters	33
2.4.1 Spectroscopic Correlations	33
2.4.2 Galaxy Dependence	33

3	Overview of the Supernova Legacy Survey	35
3.1	Overview of the Science Analysis	35
3.1.1	Photometry in Different Bands	35
3.1.2	The SALT2 Light Curve Fitter	36
3.1.3	The Cosmology Fit	36
3.2	The CFHT Legacy Survey	36
3.2.1	The “Very Wide” Survey	37
3.2.2	The “Wide” Survey	37
3.2.3	The “Deep” Survey	37
3.3	Observation Strategy	38
3.3.1	A Rolling Search	38
3.3.2	Spectroscopic Follow Up	39
3.4	MegaPrime	41
3.4.1	The Upper End	41
3.4.2	Wide Field Corrector	41
3.4.3	Image Stabilizing Unit	42
3.4.4	Guiding and Focus	42
3.4.5	MegaCam	42
3.4.6	Around MegaCam	43
3.4.7	Modeling the Optical Path	43
3.5	Overview of the Data Flow	45
3.5.1	Preprocessing at CFHT	45
3.5.2	Local Processing	46
4	PSF Photometry of Dim Supernovae	49
4.1	Local Image Preprocessing	49
4.1.1	Sky Subtraction	49
4.1.2	Star Catalog	50
4.1.3	PSF fitting	51
4.1.4	Astrometry	51
4.2	Direct Simultaneous Photometry	53
4.2.1	Algorithm	53
4.2.2	Preserving Linearity	54
4.2.3	Effects of Refraction	56
4.3	Validations with simulations	57
4.3.1	Simulation goals	57
4.3.2	Simulation method	58
4.3.3	Expected biases	59
4.3.4	Simulation parameters	60
4.3.5	Results	61
5	Photometric Calibration of the SNLS Supernova Sample	67
5.1	Calibrating Supernova Measurements	67
5.1.1	An Introduction to Photometric Calibration	67
5.1.2	The SNLS Magnitude System	69
5.2	Instrument Response Model	70
5.2.1	Transmission Model	70
5.2.2	Filter Measurements	71

5.3	Zero Point computation	73
5.3.1	Sky Pollution Bias	74
5.3.2	Chromatic PSF Bias	76
5.3.3	Results of Calibration uncertainty	78
6	Cosmology Analysis	81
6.1	Supernova Sample Selection	81
6.1.1	SALT2 Training Sample	82
6.1.2	For Cosmology	82
6.1.3	Flux Convention	84
6.2	Lightcurve Parameter Extraction	84
6.2.1	Results of the SALT2 Model	84
6.2.2	Lightcurve Fitting	85
6.2.3	Simulating the SALT2 Uncertainty	86
6.3	Corrections	89
6.3.1	Host Galaxy Mass Corrections	89
6.3.2	Peculiar Velocity Corrections	92
6.3.3	Malmquist Bias Correction	93
6.3.4	Dust Correction	94
6.4	Fitting the Hubble Diagram	95
6.4.1	Correlated Calibration Systematics	95
6.4.2	Determining σ_{coh}	95
6.4.3	Constraints from Other Cosmological Probes	96
6.4.4	Overview of the Fit Method	97
6.5	Cosmological Results	99
6.5.1	A Blinded Analysis	99
6.5.2	Comparison with JLA Analysis	100
6.5.3	Impact of Corrections	100
6.5.4	Preliminary Analysis Results	101
	Conclusion	105
	Appendices	107
	Appendices	
	A The Supernova Database	109
	B Zero Point Robustification	111
	Bibliography	133

List of figures

- 1.1 Here we plot the observed flux of an object as a function of the redshift at which its light was emitted, for different cosmology models. The dashed line corresponds to a flat matter dominated universe in which there is no acceleration. The solid line corresponds an accelerating expansion, similar to actual observations. . . . 11
- 1.2 The density profile required to explain the observations implies the presence of significant amounts of missing mass. 12
- 1.3 Cosmological results using the luminosity distance estimates of [Perlmutter et al. \(1999\)](#). 14
- 1.4 Map of CMB temperature anisotropies as seen by Planck. The central regions correspond to the galactic plane and are mostly excluded from cosmological analysis. 15
- 1.5 Uncertainty contours of the JLA analysis. “Planck” represents CMB temperature data, “WP” represents CMB polarization data, and “BAO” represents BAO data. Note that in both parameter spaces, the 2 contours are nearly perpendicular and greatly compliment each other. 17
- 1.6 Uncertainty contours in the w VS w_a plane provided by the JLA analysis. w_a is almost completely unconstrained. 20

- 2.1 Spectroscopic properties of a typical SNIa. Note that the emitted flux peaks in the blue band. For this reason, we establish the convention that the integrated flux in this band is to be used when comparing supernovae. 22
- 2.2 Typical supernova lightcurve, before and after model fitting, of supernova 03D4ag from the SNLS5 analysis. Note the second smaller peak in the redder i and z bands. 23
- 2.3 The 2 most visible correlations between SNIa brightness and lightcurve properties. 24
- 2.4 Spectra and light-curves of peculiar SNIa relative to normal SNIa. The differences between the two are less obvious then between Ia and non-Ia supernovae, but are still significant enough to be distinguished after careful consideration of all the information at hand. 25
- 2.5 Total transmission functions for the 5 filters that describe the SNLS data. T_a is the atmospheric transmission function, T_m is the instrument transmission function, T_0 is the filter transmission function, and ϵ is the quantum efficiency of the CCD. The total transmission function is the product of all of these. 28
- 2.6 30

- 3.1 The objective is to compare the supernova fluxes highlighted in blue. The left hand figure shows us how to calibrate fluxes, whereas the right hand figure shows the necessity of a spectrophotometric model of SNIa. 36
- 3.2 Location of the wide and deep fields in the night sky. 37

3.3	SNIa candidates, detected between May 2004 and January 2006, and their brightness in g, r, or i band as a function of time.	40
3.4	Telescopes used for spectroscopic confirmation of SNIa candidates for the SNLS.	41
3.5	The MegaPrime instrument (from the CFHTLS website).	42
3.6	Arrangement and numbering scheme of the CCD mosaic. A and B correspond to the 2 amplifiers used during readout. Taken from Terapix	44
3.7	Effective model of the optical path within the MegaPrime instrument. The model's free parameters include the properties of each lens, the distance from one lens to the next, and also an offset between the lens center and the central axis, in order to model the impact of misalignment of the various components. Taken from Villa (2012)	44
3.8	Example of the end result on the CCD of illumination of the focal plane by a given LED. The deformed square near the middle is the result of inner reflections. Taken from Villa (2012)	45
4.1	Gaussian-weighted second moments from a single typical image, with the found star clump and the star selection (red points within the ellipse).	50
4.2	Astrometric 1-D residuals scatter as a function of star magnitude for the D3 field in <i>r</i> band. The top plot compares, as a function of magnitude, the measured residual RMS (points) with the average expected RMS (curve) including a noise floor of 0.013 pixels. They are roughly compatible, but not necessarily equal because the expected RMS varies with IQ at fixed magnitude. The bottom plot displays the RMS of the residual pulls (i.e. residuals in unit of expected RMS), which are close to 1 at all magnitudes. We hence conclude that adding the position noise floor of 0.013 pixels (2.4 mas) in quadrature to the position uncertainty expected from shot noise fairly describes the residuals. This figure only considers residuals along <i>y</i> for reasons explained in section § 4.2.3.	53
4.3	57
4.4	Above are density plots comparing the distribution of real supernovae and simulated fake stars in the plane of <i>S/N</i> of the supernova lightcurve VS the ratio of the galaxy flux to the supernova flux at maximum.	60
4.5	Photometric factor accuracy as a function of <i>S/N</i> for the RSP method. We have binned the estimated \hat{r}/r in <i>S/N</i> bins. We plot both the uncertainty on the bin mean as well as the dispersion in the bin so as to compare it to the expected dispersion at that <i>S/N</i> . We also plot the expected <i>S/N</i> bias, as well the obtained fit for equation 4.14.	62
4.6	Photometric factor accuracy as a function of <i>S/N</i> for the DSP method. We have binned the estimated \hat{r}/r in <i>S/N</i> bins. We plot both the uncertainty on the bin mean as well as the dispersion in the bin so as to compare it to the expected dispersion at that <i>S/N</i> . We also plot the expected <i>S/N</i> bias, as well the obtained fit for equation 4.14.	62
4.7	63
4.8	Standard deviation of flux estimates over the lightcurve as a function of the average flux. The relation is shown here for high-flux field stars, and we see a clear linear relationship, indicative of a contribution to scatter beyond shot noise from the sky and the object.	64

4.9	We plot here the ratio of the modeled uncertainty to the RMS of the light curve, as a function of the sum of the fluxes of the fake star and galaxy. The two set of points refer to before and after adding a β term to the model uncertainty (Eq. 4.16). We see that the correction makes only a small difference.	64
4.10	Evolution of χ^2/N_{dof} of night fits of real SNe as a function of redshift.	65
4.11	We consider the error in the fitted position in units of σ_{IQ} as a function of the S/N ratio. We also plot the expected relation between the two using equation 4.17.	66
4.12	To fit the form factor, we fit a slope in the r^2 VS flux bias plane, where r is the error on the position. Each black point represents the computed bias using equation 4.18 for a random position on the image and a random displacement across it.	66
5.1	The solid black lines represent the old calibration transfer scheme, as described in Regnault et al. (2009). The dotted red lines represent the work done in Betoule et al. (2013). The instrument names indicate that both sets of stars were observed with the said instrument, hence making flux calibration transfer possible.	70
5.2	Relative corrections to the twilight flat fields due to grid corrections.	71
5.3	Overview of the MegaPrime photometric response analysis. Boxes describe the various data sets involved in the construction of the model (dashed for external data). Ellipses represent the main steps of the analysis. Taken from Betoule et al. (2013). Using the lessons learned from surveys such as SNLS and SDSS, newer surveys such as DES and LSST will regularly measure the combined impact of the optics, the filters, and the CCDs rather than dealing with them separately.	72
5.4	Filter induced color dependence of magnitudes at 17cm from focal center in u, g, r, i, i2, and z bands.	73
5.5	Ratio of the fitted sky level to the flux of the star as a function of color, for high flux stars only in i band. For such stars we assume that the fitted sky level is predominantly a fraction of the flux incorrectly fitted as the sky level. We see that the fraction of flux that goes into our sky level estimator evolves linearly with color.	75
5.6	Plot of zero point residual vs magnitude in i band, before and after correcting for aperture sky pollutions.	76
5.7	Comparison of data with Pickles (1998) spectroscopic library in order to fit an appropriate effective filter, in g band.	78
6.1	Distribution of the full supernova sample (before cuts).	83
6.2	85
6.3	Evolution of standardization parameters as a function of redshift.	87
6.4	Diagrammatic overview of the simulation process. We begin by choosing the underlying input models for both the cosmology and the supernovae. This produces two sets of supernovae : one for SALT2 training, and one for cosmology. Once the training is complete, distance moduli are computed for the cosmology set. In turn, we correct these moduli for Malmquist bias, and fit a cosmology to them. We can then compare the input and output values of the cosmological parameters, in particular w	88
6.5	Difference between input and recovered distance moduli for various input models. The first two entries in the model name describe the input spectral and intrinsic scatter models. The last two indicate that a “real” training set was used.	89

6.6	Fitting galaxy mass VS K_S magnitudes.	91
6.7	Hubble residuals as a function of galaxy mass, before any correction is applied, as obtained in the JLA analysis.	91
6.8	Expected Malmquist bias for each survey as a function of redshift. The smaller error bars represent the Monte Carlo statistical limitation alone, while the larger ones include the uncertainty on the selection function. Taken from Betoule et al. (2014)	94
6.9	In order of redshift, the samples are the low-z subsample at $z < 0.03$ and $z > 0.03$, the SDSS subsample at $z < 0.2$ and $z > 0.2$, the SNLS subsample at $z < 0.5$ and $z > 0.5$, and the HST subsample. Despite appearances, the points are consistent with a redshift independent σ_{coh}	96
6.10	Confidence contours of the nuisance parameters and Ω_m . Note that the contours in nuisance parameter VS Ω_m space lack significant diagonal tilts.	99
6.11	Histogram of difference in Hubble residual relative to JLA uncertainty, in absolute value.	100
6.12	Distribution of the full supernova sample (before cuts).	102
6.13	Expected uncertainty on w for various scenarios computed using an artificial Fisher matrix. The x-axis represents a change in the zero point uncertainty in all bands. The solid lines represent the statistical uncertainty on w for various color coded data samples : black corresponds to the SNLS3 data sample, red corresponds to the addition of the final SNLS and SDSS data, and green represents the addition of 300 low redshift supernovae. Points 1 and 2 represent the SNLS3 analysis, before and after recalibration. Points 5 and 3 represent the addition of new supernovae to both the SNLS and SDSS samples, again before and after recalibration. Point 4 represents the addition of new low-z data, after recalibration.	103
B.1	Example of cuts for a single zero point fit.	112
B.2	Scatter plot of calibration stars for field D1	114
B.3	Residuals of zero point for cut aperture photometry quality	115
B.4	Distribution in magnitude for cut aperture photometry quality	116
B.5	Residuals of zero point for cut saturation suspect	117
B.6	Distribution in magnitude for cut saturation suspect	118
B.7	Residuals of zero point for cut excessive clipping in flux average	119
B.8	Distribution in magnitude for cut excessive clipping in flux average	120
B.9	Residuals of zero point for cut aperture bias npoints	121
B.10	Distribution in magnitude for cut aperture bias npoints	122
B.11	Residuals of zero point for cut aperture bias dim	123
B.12	Distribution in magnitude for cut aperture bias dim	124
B.13	Residuals of zero point for cut aperture bias bright	125
B.14	Distribution in magnitude for cut aperture bias bright	126
B.15	Residuals of zero point for cut variable star	127
B.16	Distribution in magnitude for cut variable star	128
B.17	Residuals of zero point for cut clipped in zp fit	129
B.18	Distribution in magnitude for cut clipped in zp fit	130
B.19	Residuals of zero point for all cuts combined	131

List of tables

3.1	Central coordinates of the CFHT Deep Survey fields. An estimated average value of Milky Way $E(B - V)$ is given using the Schlegel et al. (1998) maps, which will be discussed further in section § 6.3.4	38
3.2	Total integration time of the deep survey in different bands, <i>for each field</i> i.e. the total time allotted to the survey is 4 times what is shown.	38
4.1	Average and standard deviation of $\tan z \cos \eta$ and $\tan z \sin \eta$ across all fields. Note that within the same field the values are very similar from band to band.	56
5.1	Parameters relating fitted sky level and flux as a function of color for bright stars (Eq. 5.8).	75
5.2	Color terms and offsets between PSF and aperture natural magnitude systems in each band. α and ϵ are defined by Eq. 5.12 . The λ_0 parameter describes the corresponding additional effective filter of equation 5.14 such that $C(\lambda) = \lambda + \lambda_0$	77
5.3	Final calibration uncertainty of the SNLS survey, as obtained by the work of Betoule et al. (2013)	78
5.4	Summary table of statistical uncertainties due to zero point fitting. The mean, min, and max sub-columns correspond to the average, minimal, and maximal values of the quantity in question across all 36 CCDs.	79
5.5	Summary of systematic uncertainties due to PSF photometry. Note that if the effect is filter dependent, the table shows the maximum uncertainty.	80
6.1	83
6.2	Contributions of each survey to the Hubble Diagram after cuts, including average redshift and residual of each survey after a fit to a Λ CDM model (see section § 6.5.1).	84
6.3	Results of fit for flat Λ CDM model, for blinded data.	101
B.1	Description of aperture bias cuts. These are chosen by considering the patterns observed in figure B.2	112
B.2	Description of cuts on stars used during zero point fitting. We show the fraction of stars each cut eliminates as a percentage of the total sample. We also show the shift in zero point had it been computed excluding this cut. The referenced figures correspond to the distribution in magnitude of the cut stars, and their residues as a function of magnitude. The combination of all cuts can be seen in figure B.19 . An example of these cuts for a single zero point fit can be seen in figure B.1	113

Introduction

The advent of **General Relativity** (GR) in the early 20th century heralded the era of modern physical cosmology. One of its simplest solutions, the Friedmann equations, was the result of applying GR to the universe as a whole and were discovered in 1922 ([Friedmann 1922](#)). They described the underlying dynamic of cosmological evolution as being that of a metric expansion of space. The backwards extrapolation of this expansion indicated that the universe originated as an infinitely hot, dense soup of matter and radiation, and was thus eventually dubbed the **Big Bang** theory. The ensuing decades saw a slow but gradual confirmation of many of the most basic implications of this expanding universe.

In 1929, Edwin Hubble's observations confirmed that, in our cosmological neighborhood, an object's redshift was directly proportional to its distance from us ([Hubble 1929](#)). This was a direct test of the concept of metric expansion itself. In 1965, Penzias and Wilson discovered the faint traces of a much hotter, denser early universe in the form of isotropic microwave radiation ([Penzias & Wilson 1965](#)). This microwave radiation is often dubbed "fossil radiation" because it probed a much earlier stage of the universe's history than Hubble's discovery. The temperature of the discovered radiation seemed consistent with theoretical expectations. This same radiation was thought to have very small anisotropies (later found to be on the order of 10^{-5}) as a result of adiabatic fluctuations in the very early universe. These fluctuations seed the large scale structure growth in the later universe. In 1992, the first measurement of these anisotropies was carried out using the **Cosmic Background Explorer** (COBE) ([Smoot et al. 1992](#)). The results proved to be the definitive piece of evidence that gave the Big Bang theory a wide consensus. Today, this consensus is near universal.

At the same time, the COBE results also observationally confirmed some of the first challenges to the Big Bang model of cosmology. Combining the correlations in the observed fossil radiation with the expected history of expansion seemed to suggest superluminal communication in density anisotropies in the early universe. In addition, the COBE data indicated a spatially flat metric, and it was not clear why this had to be the case. In the late 1990s, a significant discovery was made when two independent teams of cosmologists working with supernovae ([Riess et al. \(1998\)](#) and [Perlmutter et al. \(1999\)](#)) found that the expansion of the universe was in fact accelerating, which lies in stark contradiction with the simplest scenario of a flat matter dominated universe.

Rather than completely overturn the Big Bang theory, these anomalies and others have instead served to enrich the theoretical landscape with which modern cosmology concerns itself. The Big Bang theory itself is better thought of as a *class* of models, rather than a single well defined theory. Each such model contains a number of assumptions regarding the structure of the universe and its energy content. Hence, anomalies in cosmology could be indicative of new physics in a whole host of areas, ranging from basic assumptions regarding homogeneity and isotropy, to General Relativity itself, to particle physics, and even to the fundamental question of interpreting infinities in quantum field theory. Indeed, none of these anomalies require us to

rule out the concept of metric expansion. Instead, they force us to rethink what mechanisms lie behind it.

Following in the success of the seminal supernova observations, the **Supernova Legacy Survey** (SNLS) was undertaken to provide the most competitive constraints to date regarding the accelerating expansion of the universe. The aim of this manuscript will be to give the reader a thorough overview of both the conceptual underpinnings of supernova cosmology in general and the technical details of the SNLS experiment in particular.

In chapter § 1, we aim to offer a review of the current theoretical status of cosmology. While there exists a “standard” model of cosmology, there is no wide consensus on its validity. In particular, a great diversity of views emerge when trying to explain the aforementioned anomalies. We explore a few of these views with respect to the acceleration anomaly.

In chapter § 2, we introduce **type Ia Supernovae** (SNIa), the supernovae that are studied by the SNLS (and all other supernova cosmology experiments). In particular, we motivate their use as probes of expansion, or so called “standard candles”. We also discuss their shortcomings as standard candles and how to get around them. In particular, it is in this chapter that we introduce the spectrophotometric model of SNIa known as **SALT2**, a crucial component of the so called “standardization” procedure. We also discuss issues that will be of particular concern for future, more precise generations of supernova surveys relating to open questions in the realm of SNIa standardization.

In chapter § 3, we present an overview of the SNLS experiment. This includes presenting the instruments used to collect the science images, the manner in which the data was collected, and a brief overview of the science analysis that follows in the remaining chapters.

In chapter § 4, we look at the process of transforming images of supernovae into a time series of fluxes, known as a **light curve**, corresponding to the observed brightness of the SNIa. This process is known as **photometry**. In chapter § 5, we explain the calibration process of the obtained fluxes. These two processes are intertwined, as high precision photometry requires a careful application of the calibration procedure that takes into account the peculiarities and characteristics of the photometry method employed.

Finally, in chapter § 6, we describe the use of all the aforementioned steps to produce cosmological constraints. We place special emphasis on the determination of the various uncertainties at play. We conclude with an overview of the results of the analysis in its current state of advancement.

Of note is that this will constitute the first cosmology analysis of the full SNLS supernova sample. The SNLS analysis has been progressively releasing cosmological analyses as its methods and data sample have evolved with time. The results of the first year data set can be seen in [Astier et al. \(2006\)](#). The three year data set results can be seen in [Guy et al. \(2010\)](#), [Sullivan et al. \(2011\)](#), and [Conley et al. \(2011\)](#). The total data set represents five years of data taking.

Following the release of the three year data set, a close collaboration developed between some members of the SNLS and some members of the supernova cosmology team of the **Sloan Digital Sky Survey** (SDSS). This collaboration was dubbed the **Joint Lightcurve Analysis** (JLA). A number of significant improvements to and validations of the analysis methods of supernova cosmology were attained as a result of this collaboration, which we will explore in the course of this manuscript. All these improvements were put into effect in the JLA cosmology paper [Betoule et al. \(2014\)](#), providing new and improved cosmological constraints compared to the previous analysis of the three year data set. This manuscript follows hot on the heels of this paper, and the final cosmology analysis closely mimics that of the JLA paper, the most notable difference with which is the inclusion of the final 5 year data set of SNLS. We refer to this ongoing analysis as SNLS5.

Chapter 1

Physical Cosmology and the Acceleration of Expansion

In this chapter we present a broad overview of the theoretical concepts crucial to our current understanding of cosmology. We begin by looking at the evolution of our concept of relativity, from Galilean to General Relativity. We then explore how General Relativity can give rise to a class of predictive models about our universe's history, and how these models tie into the cosmological parameters. Afterwards, we present the so called Λ CDM model, the simplest model that can explain our current observations, in particular the relatively recent observation that the expansion of the universe is accelerating. Finally, we briefly explore the many other models that have been put forth to explain this acceleration.

1.1 A Historical Overview of Relativity

1.1.1 Galilean Relativity

Which reference frames can be called inertial ? Answering this question has led to some of the most profound discoveries of physics, and fundamentally altered our very understanding of space and time. In this section, we take a historical approach to understanding why and how this question led to the formulation of **General Relativity** (GR). A principal motivating factor in defining such frames is understanding how the formulation of the laws of physics depends on the chosen reference frame. While such investigations have led to widely varying descriptions of space and time as the laws considered change, there is a single postulate that remains fundamentally the same in all theories of relativity :

Postulate 1 The postulate of relativity : *The laws of physics are invariant in all inertial reference frames.*

This postulate defines the very concept of inertial reference frames. To understand its implications, we begin with a simple thought experiment; one so fundamental most non physicists have already wondered about it. An observer is on a moving train. As the train begins to move, he has trouble telling if the train is moving forward or if the station is moving backwards. To answer this question, one must first consider what mechanical laws are being considered. To start, we begin by considering Newton's laws, famously formulated in [Newton \(1760\)](#). These are :

Newton's Law 1 *If no external forces are applied on a system, it remains at rest or continues moving at constant velocity.*

Newton's Law 2 *The mass times acceleration of a system equals the amount of external force exerted on it : $F = m \times a$*

Newton's Law 3 *For every force one system applies on another, the latter system exerts a force on the former equal in force but in the opposite direction.*

The galilean perspective on this issue is that both answers (either that the train is moving forwards or that the station is moving backwards) can be considered valid, so long as the relative motion between the two can be said to be rectilinear and uniform. The only thing that matters then, is that the proper transformations be applied when transferring coordinates from one reference frame to the other. We call the train station's reference frame S , and that of the train S' . If the train tracks are aligned with the x-axis, and the train is moving in the positive x direction with speed v , these transformation are :

$$\left. \begin{aligned} x' &= x - v \times t \\ y' &= y \\ z' &= z \end{aligned} \right\} \quad (1.1)$$

This can be justified by the fact that Newton's laws are invariant under this transformation. It is obvious that law 1 still holds, since equations 1.1 transform constant velocities into constant velocities. In addition, it is clear that the second derivative of x' is the same as that of x , provided v is constant in time. Hence, law 2 still holds. Finally, law 3 is left unaffected by these transformations. In other words, because only the second derivative in time of coordinates are thought to matter in the formulation of the laws of physics, adding a first order derivative (in time) to an inertial reference frame will lead to another inertial reference frame. This term will simply vanish after the second derivative is taken, and postulate 1 will hold for the laws of Newton. Our train passenger can now rest at ease in the knowledge that both of his answers are correct, and he can simply pick the frame which facilitates whatever particular physical problems he is trying to solve during his train ride.

1.1.2 Special Relativity

Suppose, however, that the particular problem he is trying to solve happens to involve an electrically charged ball. Maxwell's laws require that moving electrical charges create a magnetic field proportional to their speed. In other words, what happens when one introduces first order derivatives in the laws of physics ? Indeed, this is the case for Maxwell's laws.

This poses a conundrum to our train passenger. The galilean transformations described in equation 1.1 can reconcile the apparent motion of objects in reference frame S which are stationary in reference frame S' . It cannot, however, make magnetic forces appear out of thin air. It is clear then that the galilean transformations cannot satisfy the postulate of relativity if electromagnetic forces are involved.

To find a replacement for equation 1.1, we begin by reformulating the problem. First, we note that Maxwell's equations can be shown to lead to a wave equation :

$$\left. \begin{aligned} \left(\nabla^2 - \frac{1}{c^2} \frac{\partial^2}{\partial t^2} \right) \vec{E} &= 0 \\ \left(\nabla^2 - \frac{1}{c^2} \frac{\partial^2}{\partial t^2} \right) \vec{B} &= 0 \end{aligned} \right\} c = \frac{1}{\sqrt{\mu\epsilon}} \quad (1.2)$$

Where \vec{E} and \vec{B} are the electrical and magnetic fields, and μ and ϵ are the permeability and permittivity of vacuum. If the postulate of relativity is to hold, then the value of c must remain constant throughout any change of reference frame. Otherwise, that would require different values for the permeability and permittivity of vacuum, violating the postulate. This electromagnetic wave equation actually describes light waves, leading to a second postulate that we will use in formulating our next relativistic theory, **Special Relativity** (SR) :

Postulate 2 *The speed of light in a vacuum is the same for all observers.*

The idea, then, is to change the transformations of equation 1.1 into transformations that will satisfy postulate 2. The only way to accomplish this is to allow the transformations to affect the time coordinate as well. This leads to the Lorentz transformations :

$$\left. \begin{aligned} t' &= \gamma \left(t - \frac{vx}{c^2} \right) \\ x' &= \gamma (x - vt) \\ y' &= y \\ z' &= z \end{aligned} \right\} \gamma = \frac{1}{\sqrt{1 - \left(\frac{v}{c}\right)^2}} \quad (1.3)$$

While these transformations had been known prior to the advent of special relativity, the contribution of [Einstein \(1905\)](#) was to derive these entirely from postulates 1 and 2, and to understand that they represented fundamental properties of the geometry of space and time, and not the effects of motion on the size of rigid bodies (see the historical discussion in [Brown \(2003\)](#)). By allowing space and time to “mix” in these transformations, we have introduced the concept of spacetime. Before moving on to General Relativity, it is important to understand how norms are defined in spacetime. Given a 4-vector u with components u_μ its norm squared is defined as :

$$u^2 = -u_0^2 + u_1^2 + u_2^2 + u_3^2 \quad (1.4)$$

It is worth noting that such a definition ensures that norms are invariant under the Lorentz transformations of equation 1.3, and is therefore a fixed quantity regardless of the choice of reference frame. To simplify explanations regarding general relativity, we introduce here the concept of the metric tensor $g_{\mu\nu}$. The metric tensor is defined such that for any 4-vector u , its norm is :

$$u^2 = g_{\mu\nu} u^\mu u^\nu \quad (1.5)$$

It is clear therefore, that in the case of special relativity, the metric tensor is always the same. This special case of the metric tensor is usually written as $\eta_{\mu\nu}$:

$$\eta_{\mu\nu} = \begin{pmatrix} -1 & 0 & 0 & 0 \\ 0 & 1 & 0 & 0 \\ 0 & 0 & 1 & 0 \\ 0 & 0 & 0 & 1 \end{pmatrix} \quad (1.6)$$

1.1.3 General Relativity

At this point, our train passenger still has one final question. He has derived transformations that will allow him to transform coordinates from one reference frame to another. These transformations will not alter the laws of physics provided the 2 frames are moving apart from each other at a constant speed v . Going back to our initial question, however, how then do we define

inertial reference frames. These transformations allow us to say that if any given reference is an inertial one, then any other reference frame moving in a rectilinear and constant fashion relative to it is also an inertial reference frame. This defines a class of inertial reference frames *up to an acceleration*. How to tell then if our frame is an inertial one or an accelerating one?

Our observer might be tempted to draw upon his experiences aboard the train. When the train began to slowly edge forward, he could not tell if he was moving forward or if the train station was moving backward. On the other hand, when the train began to accelerate in order to reach its top speed, he felt pushed backwards against his seat, confirming that he was accelerating forward. We might then be tempted to use these virtual forces to define inertial reference frames : they are the class of frames that do not experience virtual forces. At this point, we are tempted to think that special relativity has completely solved the question of defining inertial reference frames.

However, much like Maxwell's laws challenge Galilean relativity, so too does the law of gravitation present a challenge to special relativity. Recall that in a given gravity field g , the force applied on a body is simply $m \times g$ where m is the mass of the body. Applying Newton's second law in this case becomes :

$$\begin{aligned} F &= m \times a \\ m \times g &= m \times a \\ g &= a \end{aligned} \tag{1.7}$$

Because the force of gravity is proportional to the mass of the gravitating system, Newton's second law implies that all gravitational forces are locally equivalent to an acceleration field. How then does one distinguish gravitating reference frames from accelerating ones ? The development of general relativity is rooted in the impossibility of this distinction. To understand this, we introduce our third and final postulate :

Postulate 3 *The equivalence principle* : *The inertial mass of a body (right hand mass term in equation 1.7) is equal to its gravitational mass (left hand mass term in equation 1.7).*

This postulate cements the indistinguishability of gravitating and accelerating reference frames. The solution of general relativity is to make the free falling frames the inertial frames. In this interpretation, the "force" of gravity as we experience it in everyday life is actually a virtual force, arising from our acceleration relative to local inertial frames. General relativity therefore sets out to write a set of equations relating the presence of energy to distortions in the spacetime metric. This derivation is constrained by the fact that these distortions must reproduce the observed effects of gravity. These are known as the **Einstein field equations** (EFE), and were first derived in [Einstein \(1915\)](#). They are :

$$R_{\mu\nu} - \frac{1}{2}Rg_{\mu\nu} = 8\pi T_{\mu\nu} \tag{1.8}$$

Where $T_{\mu\nu}$ is the stress-energy tensor, R is the Ricci scalar, and $R_{\mu\nu}$ is the Ricci tensor. In this world view, Newton's laws become replaced by the concept of geodesics which describe the path of inertial reference frames. The geodesic equations are also derived from the equivalence principle. We will not explore the differential geometry details of the EFE. Suffice it to say that our primary use for them as observational cosmologists lies in their ability to make predictions about the metric tensor $g_{\mu\nu}$. This tensor is the one most directly related to observables. In the next section, we will see how these equations give rise to the Hubble diagram. For now, we will

conclude by saying that it is a most profound testament to the power of physics that merely asking the question “who is in motion and who is not” leads to a theory capable of elucidating our cosmic origins.

1.2 Theoretical Basis of Modern Cosmology

1.2.1 The Friedmann Equations

The simplest solutions to the EFE are actually not for the case of a spherical mass, as is often the case in physics. Though it is a subjective assessment, the EFE are most easily applied to the universe as a whole. In this case, a number of different symmetries allow us to simplify the problem. Recall that the metric tensor is now a dynamical quantity. Rewriting equation 1.5 in differential form we find that the line element is given by :

$$ds^2 = g_{\mu\nu} dx^\mu dx^\nu \quad (1.9)$$

We begin by making a simplifying assumption :

Assumption 1 The Cosmological Principle : *The energy content of the universe is homogeneous and isotropic in space.*

Using this principle we can rewrite $T_{\mu\nu}$ as :

$$T_{\mu\nu} = \begin{pmatrix} \rho & 0 & 0 & 0 \\ 0 & p & 0 & 0 \\ 0 & 0 & p & 0 \\ 0 & 0 & 0 & p \end{pmatrix} \quad (1.10)$$

The homogeneity and isotropy required by the cosmological principle means that there exists a reference frame in which the off diagonal terms of $g_{\mu\nu}$ are 0, and in which $T_{11} = T_{22} = T_{33} = p$. We use this to rewrite equation 1.9 in less general form using spherical coordinates. Taking r , θ and ϕ to be comoving coordinates (i.e. observers at rest in (r, θ, ϕ) are in free fall), and defining the cosmic time t as the time measured by observers at rest in (r, θ, ϕ) we arrive at the **Friedmann-Lemaitre-Robertson-Walker** (FLRW) metric :

$$\begin{aligned} ds^2 &= -c^2 dt^2 + a^2(t) \left[\frac{dr^2}{1 - kr^2} + r^2 (d\theta^2 + \sin^2 \theta d\phi^2) \right] \\ &= -c^2 dt^2 + a^2(t) dl_{(3)}^2 \end{aligned} \quad (1.11)$$

Where k is the curvature of space. The dynamical quantity $a(t)$ is known as the scale factor. The simplifying symmetries constrain this to be the only dynamical quantity involved. The quantity multiplied by the scale factor is simply the line element for an infinitesimal displacement in 3D space, hence why we have rewritten it as $dl_{(3)}^2$. This is immediately apparent for the flat space case ($k = 0$) where one finds the usual formula for the line element in spherical coordinates. In other words, before we even apply the EFE, the underlying symmetries allow us to describe the universe using a single dynamical quantity, which can easily be understood as the evolution over time of the relative distance between objects. Because it is found to strictly increase over time, this evolution is referred to as **expansion**.

Assuming that the metric takes the FLRW form described in equation 1.11, and that the stress energy tensor takes the form described by equation 1.10, we can use the EFE to relate the scale factor to the energy content of the universe. These relations are known as the Friedmann equations, and were first described in [Friedmann \(1922\)](#) :

$$H^2 \equiv \left(\frac{\dot{a}}{a}\right)^2 = \frac{8\pi G}{3} \left(\rho - \frac{k}{a^2}\right) \quad (1.12a)$$

$$\frac{\ddot{a}}{a} = \frac{-4\pi G}{3}(\rho + 3p) \quad (1.12b)$$

H is defined as the Hubble parameter. Its value today, H_0 , is known as the **Hubble constant**. Assuming that the energy content of the universe is dominated by either matter or radiation, one can put general constraints on the values of ρ and p :

Assumption 2 *Energy density is positive.*

Assumption 3 *Pressure is positive.*

This would imply that the right hand term of equation 1.12b is negative, leading to a net deceleration in the universe's expansion. Here, we can already understand the implications of an observed acceleration. Namely that, in the context of the Friedmann equations, matter and radiation alone cannot explain the observations.

Before going further, it can be useful to rewrite equation 1.12a in a more wieldy form, better suited to compare it to various models of the universe. For a full description of the universe, we need to account for a multitude of possible contributions to its total energy density (traditionally thought to be matter and radiation). In what follows each such contribution is designated by the subscript i :

$$\begin{aligned} H^2(a) &= \frac{8\pi G}{3} \left(\sum_i \rho_i(a) - \frac{k}{a^2} \right) \\ &= \frac{8\pi G}{3} \rho_c(a) \left[\sum_i \Omega_i(a) + \Omega_k a^{-2} \right] \end{aligned} \quad (1.13)$$

Where $\Omega_i(a)$ is the density of fluid i relative to the critical density $\rho_c(a)$, and $\rho_c(a)$ is chosen such that the sum of all $\Omega(a)$, including $\Omega_k a^{-2}$, is equal to 1 (i.e. $\rho_c(a) = 3H(a)^2/8\pi G$). In this formalism, $\Omega_k a^{-2}$ is referred to as the curvature of the universe.

We can simplify the first Friedmann equation even further by treating the universe's energy content as an effective fluid and introducing the concept of an equation of state. This equation relates the energy density of a fluid to its pressure :

$$p = w \times \rho \quad (1.14)$$

Where w is the equation of state parameter. For matter, whose energy density is dominated by its mass energy, w is effectively 0. For radiation, whose energy density is dominated by its momentum, w is effectively 1/3. Semi-relativistic matter can take any value in between. Using local conservation of energy ($T_{;\beta}^{\alpha\beta} = 0$), the equation of state informs us about the rate of evolution of the energy density :

$$\Omega_i(a) \propto a^{-3(1+w_i)} \quad (1.15)$$

Finally, plugging this rate of evolution into equation 1.13 and comparing the left hand side with the present day rate of expansion H_0 , we obtain :

$$\frac{H^2}{H_0^2} = \sum_i \Omega_i a^{-3(1+w_i)} + \Omega_k a^{-2} \quad (1.16)$$

Note that here, the scale factor independent values of Ω represent their values today. Equation 1.16 is a particularly common form of the first Friedmann equation, since it contains many cosmological parameters of interest (the Hubble constant, the present day density of the various components that make up the universe, their equation of state, and curvature).

1.2.2 Cosmological Redshift

An important consequence of expansion is its impact on the frequency of light as it travels across a changing metric. This change in frequency is defined by the quantity z , known as the redshift, and defined such that :

$$1 + z = \frac{\nu_e}{\nu_o} \quad (1.17)$$

Where ν_e is the frequency at emission and ν_o the observed one.

Imagine a light wave emitted at time t_e , and observed at time t_o . For light, we have that d_s of the FLRW metric (equation 1.11) is 0. We also choose our coordinate system such that $r = 0$ for the observer, the light is emitted at $r = R$, and its path is radial (i.e. $d\theta = d\phi = 0$). Applying this to the FLRW metric (equation 1.11) we obtain :

$$\begin{aligned} 0 &= -c^2 dt^2 + a^2(t) \frac{dr^2}{1 - kr^2} \\ \frac{c^2 dt^2}{a^2(t)} &= \frac{dr^2}{1 - kr^2} \\ \frac{cdt}{a(t)} &= \frac{dr}{\sqrt{1 - kr^2}} \\ c \int_{t_e}^{t_o} \frac{dt}{a(t)} &= \int_R^0 \frac{dr}{\sqrt{1 - kr^2}} \end{aligned} \quad (1.18)$$

Applying the same reasoning one period later, we obtain :

$$c \int_{t_e+1/\nu_e}^{t_o+1/\nu_o} \frac{dt}{a(t)} = \int_R^0 \frac{dr}{\sqrt{1 - kr^2}} \quad (1.19)$$

Note that the right hand side of equations 1.18 and 1.19 are the same. We can thus set the left hand sides as equal :

$$\begin{aligned} c \int_{t_e}^{t_o} \frac{dt}{a(t)} &= \int_{t_e+1/\nu_e}^{t_o+1/\nu_o} \frac{dt}{a(t)} \\ \int_{t_e}^{t_o} \frac{dt}{a(t)} &= \int_{t_e}^{t_o} \frac{dt}{a(t)} - \int_{t_e}^{t_e+1/\nu_e} \frac{dt}{a(t)} + \int_{t_o}^{t_o+1/\nu_o} \frac{dt}{a(t)} \\ \int_{t_e}^{t_e+1/\nu_e} \frac{dt}{a(t)} &= \int_{t_o}^{t_o+1/\nu_o} \frac{dt}{a(t)} \end{aligned} \quad (1.20)$$

Assuming that the scale factor changes negligibly during a single period, we can consider $a(t)$ to be a constant in the integrals of equation 1.20 (a_o for the scale factor at observation time, and a_e for the scale factor at emission). Equation 1.20 becomes simply :

$$\begin{aligned} \frac{1}{a_e}(t_e + 1/\nu_e - t_e) &= \frac{1}{a_o}(t_o + 1/\nu_o - t_o) \\ \frac{1}{a_e\nu_e} &= \frac{1}{a_o\nu_o} \\ \frac{\nu_e}{\nu_o} &= \frac{a_o}{a_e} \\ 1 + z &= \frac{a_o}{a_e} \end{aligned} \tag{1.21}$$

Note that the resulting redshift depends only on the ratio of the scale factors at the time of emission and observation. In other words, it does not in any way depend on the rate of change of the scale factor at either time, nor does it depend on its intermediate history between emission and observation. Redshift is therefore a direct probe of the relative scale factor at the time of emission. Of course, this is only true provided the observed redshift is only the result of cosmological expansion in a homogeneous universe. In other words, it excludes possible contributions from the peculiar velocity of the object itself, and expanding potential wells due to the intervening structure between emission and observation.

1.2.3 The Hubble Diagram

Such an expansion would obviously have an impact on the distance of objects as a function of redshift. Keep in mind, however, that “distance” is not a well defined concept in general relativity and we must be more specific in order to be clear. Here, we will consider the concept of luminosity distance. Anyone who recalls the formula for the surface of a sphere will not be surprised to learn that luminosity distance is defined as :

$$F = \frac{L}{4\pi d_L^2} \tag{1.22}$$

Where L is the intrinsic luminosity of an object, F is the amount of light received by an observer, and d_L is the luminosity distance. Using the Friedmann equation 1.12, we can compute the luminosity distance’s dependence on the Hubble parameter, which changes form depending on the curvature of the universe :

$$d_L(z) = \begin{cases} \frac{(1+z)c}{H_0\sqrt{|\Omega_k|}} \sin \left[\sqrt{|\Omega_k|} \int_0^z \frac{dz'}{H(z')/H_0} \right] & \text{for } k = 1 \text{ i.e. } \Omega_k < 0 \\ \frac{(1+z)c}{H_0} \int_0^z \frac{dz'}{H(z')/H_0} & \text{for } k = 0 \text{ i.e. } \Omega_k = 0 \\ \frac{(1+z)c}{H_0\sqrt{|\Omega_k|}} \sinh \left[\sqrt{|\Omega_k|} \int_0^z \frac{dz'}{H(z')/H_0} \right] & \text{for } k = -1 \text{ i.e. } \Omega_k > 0 \end{cases} \tag{1.23}$$

Because the Hubble parameter and its evolution over time can itself be related to cosmological parameters using equation 1.13, we are now in a situation where we can constrain those parameters using an observable, namely the luminosity distance. In figure 1.1, we compare the evolution of the flux of an object over a redshift range, assuming a constant luminosity, for different cosmological models. This gives us an idea as to the measurement precisions required

in order to constrain different models. In real life, we cannot simply move an object of galactic brightness across cosmological scales. Instead, we must rely on objects whose intrinsic luminosity can be considered either constant from one object to the next or well determined for each observation. Such objects are called **standard candles**. In the next chapter, we will explore the properties of **type Ia supernovae**, and show that these can be used as standard candles.

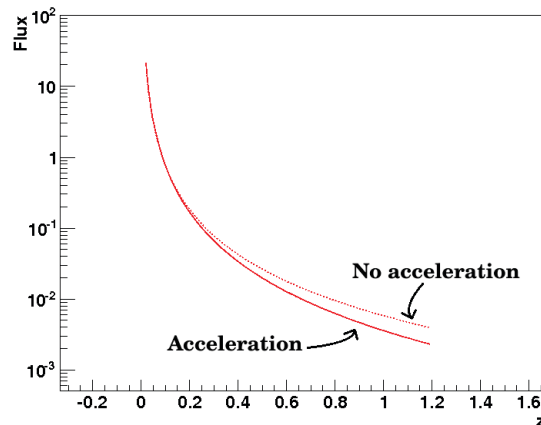


Figure 1.1: Here we plot the observed flux of an object as a function of the redshift at which its light was emitted, for different cosmology models. The dashed line corresponds to a flat matter dominated universe in which there is no acceleration. The solid line corresponds an accelerating expansion, similar to actual observations.

1.3 Constructing the Λ CDM Model

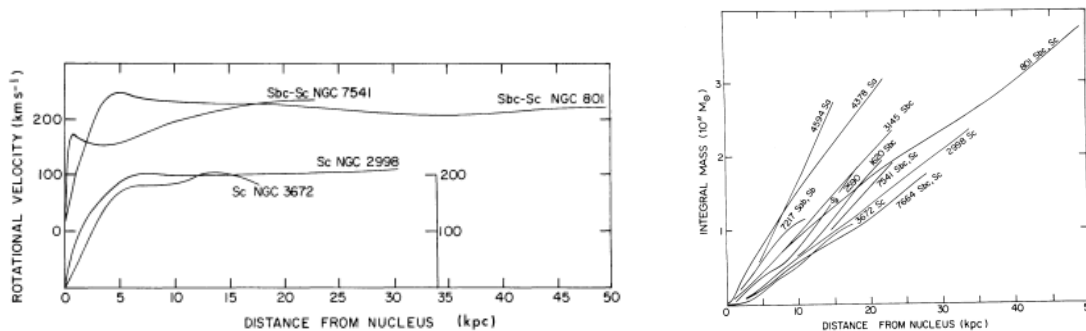
In this section we will explore the experimental and theoretical foundations of the so called Λ CDM model. This model, rather than being the result of a consensus, can be thought of more as a placeholder model. What is meant by this is not that it is the most physically motivated model. Rather, it is the simplest model that can be invoked to explain the observations, in other words, the one with the least degrees of freedom. As we will see in the next section, many different classes of models have been postulated to replace it. However, none so far have yielded detectable observational differences between the two.

1.3.1 On the Astrophysical Need for Dark Matter

We begin by looking at the early history of the CDM in Λ CDM, which stands for **Cold Dark Matter**. As the name implies, CDM is a form of matter that is both **dark**, in that it does not interact with electromagnetic radiation, and **cold**, in that the velocities of the particles that make it up are too small to significantly wipe out structure formation in the early universe. The most straightforward attempts at describing such matter using particle physics unsurprisingly belong to a class of models called **Weakly Interacting Massive Particles** (WIMPs), whereas CDM is made dark because its interaction cross sections are extremely small, and is made cold because it is massive (see section 4 of [Kamionkowski \(1998\)](#)).

Historically, the principal motivating factor for introducing it has been the presence of discrepancies between estimated galactic masses and their dynamical behavior. As recounted in [van den Bergh \(1999\)](#), various observations stretching back to Zwicky's cluster observations in

the early 1930's gave hints of this anomaly. An unmistakable and seminal signal was discovered by [Rubin et al. \(1978\)](#) using high precision spectroscopy. Specifically, maps of the baryonic density of galaxies seemed to imply that the density profile of galaxies peaks at the center, and yet the rotation curves of galaxies (average stellar velocity as a function of distance from galactic center) failed to follow suit, as seen in figure 1.2.



(a) Rotation curve of various galaxies as measured by [Rubin et al. \(1978\)](#). Note that the rotation curve remains flat well beyond the observed range of baryonic matter in all cases. (b) Integral mass as a function of distance from galactic nucleus, as deduced from the galactic rotation curves.

Figure 1.2: The density profile required to explain the observations implies the presence of significant amounts of missing mass.

Since then, the presence of dark matter has been used to explain other dynamical observations requiring the presence of mass exceeding that of the observed baryonic matter, such as the high velocity dispersions of galaxy clusters. As we will see later in this section, present day cosmological observations, and not just astrophysical ones as discussed above, require that the density of matter in the universe be different than its baryonic density, namely that roughly only 20% of matter be baryonic. CDM is also needed to explain the growth rate of structures, otherwise discrepancies arise when comparing its expected current state from CMB observations (see section § 1.3.3.1). This serves as a strong argument against theories that try to explain the anomalies by modifying the dynamical laws underlying the behavior of astrophysical scale systems, since CDM has been invoked to explain the data in a wide variety of contexts.

1.3.2 The First Acceleration Observations From SN

The seminal observations that first indicated an acceleration in the expansion rate of the universe were those of [Riess et al. \(1998\)](#) and [Perlmutter et al. \(1999\)](#). While the sample of nearby supernovae was nearly identical in both papers, these were two independent teams that had been working in parallel. This provided a certain degree of independent confirmation of the result, at least vis- \AA -vis analysis methods. To understand the significance of their observations, we rewrite the first Friedmann equation (as formulated in equation 1.16) for a universe containing only matter and radiation, what seemed like a reasonable assumption prior to these observations. This yields :

$$\frac{H}{H_0} = \Omega_m a^{-3} + \Omega_r a^{-4} + \Omega_k a^{-2} \quad (1.24)$$

The only free parameters involved are Ω_r (which in practice is so small it has no effect on the observations at hand), Ω_m , and Ω_k . The data was statistically incompatible with the prediction

of equation 1.24 for *any* given values of Ω_m and Ω_k . This meant that either a new component had to be added to the universe's energy content, or there was a significant error in the derivation of the Friedmann equations. Either way, this shakes the foundations of modern cosmology, and continues to be one of the most active areas of research in the field today.

Since the Hubble diagram produced was incompatible with any combination of Ω_m and Ω_k , a new parameter was added to fit the data. Indeed, many in the theoretical particle physics community wondered if the non-zero (indeed infinite) expectation value of the vacuum energy predicted by the **Standard Model** of particle physics had an effect on cosmology. This question, known as the **Cosmological Constant Problem**, has troubled physicists for decades and continues to do so. We do not have time to give a full treatment of such a vast problem. Instead, we redirect the reader to the extremely comprehensive reviews of [Weinberg \(1989\)](#) and [Martin \(2012\)](#). For now, suffice it to say that a non zero vacuum energy represents a constant energy density that does not change with the scale factor. In other words it would alter equation 1.24 to give :

$$\frac{H}{H_0} = \Omega_\Lambda + \Omega_m a^{-3} + \Omega_r a^{-4} + \Omega_k a^{-2} \quad (1.25)$$

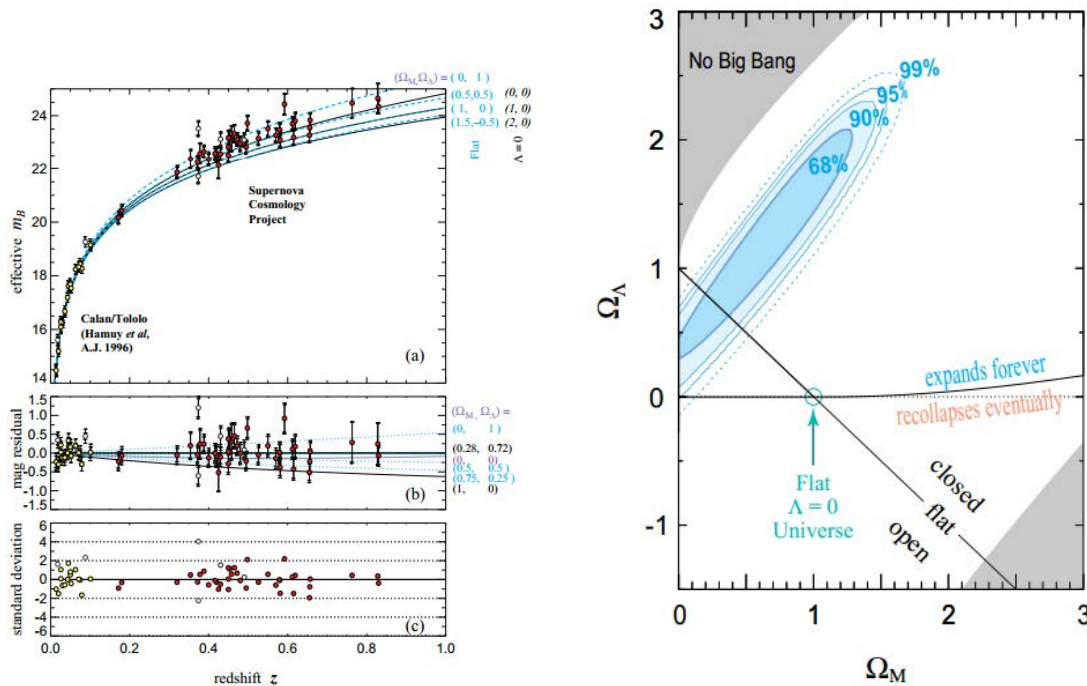
The results of fitting to this model using the [Perlmutter et al. \(1999\)](#) data are seen in figure 1.3. Of note is that the supernova data *alone* excludes any model where Ω_Λ is equal to 0, thus providing strong evidence for acceleration. Indeed, assuming flatness, the paper concludes that $P(\Omega_\Lambda > 0) = 0.9984$.

Note that while the choice of adding Ω_Λ was theoretically motivated, the data does not exclude other explanations. Indeed, one of the principal concerns of SNIa cosmology is that the observed results actually reflect cosmological evolution, and not evolution in observed SNIa luminosity, either due to their intrinsic luminosity decreasing with redshift or intergalactic dust dimming high redshift supernovae. However, it is important to keep in mind that the observations only deviated from a decelerating universe for low redshift supernovae, but that higher redshift supernovae again became compatible with a decelerating universe, as expected from a signal that is indeed due to late time cosmological acceleration. The late time deceleration cannot be incompatible with the presence of dust which can only dim supernovae, and would require a far fetched tuning of SNIa intrinsic luminosity evolution so as to first brighten then dim SNIa in just the right way as to reproduce Λ CDM. Therefore, the most likely explanation for the observations was that the universe does indeed undergo a late time phase of accelerated expansion.

Whatever the actual mechanism driving this acceleration, it is referred to as **Dark Energy**, where here the term ‘‘Dark’’ refers to our as of yet uncertainty regarding its nature. Indeed, the [Riess et al. \(1998\)](#) paper gives a constraint on the deceleration parameter, which is directly related to the equation of state parameter w simply by $q = (1 + 3w)/2$ for a flat universe. Depending on the analysis method used, the uncertainty on q delivered by [Riess et al. \(1998\)](#) is at best 0.3, which corresponds to an uncertainty on w of 0.2, leaving the door open for a wide host of models, certainly not limited to the $w = -1$ case of Ω_Λ . Likewise, the actual portion of the universe's energy budget that Ω_Λ represents is extremely uncertain, lying around 0.65 ± 0.2 .

1.3.3 Concordance With Other Probes

In the days since these initial observations, new probes have delivered their own constraints on overlapping cosmological parameters, providing significant constraints on the dark energy problem.



(a) Hubble diagram showing multiple model lines for comparison with the data. No model with $\Omega_\Lambda = 0$ can fit the available data. (b) Contour in Ω_m VS Ω_Λ space showing the impossibility of a purely matter dominated flat universe. Note that this impossibility remains true even if we relax the condition of flatness.

Figure 1.3: Cosmological results using the luminosity distance estimates of Perlmutter et al. (1999).

1.3.3.1 The Cosmic Microwave Background

The **Cosmic Microwave Background (CMB)** represents the light emitted at a redshift of about $z_{\text{decoupling}} = 1,091 = z^*$ when the universe became transparent to the photons it contained. Indeed, prior to this redshift, the universe was a photon-proton-electron plasma. When the photons decoupled from the protons and electrons, they began to travel freely, being significantly redshifted until their capture in our modern day microwave detectors. These observations are not particularly sensitive to the equation of state of dark energy given that large differences in the value of w have a similar impact on CMB observations than would small differences in the value of Ω_m . However, by constraining other cosmological parameters they limit the parameter space that supernova measurements must live in, thus lowering the uncertainty they deliver. In particular, the confidence contours of CMB observations in the Ω_m VS w plane are nearly orthogonal to those of SNIa observations.

We review some of the physical mechanisms that underlie CMB observations in order to understand its implications for cosmology. To start, the CMB itself represents the most perfect black body ever observed. The temperature maps of the CMB (see for example figure 1.4) are extremely uniform across the sky, and the variations observed therein are on the order of 10^{-5} in temperature. The main analysis for extracting information from the CMB lies in the angular dependence of the correlations of these variations.

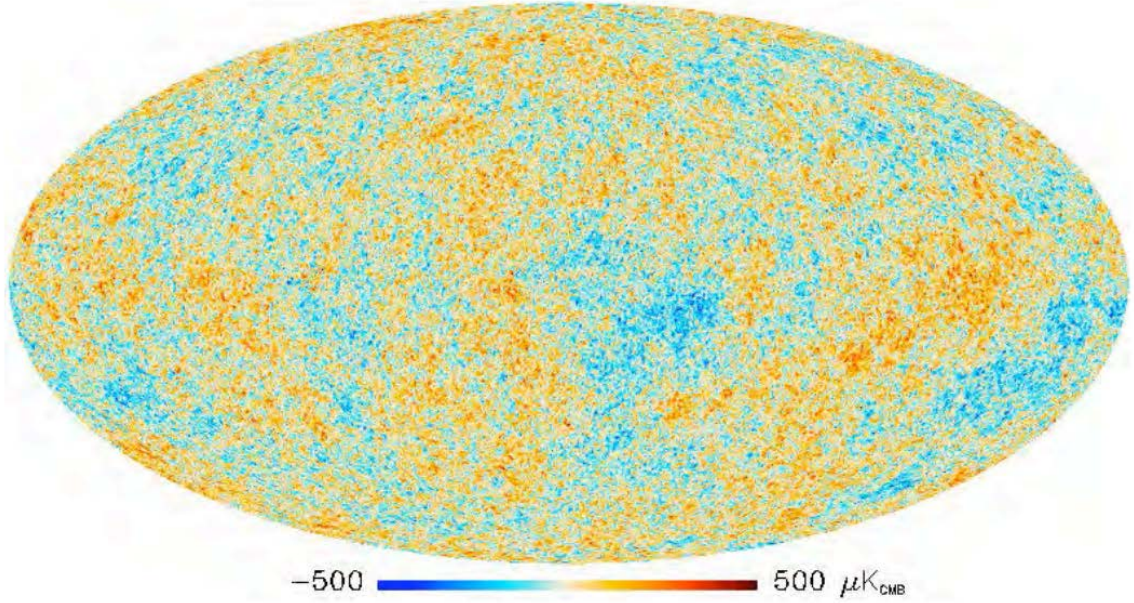


Figure 1.4: Map of CMB temperature anisotropies as seen by Planck. The central regions correspond to the galactic plane and are mostly excluded from cosmological analysis.

To understand these correlations, recall that they represent the final state of a plasma that has just decoupled. Before decoupling, the counteracting forces of gravity and pressure led to acoustic oscillations emanating from the initial energy density inhomogeneities. These oscillations all spread at the speed of sound in plasma until decoupling occurred. In other words, all inhomogeneities led to oscillations that traveled for the same distance. This implies the existence of some characteristic scale where inhomogeneities will strongly correlate. This is called the acoustic horizon and we denote it r_s . For a flat universe, r_s can be shown to depend on $H(z)$ such that :

$$r_s(z^*) = \int_{z^*}^{\infty} c_s(z) dz / H(z) \quad (1.26)$$

$$c_s(z) = \frac{c}{\sqrt{3(1 + (3\Omega_b/4\Omega_\gamma)/(1+z))}}$$

Where c_s is the speed of sound in the photon-baryon-electron plasma, Ω_b the density of baryons, and Ω_γ the density of photons. Note that Ω_Λ is completely negligible for this time period. Therefore, $r_s(z^*)$ does not depend on the properties of dark energy. However, most interestingly, the actual composition of matter comes into play here. This is the cosmological probe we previously mentioned that required Ω_b and Ω_m to differ.

Note, however, that what we observe is not $r_s(z^*)$, but rather an angle on the sky that corresponds to $r_s(z^*)$. We call this angle θ^* , and it is related to $r_s(z^*)$ by the angular diameter distance $d_A(z)$ of the redshift we are observing :

$$\theta^* = \frac{r_s(z^*)}{d_A(z^*)} \quad (1.27)$$

$d_A(z)$ simply represents the ratio of an object's size to its angle on the sky at a redshift of z . Therefore, the late time evolution of expansion will have a weak but noticeable geometrical effect on our observations of θ^* , allowing for measurements of the angular distance of the CMB, as done in [Komatsu et al. \(2011\)](#). One can think of the measurement of r_s as a point on the angular diameter distance Hubble diagram at a redshift of z^* that is degenerate with the other values upon which r_s depends.

We would like to note that there exist other harmonic peaks beyond the one discussed above, and that their relative amplitude and positions serve to further constrain cosmological parameters. In addition, we note that so far we have only discussed density correlations that manifest through temperature maps of the CMB. But one can also consider, as the Planck collaboration and others before it have, polarization maps of the CMB and the correlations contained therein. Indeed, the CMB is a rich treasure trove of cosmological information, and we could not hope here to thoroughly cover all the constraints it provides.

1.3.3.2 Baryon Acoustic Oscillations

Baryon Acoustic Oscillations (BAOs) refer to the large scale structure consequences of the acoustic oscillations previously discussed. Because the inhomogeneities seen in the CMB lead to the large scale structures we observe in the later stages of the universe's life, they too display a characteristic separation scale (which corresponds to the same comoving distance in fact) where the matter auto-correlation function will peak. This peak is considered to be robust to the non-linear growth of structure to the extent that the bias parameter b is well known (where b characterizes the bias of baryonic matter as a tracer of the total matter density).

Here we will present the measurements as being averaged over several redshift bins. Because these bins do not have a negligible redshift width, the distance measurement they represent is a combination of angular diameter distance and redshift separation. Note that the effective redshift of decoupling and the effective redshift at which oscillations stop are not exactly the same. We refer to the latter as z_{drag} , and it has been computed in [Eisenstein & Hu \(1998\)](#). The measured angular separation corresponding to the BAO bump is given by :

$$d_z = \frac{r_s(z_{drag})}{D_\nu(z)} \quad (1.28)$$

$$D_\nu(z) = \left((1+z)^2 d_A(z)^2 \frac{cz}{H(z)} \right)^{1/3}$$

Each redshift bin will constitute another point in the angular diameter distance Hubble diagram. For dark energy measurements, combined CMB and BAO studies are here to constrain the values of the various Ω more so than to constrain their nature (i.e. determine w). The latest CMB study ([Planck Collaboration et al. 2013a](#)) constrains Ω_Λ to be 0.693 ± 0.019 for a flat Λ CDM fit by combining its data with the BAO measurements described in [Anderson et al. \(2012\)](#).

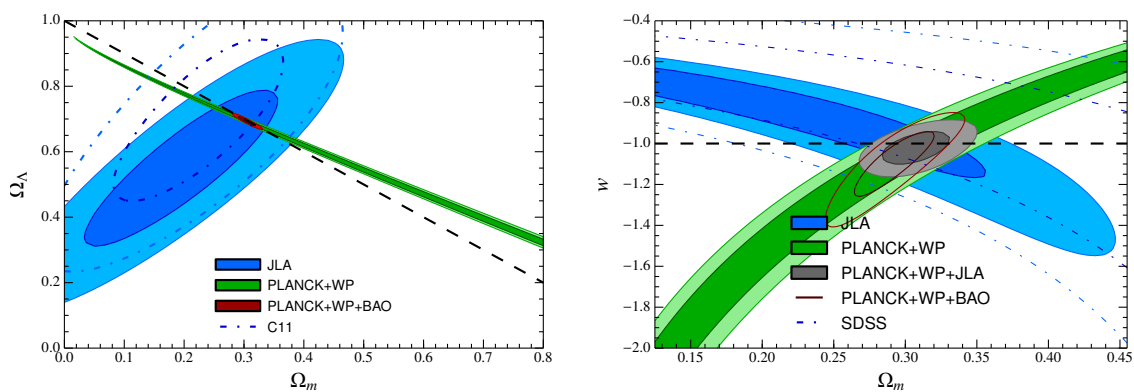
Note that we binned the measurements in redshift because this is how we will interpret the constraints they provide when combining them with the supernova data in section § 6.4.3. One can also separately measure the transverse angle and the longitudinal redshift separation that characterises the BAO peak. The ratio of the two is known as the **Alcock-Paczynski** probe, and can be used to constrain cosmological parameters other than the parameters of interest for dark energy measurements. Indeed, similarly to CMB measurement, the data of BAO surveys can be used to constrain other cosmological parameters. In particular, measurements of redshift

space distortions and of the complete power spectrum lead to constraints on the redshift of matter radiation equality, but can also constrain models of warm dark matter and neutrino masses.

1.3.3.3 Modern Supernovae Experiments

Combining these measurements with modern supernova experiments, the most significant of which will be described in detail throughout this thesis, leads to much more precise constraints on the nature of dark energy. In figure 1.5, we look at the constraints that these combined measurements bring about in the context of the JLA analysis. Note that the contours show that without supernova, our constraints on the nature of dark energy are greatly degraded.

The resulting uncertainty on w is now -1.027 ± 0.055 . The increasing precision with which a w of -1 is being measured helps transform the Λ CDM model from a mere fiducial model used to fit poorly constraining data into the current standard model of cosmology. This thesis will describe the work aimed at further improving this uncertainty, taking as a starting point the JLA analysis described in [Betoule et al. \(2014\)](#).



(a) Uncertainty contours in Ω_Λ VS Ω_m space compared with the previous supernova contour of [Conley et al. \(2011\)](#).

(b) Uncertainty contours in Ω_Λ VS w space.

Figure 1.5: Uncertainty contours of the JLA analysis. “Planck” represents CMB temperature data, “WP” represents CMB polarization data, and “BAO” represents BAO data. Note that in both parameter spaces, the 2 contours are nearly perpendicular and greatly compliment each other.

1.4 Theoretical Explanations of Observations

Recalling the definition of w given in equation 1.14, it is clear from equation 1.12b that w needs to be strictly less than $-1/3$ for there to be acceleration. From this perspective, it becomes somewhat generic of all models that acceleration becomes more significant over time. A fluid with $w < -1/3$ will decrease in density slower than regular matter or radiation (for which w is 0 and $1/3$ respectively), as described in equation 1.15. Hence, it will become dominant at later times.

Because the equation of state parameter distinguishes most clearly effective fluids which do and do not contribute to acceleration, it is frequently used as a benchmark test for the

effectiveness of a probe at measuring said acceleration. This, in turn, is why most models are categorized by their corresponding effective value of w .

1.4.1 Corrections to General Relativity

One class of explanations for the observed acceleration concerns itself with formulating alternatives to general relativity. The simplest and most famous such model was introduced by Einstein himself in [Einstein \(1917\)](#). This is the Λ CDM model that we have already introduced and it relies on the addition of a single scalar term to the EFE. These become :

$$R_{\mu\nu} - \frac{1}{2}Rg_{\mu\nu} + \Lambda g_{\mu\nu} = 8\pi T_{\mu\nu} \quad (1.29)$$

Einstein's initial motivations for such a correction was to achieve a static universe. However, this correction can also lead to acceleration, changing equation [1.12b](#) such that it becomes :

$$\frac{\ddot{a}}{a} = \frac{-4\pi G}{3}(\rho + 3p) + \frac{\Lambda c^2}{3} \quad (1.30)$$

Note that Λ does not depend on time. In other words, the Λ model corresponds to an effective fluid with $w = -1$. Incidentally, if this Λ were placed on the other side of the EFE, it would represent the vacuum energy discussed previously. For the correct value of Λ , this can lead to the observed acceleration. One could argue that this constitutes a well motivated correction to the EFE, if somewhat arbitrary in its value, because it satisfies local energy momentum conservation. In other words it satisfies :

$$\Lambda g^{\mu\nu}_{;\nu} = 0 \quad (1.31)$$

This model is attractive because it relies on the addition of only a single degree of freedom to explain the observations. What is unappealing, however, is the arbitrariness of the value of Λ , and in particular the complete lack of any physical mechanism capable of explaining the order of magnitude of Λ , let alone its value. There are other models of modified gravity, and rather than list them all we will instead discuss the primary challenge that faces them.

The theory of general relativity is well tested on a number of scales (a review of these can be found in [Will \(2006\)](#)). If we are to explain the accelerated expansion of the universe by modifying our theory of gravity, then we must modify it such that the Friedmann equations gain an acceleration term while all other tests of gravity remain consistent. The Λ correction accomplishes this because it essentially maintains the same theory except for adding a uniform scalar field in the theory. Hence, while its impact on the global metric is significant, it has little impact on local tests of gravity because it doesn't introduce a gradient to the energy density field. Other theories run into tuning problems precisely because they cannot naturally mimic this behavior. Chameleon theories ([Khoury 2013](#)) get around this problem by adding a field that becomes extremely massive (i.e. an extremely short scale force) when surrounded by matter. Hence, its local impact on gravity is negligible in all the contexts in which general relativity has been tested.

1.4.2 The Impact of Inhomogeneities

As we have seen, an important yet powerful assumption used in the derivation of the Friedmann equations is the cosmological principle. High redshift galaxy surveys indicate that while the universe seems isotropic, it is only homogeneous above certain scales. While it was always

obvious that homogeneity did not hold below certain scales, the traditional approach has been to simply conclude that while the Friedmann equations will therefore not accurately describe the “local” scale factor, it would describe the “average” scale factor so long as we only considered it to be accurate above the inhomogeneous scales. In other words, they describe the expansion of the “average” scale factor. Mathematically speaking, this is not the rigorous way to get around this problem.

Ideally, what one would do instead is to calculate the average of the expansion of the scale factor (as opposed to the expansion of the average scale factor). Some theorists have proposed methods of doing this in ways that would add an acceleration term to the Friedmann equations (Roukema et al. 2013). Because this model builds on the effect of inhomogeneities, it could explain why acceleration is a late time effect. Earlier in the universe’s history, structure formation was in its infancy and could not provide the necessary level of inhomogeneity. As the universe grows, structure formation kicks in, and so too does this effect become more significant. The biggest challenge for these models is providing a definite analytical solution to applying GR in an inhomogeneous universe. As it stands, however, such solutions are still lacking.

Another effect of these inhomogeneities is the loss of energy as light enters large potential wells, only to exit them after they have significantly expanded. Taking this into account, our interpretation of the observations must include what happens to the photons along the line of sight. This is known as the **Integrated Sachs Wolfe** effect (ISW) (the non-integrated Sachs Wolfe effect (Sachs & Wolfe 1967) concerns the gravitational redshifting of CMB photons). This effect alone cannot explain the anomalous observations assuming only a matter dominated universe. It is, however, important to keep in mind when comparing different probes. This is because the ISW affects supernovae measurements and other probes differently. Hence, it may one day reduce tensions between different probes measuring the acceleration as these become more and more precise. This is of particular importance in a Λ CDM universe where the ISW is made more significant by the late time acceleration.

1.4.3 Quintessence Models

In general, one can consider the impact on expansion of the addition of any fundamental field, in particular easy to use scalar fields, to the Lagrangian of particle physics. The only condition this field would have to satisfy for this field to be a candidate for dark energy is $w < -1/3$. Of course, this implies that we are completely ignoring the quantum contribution of this scalar field (and any other scalar field for that matter, such as the known Higgs field) to the vacuum energy problem, and are instead only considering its properties as a classical field. Here we follow the presentation of these models given in Yoo & Watanabe (2012). In quintessence models the potential field $V(\phi)$ is such that w is given by :

$$\begin{aligned}
 w_\phi &= \frac{p}{\rho} && \text{(by definition)} \\
 &= \frac{\frac{1}{2}\dot{\phi}^2 - V(\phi) - \frac{1}{6a^2}(\nabla\phi)^2}{\frac{1}{2}\dot{\phi}^2 + V(\phi) + \frac{1}{2a^2}(\nabla\phi)^2} && (p \text{ and } \rho \text{ for quintessence fields)} \\
 &= \frac{\frac{1}{2}\dot{\phi}^2 - V(\phi)}{\frac{1}{2}\dot{\phi}^2 + V(\phi)} && \text{(use spatial homogeneity to get rid of } \nabla\phi \text{ terms)} \quad (1.32) \\
 \phi \rightarrow 0 \\
 \approx & \quad -1 && \text{(for a slow rolling field)}
 \end{aligned}$$

The $\nabla\phi$ terms disappear by invoking spatial homogeneity. Hence, many models with a $V(\phi)$ that yields a $w_\phi < -1/3$ have been considered simply by constructing the proper $V(\phi)$, and

it is not hard nor particularly unnatural to construct models where $w \approx -1$ today, simply by having a slow rolling field where $\dot{\phi}$ is small and therefore $w_\phi \approx -1$. The difficulty lies in making such models distinguishable from the standard case of a $w = -1$ that is static in time. Indeed, equation 1.32 can vary with time, but our current probes are not sensitive to such changes. To get an idea of a probe's sensitivity to changes in the value of w , we can define w_a such that :

$$w(a) = w_0 + (1 - a)w_a \quad (1.33)$$

Such a parametrization is not physically motivated. Rather it exists merely to test a probe's sensitivity to the time dependence of w . In figure 1.6, we see the contour plots provided the JLA analysis in the w VS w_a parameter space. We find that w_a is barely even constrained (the uncertainty on w_a is of 0.552). If the Λ CDM model continues to be consistent with the data as the uncertainty on w continues to decrease, then the only way for future generations of experiments to either discard or further validate the model will be by increasing the sensitivity to the time dependence of w . For supernovae, this requires going to much higher redshifts. At such redshifts, the SNIa is redshifted such that the bulk of its light is in the infrared range, which is almost completely blocked out by the atmosphere. Such observations therefore require space based missions.

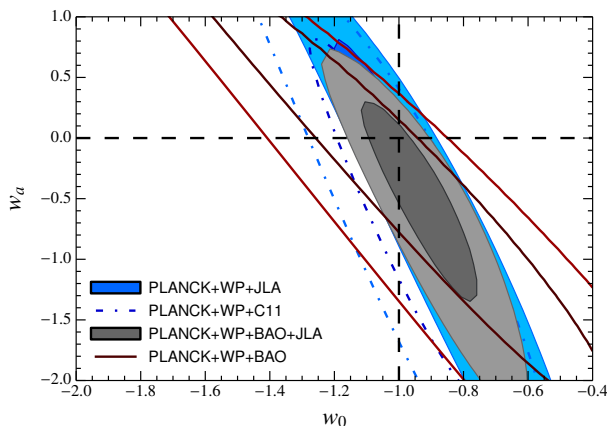


Figure 1.6: Uncertainty contours in the w VS w_a plane provided by the JLA analysis. w_a is almost completely unconstrained.

Chapter 2

Supernovae as Standard Candles

In this chapter we seek to motivate and describe the use of a certain type of supernova as standard candles. We begin by describing the empirical properties of these objects before moving on to the physical mechanisms that power them. Since the latter are still uncertain, it is better to define these objects empirically. We then move on to the necessary step of creating a spectrophotometric template model that captures their variability. Finally, we consider some open questions that remain vis-a-vis that variability.

2.1 Empirical Properties of SNIa

Supernova Cosmology relies heavily on empirical relations obtained through observations of a certain type of supernova : **type Ia supernovae** (SNIa). For this reason, we define SNIa not by the physical mechanism behind them, but by their observational properties. Indeed, given that the actual mechanism is still an open question, there is no other way to define them. In this section, we will explore these properties and motivate the use of SNIa as standard candles.

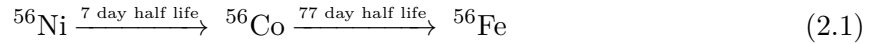
2.1.1 Spectroscopic Properties

In figure 2.1a, we see the spectrum of a typical SNIa at its maximum brightness. Because even within SNIa there exists some diversity, the definition of an SNIa does not have stringent boundaries. Instead, we assess the validity of a Ia typing by the degree of proximity between the spectrum of the observed transient object and another object, considered to be a typical SNIa. The latter are deemed typical because the features of their spectra lie near the center of the observed variability. Commonly used “typical” SNIa are SN1981B (Branch et al. 1983), SN1989B (Barbon et al. 1990), SN1992A (Kirshner et al. 1993), and SN1994D (Patat et al. 1996). Note that given the evolution of the spectra over the supernova’s lifetime, those features are easiest to identify around maximum light. Besides, for high redshift supernovae, the S/N ratio is only within acceptable bounds over a short period around maximum light. For this reason, for distant supernovae, the reliability of the classification depends strongly on the proximity to the maximum date at which the spectrum was observed.

SNIa spectra display a P-Cygni profile¹ due to the holotropic expansion of the ejecta at velocities typically on the order of $0.03c$ at the time of maximum luminosity, but sometimes even reaching up to $0.1c$ for certain extreme cases. Note that these high velocities (and the high

¹P-Cygni profiles correspond to the presence of both significant blue-shifted absorption and nearly rest frame emission features for a given spectral line.

optical spectrum, with a number of spectral features due to the chemical composition of the ejecta. The decay ^{56}Ni chain is :



2.1.2 Photometric Properties

SNIa are extremely bright events, around 4×10^9 solar luminosities in the blue band³, often making them as bright, or even brighter, than their host galaxies. This allows them to be observed up to very high redshifts.

In figure 2.2, we see a typical SNIa lightcurve in different bands. Notice that the maximum observed flux is not attained at the beginning of the explosion. At the start of the explosion, the matter density is still high and captures most of the emitted light. The explosion itself is roughly similar to the ballistic expansion of a sphere. Hence, the observed luminosity will ramp up progressively during this time due to a decrease in density (and therefore in opacity as well). This difference between the start of the explosion and the time of maximum luminosity is about 19 days in the rest frame of the supernova, and is called the **rise time**. It is the decay chain of the ^{56}Ni that drives the ensuing lightcurve. The supernova will then proceed to dim for a duration set by the half lives seen in 2.1. Note that in the red and infrared range, a second smaller peak occurs around 20 days after blue band maximum. This is due to a $\text{FeIII} \rightarrow \text{FeII}$ recombination that occurs when the supernova cools, increasing transparency in the red (Kasen 2006).

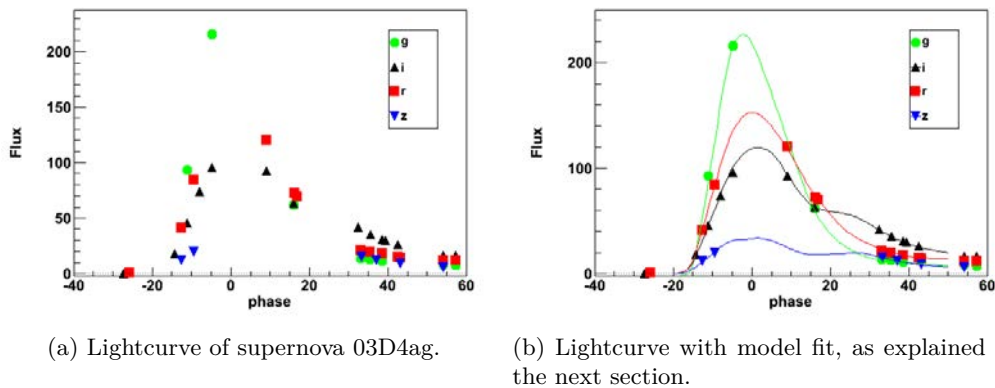
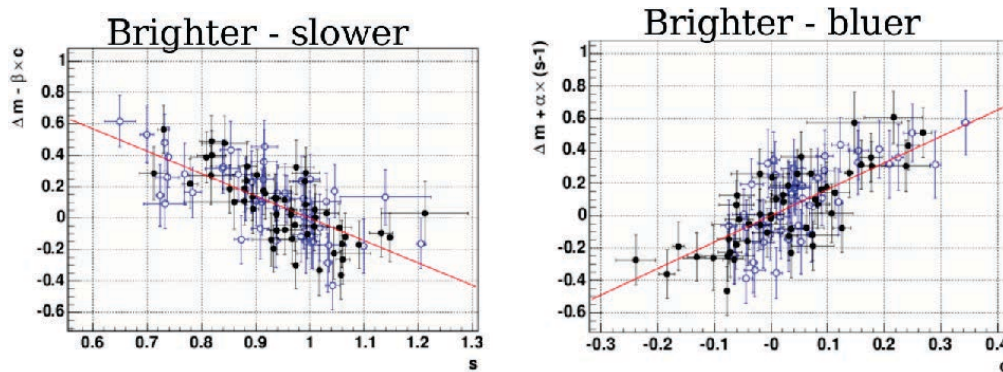


Figure 2.2: Typical supernova lightcurve, before and after model fitting, of supernova 03D4ag from the SNLS5 analysis. Note the second smaller peak in the redder i and z bands.

The quintessential photometric requirement for standard candles is the repeatability of their luminosity. In this respect, SNIa are not perfect standard candles. However, it has been noticed that the variability in their intrinsic luminosity is correlated with the variability of their lightcurves. 2 degrees of freedom clearly stand out in this variability as being strongly correlated with luminosity. These are known as **stretch**, named as such because it corresponds to certain SNIa having their lightcurves stretched in time, and **color**, named as such because it corresponds to chromatic differences between SNIa. The correlation of these parameters with luminosity is seen in figure 2.3. In section § 2.3, we take a closer look at the definition of these parameters and their use in determining the luminosity distance to the observed SNIa. Because

³The blue band, or *B* band for short, is centered on 4450\AA and has a bandwidth of 940\AA .

these corrections are needed for proper cosmological analysis, SNIa are known as **standardizable candles**. Note, however, that despite these corrections, there remains 15% of variability in the intrinsic luminosity of SNIa. In section § 6.2.3, we consider the impact of this dispersion on our ability to properly extract cosmological parameters from supernova data.



(a) The brighter/slower correlation. The x-axis is the stretch of the SNIa. The y-axis is its residue to the Hubble diagram after being corrected for the brighter/bluer correlation. (b) The brighter/bluer correlation. The x-axis is the color of the SNIa. The y-axis is its residue to the Hubble diagram after being corrected for the brighter/slower correlation.

Figure 2.3: The 2 most visible correlations between SNIa brightness and lightcurve properties.

2.1.3 Peculiar SNIa

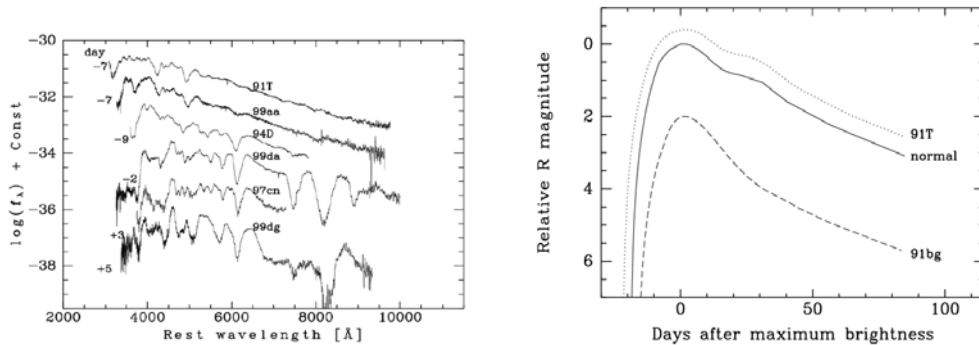
In roughly 30% of cases, SNIa are identified as **peculiar type Ia supernovae**. These are supernovae whose spectra display the features characteristic of an SNIa, but are either sub or super luminous relative to the bulk of the distribution, even after we take into account their stretch and color. This obviously presents a problem as they can bias our Hubble diagram were they to be included in our cosmology analysis. Fortunately, they are marked by the presence of other spectral features, as seen in figure 2.4a. Much like “normal” SNIa, the different sub-classes of peculiar SNIa are defined by their resemblance to an archetype.

2.1.3.1 Super-Luminous 1991T-like

The most prominent class of super-luminous SNIa are the so called **1991T-like**. The Ca II and Si II lines discussed above are markedly weak for these supernovae, in particular prior to the maximum, as shown in Li et al. (2001a), Filippenko et al. (1992b), and Mazzali et al. (1995). While these peculiarities are not present in all super-luminous SNIa, superluminous SNIa do generally have shallower lines for intermediate weight elements prior to maximum light. While these lines become deeper when the supernova starts to dim, some differences persist.

2.1.3.2 Sub-Luminous 1991bg-like

One class of sub-luminous SNIa closely resemble the archetypal 1991bg, described in Filippenko et al. (1992a) and Mazzali et al. (1997), and are therefore called **1991bg-like**. As measured by Filippenko (1997), in the blue band, they are dimmer by a factor of 10 relative to normal SNIa. A fast decline in luminosity after maximum light is characteristic of their lightcurves. Spectroscopically, they can be identified by their Ti II absorption lines (Li et al.



(a) Spectra of various peculiar SNIa compared to the spectra of 1994D, a normal SNIa. Notice that the superluminous objects tend to have erased features, while the subluminous ones tend to have more pronounced features (taken from [Li et al. \(2001b\)](#)).

(b) Light curves of peculiar SNIa relative to a normal SNIa. The rise time is greater for superluminous SNIa, and smaller for subluminous ones. Note also that subluminous SNIa do not display a local second maxima 20 days after maximum brightness.

Figure 2.4: Spectra and light-curves of peculiar SNIa relative to normal SNIa. The differences between the two are less obvious than between Ia and non-Ia supernovae, but are still significant enough to be distinguished after careful consideration of all the information at hand.

[2001a](#)). One is at 4200\AA , and the other is at 5900\AA . This latter line increases the depth of the aforementioned Si II line at 6100\AA .

2.1.3.3 Sub-Luminous 2002cx-like

The final class of peculiar SNIa we consider displays some odd spectral properties. Despite being roughly 6 times dimmer than normal SNIa, they actually have less pronounced spectral features and display highly continuous spectra in the red characteristic of super-luminous SNIa as seen in figure 2.4a. The archetypal object of this class is 2002cx, described in [Li et al. \(2003\)](#) and [Jha et al. \(2006\)](#), and they are therefore referred to as **2002cx-like**. Their spectra is, however, identifiable due to slow ejecta velocities. Indeed, the velocities indicated by the spectral broadening of features for 2002cx-like supernovae are on the order of $5,000\text{km/s}$, well short of the typical $10,000\text{km/s}$ of normal SNIa. In addition, their lightcurves present shorter rise times of about 4 days, and do not display a second peak in the red. These supernovae have been identified by the works of [Phillips et al. \(2007\)](#) and [Foley et al. \(2009\)](#).

2.2 Proposed Physical Mechanisms

Given the specifics of observational properties of SNIa, we can infer quite a few things about the physical mechanism behind them. The most important question is determining what type of stellar object, and under what conditions, exploded into the observed supernova. This object is called the **progenitor**. While the progenitor star itself is not hotly debated, what is still unknown is the configuration in which it finds itself prior to the explosion, and the mechanism by which it explodes. The 2 most popular models both assume a binary system, but it is a matter of some debate whether the binary system in question consists of a single white dwarf and a larger, less compact star from which it accretes mass, or of two white dwarfs that collide due to orbital decay caused by gravitational radiation.

2.2.1 The Single Degenerate Model

The model with a single white dwarf is known as the **single degenerate model** because it only contains a single mass of degenerate matter, namely the C-O white dwarf itself. For a long time, the consensus view (Livio 2000) was that the progenitor is an accreting carbon-oxygen (C-O) white dwarf, and that its explosion is triggered when its mass approaches the so called **Chandrasekhar mass** which is $M_C = 1.38M_\odot$ (Chandrasekhar 1931). It has been known for quite some time that Fermi degeneracy pressure would no longer sustain a mass of non-rotating degenerate matter past a certain mass. As the Chandrasekhar mass is approached, the temperature of the star diverges. The explosion would occur when at any point in the star the temperature reaches the C-O fusion threshold. This then leads to a runaway fusion reaction that could convert the bulk of the C-O star into intermediate and heavy mass elements in just a few seconds (Hoyle & Fowler 1960). This scenario is favored for a number of reasons, described in Astier (2012) as :

- The fusion products of C and O produce the Si, S, and Ca present in SNIa spectra.
- The final product of a C and O fusion chain would be ^{56}Ni . On the one hand, the half lives of its decay chain correspond to the timescales of SNIa lightcurves. On the other, the sharp emission lines observed in late time spectra (when Doppler broadening of features is not as significant) is also consistent with the decay chain of ^{56}Ni .
- Because the explosion would always occur at the same mass, such a model provides a simple explanation for the repeatability in the luminosity of these events.
- Few other stellar objects, apart from C-O white dwarfs, lack the H and He in their initial state.
- SNIa are the only type of supernova observed in old stellar environments. Hence, their progenitor is thought to be at the end of a stellar evolutionary path. This is the case for white dwarfs, the end fate of most stars of less than $8M_\odot$.

Despite these advantages vis-a-vis SNIa properties, the single degenerate model runs into problems vis-a-vis its companion star. This companion star is required to be a star whose surface gravity is small enough that the C-O white dwarf can easily rob it of its outer layers. This points to either red giants or late-type main sequence stars, both very bright stars, made even brighter if they are accreting material. It is thought, then, that older images of galaxies prior to an SNIa would reveal the bright companion star. All such searches have so far proved fruitless (see for example Maoz & Mannucci (2008), Li et al. (2011) and Schaefer & Pagnotta (2012)).

2.2.2 The Double Degenerate Model

To account for this shortcoming, the double degenerate model was proposed. In this model, the binary system consists of two C-O white dwarfs in close orbit, as described in Iben & Tutukov (1984). Given the compactness of such objects, general relativistic corrections to their orbit are

non negligible, in particular due to gravitational radiation. The emitted gravity waves eventually collapse the system, and the two white dwarfs collide. The existence of such binary systems is not a far fetched scenario, and indeed their number has been measured to be high enough to explain the observed number of SNIa, as shown in [Webbink \(1984\)](#). More generally, one may use the rate of SNIa and its evolution in redshift to distinguish between the two models, as this evolution can serve as a proxy for the age of the progenitor.

It remains an open question if such scenarios can explain the reproducibility of intrinsic SNIa luminosity. What it can explain, however, are the superluminous events that seem to require masses beyond the Chandrasekhar mass ([Howell et al. 2006](#)).

2.3 SNIa Modeling

In this section we describe the standardization procedure used to compute an effective brightness of SNIa with reduced variability. For reasons we shall explain in this section, doing this requires a complete spectrophotometric model to fit to the observations. None of the SNIa scenarios described in the previous section are reliable enough to provide such a model, in particular because the simulations required to go from explosion scenario to spectrophotometric model are extremely complex and depend on a whole host of unconstrained parameters. For this reason, the model is built empirically based on existing data of SNIa and the variability contained therein. The procedure we follow was first described in [Guy et al. \(2007\)](#), and is called **SALT2**⁴.

2.3.1 Standardizing the Distance Modulus

As we have seen, SNIa are better described as standardizable candles, rather than mere standard candles. This is due to the fact that we can observe a wide range of SNIa magnitudes at same redshift (roughly 30% RMS in magnitude). Fortunately, about half of this variability is correlated to measurable features of the SNIa lightcurve. As we have seen in [figure 2.3](#), 2 parameters clearly stand out as being correlated to brightness, namely stretch and color. By accounting for these observed correlations we correct the blue band magnitudes of our SN sample and obtain a new quantity called the distance modulus :

$$\mu = m_B - M_B + \alpha \times x_1 - \beta \times c \quad (2.2)$$

Where x_1 is the stretch parameter, c stands for color, m_B is a logged value of the integrated flux of the supernova, and M_B is the absolute magnitude of SNIa. As we shall see in [section 6.4.4](#), α and β are fit simultaneously with the cosmology.

2.3.2 On the Need for K-Corrections

Keep in mind that the photometric measurements of supernovae are done using filters that cover a set wavelength range. As we will see in more detail in [section § 5.2](#), each filter contributes to the instrument’s transmission $T(\lambda)$ ⁵. Typical shapes for the transmission functions of the MegaCam⁶ filters can be seen in [figure 2.5](#). Recall that the amount of light emitted by an

⁴**SALT** stands for “Spectral Adaptive Lightcurve Template” and was first described in [Guy et al. \(2005\)](#). SALT2 represents an incremental improvement on SALT.

⁵The transmission function is bounded between 0 and 1, and describes the fraction of light that arrives at the CCD as a function of wavelength. This function depends on both the filter used and the atmospheric transmission.

⁶MegaCam is the camera used by the SNLS experiment.

object cannot be quantified by a single number. Astronomical observations correspond instead to various amounts of light emitted throughout a spectrum of wavelengths. We call this an objects' **Spectral Energy Density** (SED). We refer to it hereforth as $\phi(\lambda)$. The measured flux therefore corresponds to :

$$F_{observed} = \int \phi(\lambda)T(\lambda)\lambda d\lambda \quad (2.3)$$

Because observing conditions can vary significantly from one image to the next, this quantity is a completely uncalibrated one. We calibrate this quantity by comparing it in the same observing conditions to that of an object with a known SED, known as a standard star. The calibrated flux is therefore the ratio of an object's flux to that of the standard star in the same observing conditions :

$$F_{calibrated} = \frac{\int \phi(\lambda)T(\lambda)\lambda d\lambda}{\int \phi_S(\lambda)T(\lambda)\lambda d\lambda} \quad (2.4)$$

In practice, we use a logged value of this quantity called a magnitude. Note that lower magnitudes indicate brighter stars, and vice versa :

$$m = -2.5 \log_{10} \left(\frac{\int \phi(\lambda)T(\lambda)\lambda d\lambda}{\int \phi_S(\lambda)T(\lambda)\lambda d\lambda} \right) \quad (2.5)$$

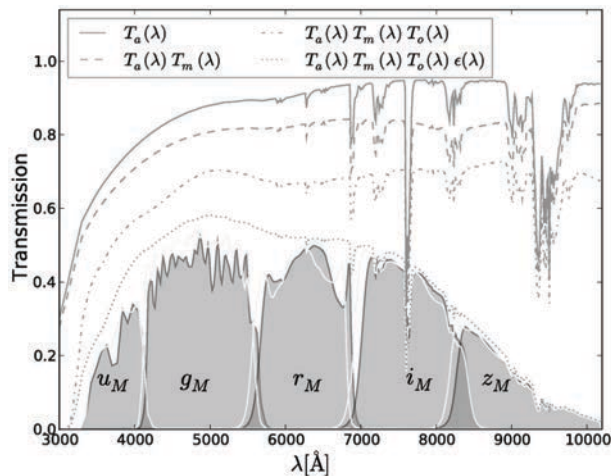


Figure 2.5: Total transmission functions for the 5 filters that describe the SNLS data. T_a is the atmospheric transmission function, T_m is the instrument transmission function, T_o is the filter transmission function, and ϵ is the quantum efficiency of the CCD. The total transmission function is the product of all of these.

Because the observed SNIa are redshifted, we cannot define its blue band magnitude to simply be one of the observed broad-band magnitudes, let alone do the same for stretch and color. In other words, the quantity defined in equation 2.5 corresponds to a different intrinsic wavelength range depending on the object's redshift. This is why the observed lightcurves are fit to a redshifted model whose free parameters will correspond to the parameters required to compute the distance modulus of equation 2.2. This model aims to capture the variability in the spectral energy distribution of SNIa and their evolution over time. Mathematically, it is treated as a linear combination of time dependent spectral templates, multiplied by a time independent

color term. At any given phase p of the explosion, and at wavelength λ , the model prediction for the flux is given by :

$$F(p, \lambda) = x_0 \times [M_0(p, \lambda) + x_1 M_1(p, \lambda)] \times e^{c \times CL(\lambda)} \quad (2.6)$$

Where M_0 and M_1 are time dependent spectral templates, CL is the time independent color law, x_1 is the stretch parameter, c is the color parameter, and x_0 sets the flux scale. M_0 , M_1 , and CL are fixed from one SNIa to the next, and are fit during model training. Note that the color term takes the form of a traditional galactic extinction color law, except that the form of CL is left to be fit from the data. x_0 , x_1 , and c are free parameters and are fit individually for each SNIa. Note that the phase p is defined as time relative to maximum light in the rest frame B band. The SNIa properties are therefore obtained by fitting their lightcurves to equation 2.6. This procedure is summarized diagrammatically on page 32. Note that, to fit a light curve to equation 2.6, one must integrate the flux of equation 2.6 in the observed rest frame bands, and also take into account the time dilation effects of redshifted supernovae. Before being able to do any of that, however, one needs to construct the templates that make up the model. Generally speaking, this process of using a spectrophotometric model of an object to transform its observed broad band magnitudes into rest frame magnitudes is called a **K-correction**.

2.3.3 Overview of Model Training

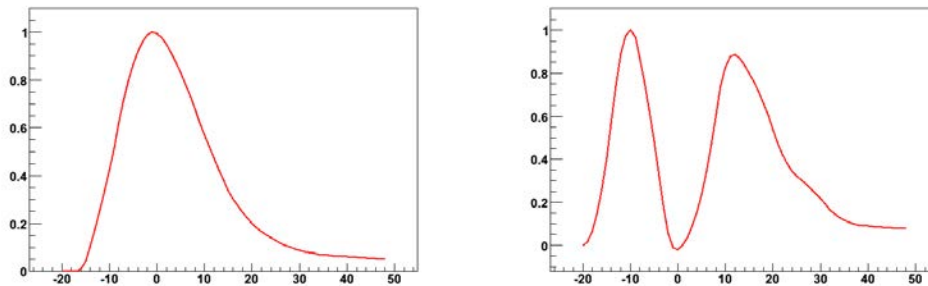
To construct these templates, we require a large amount of both spectroscopic and photometric data, covering a wide range of phases and wavelengths. The training will consist of estimating the parameters x_0 , x_1 , and c for each supernova that entered the training, while simultaneously fitting the M_i and CL templates themselves. Obviously, this requires an initial guess for the value of the templates obtained from a prior training of the model. Note that there is no theoretical limit on the number of M_i that we can fit. We stop at 2 because we find no empirical evidence for an additional correction term in equation 2.2. Note that it has not been ruled out that by adding another component M_2 to the training we could find a significant correlation between the corresponding term x_2 and the supernova brightness. However, to this day, no such correlation has been observed.

From a numerical point of view, the M_i templates are defined on a function basis covering the desired range of p and λ . In the case of SALT2, third order B-splines are used. As for the CL template, it is defined as a third order polynomial with 2 degrees of freedom fixed such that $CL(\lambda_B) = 0$ and $CL(\lambda_V) = 0.4 \ln(10)$ where $\lambda_B = 4450 \text{ \AA}$ and $\lambda_V = 5510 \text{ \AA}$. For a given set of supernova and template parameters, the χ^2 is computed by comparing the input data to the passband integrated model predictions of equation 2.6.

Note that while this comparison is well defined for light curves, this is not the case for spectra. Because most spectroscopic surveys do not have this type of training in mind, the absolute flux calibration and color calibration of the delivered spectra are often unreliable or simply nonexistent. However, these spectra still contain valuable information regarding the shape of various features of SNIa lightcurves. To this end, we recalibrate the spectral information using the photometric data. The spectra are recalibrated by multiplying them by a chosen recalibration function. In the case of SALT2, we have chosen the exponential of a polynomial, to ensure that the recalibrated flux values are positive. The number of free parameters in the recalibration function are limited by either the number of lightcurves, or the wavelength range of the spectra (not more than one parameter per 800 \AA), whichever is smaller.

Now that we have defined a χ^2 , we can fit our model by minimizing said χ^2 . We use the results of an older training method, SALT, as the initial guess for the model parameter values.

We then use a Gauss-Newton algorithm to converge to the optimal set of parameter values. In other words, we assume the χ^2 is a quadratic function of the parameters, and use that to correspondingly update the parameter values. This is done iteratively until the decrease in the χ^2 is considered negligible. This is first done while considering a single component M_0 . We then use the results of that fit as the initial guess for a second fit, this time including M_1 . We fit a color law at both steps. In figure 2.6, we see some typical results for the M_0 and M_1 templates.



(a) Template 0 B-band flux as a function of time. This corresponds to the rest frame B-band lightcurve of a type Ia supernova whose color and stretch values are both null.

(b) Template 1 B-band flux as a function of time. The 2 bumps “stretch” out the lightcurve, making it ramp up and die down slower, hence the name for the corresponding parameter.

Figure 2.6

2.3.4 Accounting for Data Holes

In order to take advantage of all available light curve data, the templates constructed must cover a broad range of wavelengths and phases. However, this leads to poorly constrained areas in the model, given the lack of both spectroscopic and photometric coverage in these areas. More than merely increasing model uncertainties in a given area, this often results in a complete absence of information between 2 nodes of the chosen basis. This obviously leads to a failure of the training process. Decreasing the distance between basis nodes would lead to an unacceptable loss in precision in the well defined regions of the model. The traditional method employed to circumvent this issue is called **regularization**. It consists in adding a smoothness constraint while fitting. Generally speaking, this consists in modifying the χ^2 such that it now becomes :

$$\begin{aligned} \chi_{total}^2 &= \chi_{data}^2 + \chi_{regularization}^2 \\ &= \sum_{components} \left[(D - M)^t C_D^{-1} (D - M) + (M - E(M))^t C_{E(M)}^{-1} (M - E(M)) \right] \end{aligned} \quad (2.7)$$

Where D are the data, C_D their covariance, M the model, $E(M)$ some expected property of the model and $C_E(M)$ its covariance. By properly choosing $E(M)$, this corresponds to adding a term to the χ^2 that penalizes large derivatives at any given point in the model. In areas of the model where this is the only contribution to the χ^2 , the model value will become whichever minimizes the slope between the current node and the surrounding nodes. This becomes clear when considering the various implementations of equation 2.7 in the current SALT 2 code. Considering the notation $M_{i,j} = M(p_i, \lambda_j)$, they can be written as :

Lambda gradient regularization This regularization function smooths the model in the wavelength direction :

$$\chi_{\text{regularization}}^2 = \frac{w}{N} \sum_i^j \left(\frac{M_{i,j+1} - M_{i,j}}{M \times (\lambda_{j+1} - \lambda_j)} \right)^2$$

Phase gradient regularization This regularization function smooths the model in the phase direction :

$$\chi_{\text{regularization}}^2 = \frac{w}{N} \sum_i^j \left(\frac{M_{i+1,j} - M_{i,j}}{M \times (p_{i+1} - p_i)} \right)^2$$

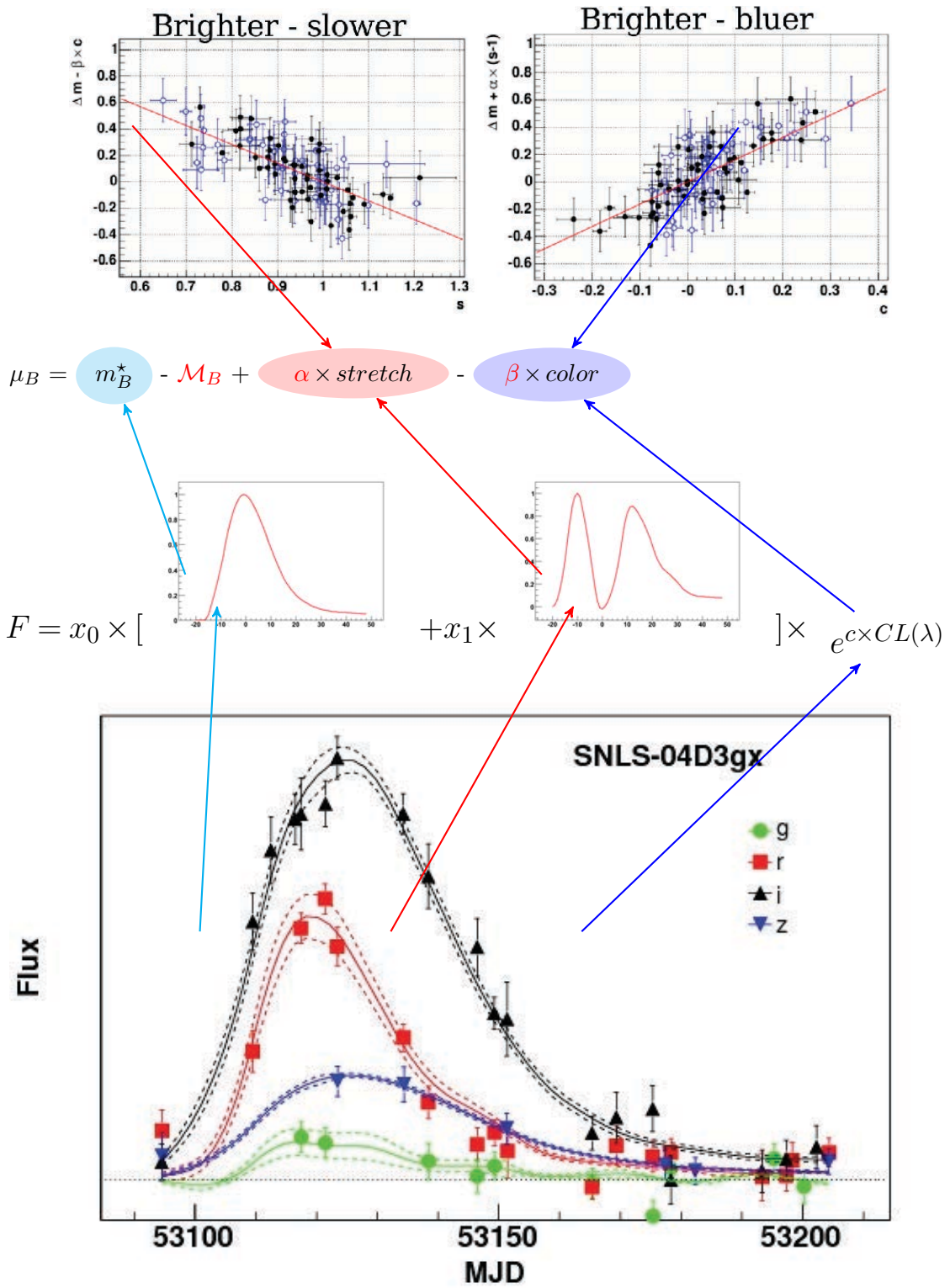
Dyadic regularization This regularization function considers contributions from the derivative in both the wavelength and phase directions :

$$\chi_{\text{regularization}}^2 = \frac{w}{N} \sum_i^j \left(\frac{M_{i+1,j+1}M_{i,j} - M_{i+1,j}M_{i,j+1}}{M^2 \times (p_{i+1} - p_i)(\lambda_{j+1} - \lambda_j)} \right)^2$$

Full dyadic regularization This generalizes the dyadic regularization by allowing one to choose a k and l that will set the phase and wavelength range over which the derivatives are computed :

$$\chi_{\text{regularization}}^2 = \frac{w}{N} \sum_i^j \sum_k^l \left(\frac{M_{i+k,j+l}M_{i,j} - M_{i+k,j}M_{i,j+l}}{M^2 \times (p_{i+k} - p_i)(\lambda_{j+l} - \lambda_j)} \right)^2$$

Note that we have introduced 2 new parameters here : N and w . N merely represents the number of terms in the ensuing sum, whereas w is a normalization parameter. It corresponds to the weight assigned to the regularization. The idea is that w can be tuned such that it is large enough to satisfyingly smooth out ill defined regions of the model, but small enough that its contribution is negligible in the well defined regions. To estimate the effect of this parameter, a simulated data set was used. The training was run on this data set for multiple values of w , until a value was found such that the induced bias on the K-corrections was smaller than 5 mmag for any given wavelength. Despite this, some concerns remain regarding regularization. Namely its ability to both smooth out spectral features in well defined regions (by encouraging small values for the derivative of the model) and introduce features in poorly sampled regions (through ringing effects). These concerns are addressed in the simulations described in section § 6.2.3.



2.4 Hints of New Standardization Parameters

The standardization parameters we have seen so far stand out clearly when training the SALT2 templates. However, recent studies have hinted at other standardization parameters. While the impact of these is not as significant as the stretch and color corrections, understanding them is crucial if we wish to increase the precision of our distance moduli in the coming years.

2.4.1 Spectroscopic Correlations

There are hints that standardization parameters may be found by considering the spectroscopic features of each SNIa. [Bronder et al. \(2008\)](#) claims to have found a correlation between blue band magnitude at maximum and the **equivalent width**⁷ of the SiII line. However, this correlation is due to the correlation between that equivalent width and the stretch of the SNIa. In other words, it does not represent a new standardization parameter, but merely a spectroscopic alternative to a pre-existing one. The variance in the resulting residuals to the Hubble diagram after such a standardization are comparable to those after a stretch correction. [Nordin et al. \(2011\)](#) claims that this equivalent width also correlates with color. Based on analysis of a sample of 55 SNIa, he concludes that the use of the SiII equivalent width as a standardization parameter could slightly decrease scatter in Hubble residuals. These results remain tentative, as they are yet to be reproduced for larger samples.

[Bailey et al. \(2009\)](#) uses **Supernova Factory** (SNF) data to show the existence of a single parameter that can reduce the Hubble scatter of SNIa by 15% relative to a stretch and color correction. The parameter used is the flux ratio $R_{642/443} = F(642\text{nm})/F(443\text{nm})$. However, obtaining such a ratio requires a flux calibrated spectra. Obtaining this to within the precision required for supernova cosmology would require long hours of observation for each supernova, making this standardization prohibitively expensive. In addition, the flux at restframe 642nm exits the wavelength range of ground based optical spectrometers around a redshift of 0.6, greatly limiting the applicability of this standardization.

There are many other papers that one could cite in the quest to standardize supernovae using spectral features. To summarize all of them would be a thesis onto its own as this is a very active area of research that could one day lead to more accurate distance moduli. For the time being, however, such corrections are greatly limited by our instrumental capabilities at high redshift. As such, we do not consider their inclusion in the cosmology analysis of chapter § 6.

2.4.2 Galaxy Dependence

A number of studies ([Kelly et al. \(2010\)](#), [Sullivan et al. \(2010\)](#), and [Lampeitl et al. \(2010\)](#)) have repeatedly confirmed that, after stretch and color corrections, there exists a correlation between intrinsic luminosity variations and the properties of the supernova’s host galaxy mass. The mass itself is likely merely a proxy for the underlying physical mechanism driving the correlation. It is not yet clear with which of a galaxy’s many properties there exists a causal relationship and what that relationship may be. Indeed, since the initial discovery, this same correlation between Hubble diagram residuals and host galaxy properties has been expressed using different host galaxy properties :

⁷The equivalent width of an absorption line is defined as the width that a rectangular absorption line would need to have to absorb the same total amount of light, assuming total absorption within that width.

- [Gupta et al. \(2011\)](#) have determined the mass of the host galaxies of the SDSS-II sample using UV and near infrared photometry. They find a clear correlation between SNIa intrinsic luminosity and host galaxy mass.
- [D’Andrea et al. \(2011\)](#) used galactic spectra to determine metallicity and star formation rates. They find that SNIa intrinsic luminosity correlates with both of these.
- [Childress et al. \(2013\)](#) and [Pan et al. \(2014\)](#) find the same correlations at low redshift using the data of the **Supernova Factory** (SNF) and the **Palomar Transient Factory** (PTF). They also find that SNIa color correlates with host galaxy metallicity.
- [Rigault et al. \(2013\)](#) reviewed the same SNF and PTF data, but focusing on the properties of the immediate environment of the supernova. They distinguished 2 populations : those in H $_{\alpha}$ emitting regions, and the rest, dubbed “neutral” environments. They find a difference in absolute magnitude between the two populations of -0.094 ± 0.031 *after* stretch and color corrections.

It is not known which of these many indicators should be used as an additional parameter in correcting the distance modulus, because they all correlate strongly with each other. Further studies are required to determine which of the galactic parameters is the causal agent, and which are only proxies for that causal agent. For now, as we shall see in more detail in section § 6.3.1, we follow the procedure of [Conley et al. \(2011\)](#) and [Betoule et al. \(2014\)](#) and implement a step correction based on two populations of supernovae based on their host galaxy mass.

As our measurements of the distance modulus becomes more precise, it will be more and more important to gain a better understanding of this effect. Indeed, if the galaxy mass is only a proxy for the underlying mechanism (which it likely is), then any redshift evolution in the adequacy of the mass as a proxy would bias our cosmology.

Chapter 3

Overview of the Supernova Legacy Survey

In this chapter we will present the Supernova Legacy Survey (SNLS). It is on the data provided by this survey that most of my thesis rests on. The objective of this chapter is to give the reader a complete understanding of the steps required to transform the photons of distant objects into the science images that will be used for the cosmology analysis. We begin with a broad overview of the complete science analysis of the photometric data in section § 3.1, before delving more deeply into its technical details in the remaining chapters. Indeed, it is difficult to grasp the stakes of each step in the analysis without first having an idea of its role in the complete analysis. We then present the broader survey of which the SNLS is a part in section § 3.2. Then, in section § 3.3, we focus on the specific observation strategy followed when collecting the data used by the SNLS. We then present the instrument used and its various subcomponents in section § 3.4. Finally, in section § 3.5, we discuss the image preprocessing that is required before we can move on to the photometry measurements.

3.1 Overview of the Science Analysis

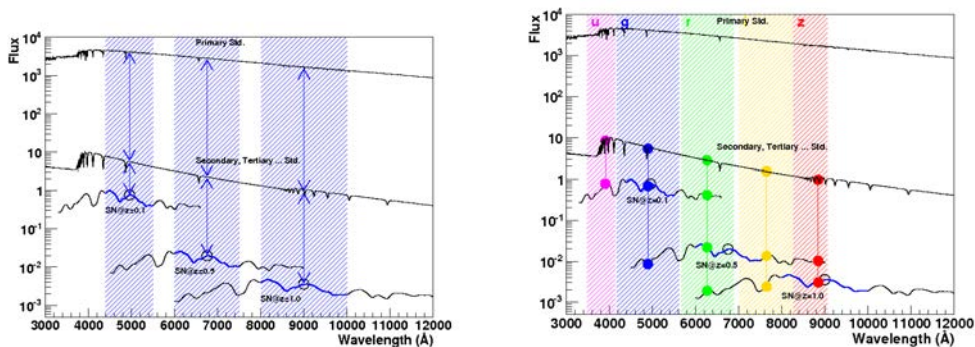
3.1.1 Photometry in Different Bands

The first step of the analysis consists of obtaining the light curves of each supernova in each band in which it has been observed. We will explore this process in great detail in the next chapter. It is the precision of these measurement that ultimately carry the most weight in determining the uncertainty on the distance modulus. If SNIa were not redshifted, then these measurements could be directly compared with one another, and the relative calibration from band to band would be of no use to us. However, since SNIa are redshifted, we would not be comparing the same intrinsic luminosity. We define the standard luminosity to be the integrated luminosity emitted by the supernova in its rest frame blue band. This intrinsic band will correspond to a different wavelength range for our observations. We must therefore inter-calibrate these measurement by anchoring them to a well understood standard star, as seen in figure 3.1a. This process is described in detail in section 5.1.1.

However, the actual passbands available to us do not correspond to the redshifted blue bands. That would require us to construct one filter per supernova. As we have seen, it is for this reason that we require a light curve fitter.

3.1.2 The SALT2 Light Curve Fitter

Once we have obtained the light curve of a supernova from multiple bands, it is possible to fit it to a parametrized model of the supernova’s **Spectral Energy Distribution (SED)**. We have described in detail how to construct such a model in section 2.3. Using this estimator for the SED of the observed supernova, we can conclude as to its observed magnitude in its rest frame blue band, and its correction parameters, stretch and color, as shown in figure 3.1b.



(a) The primary star is an object whose SED is well measured and well understood. Through a series flux calibration transfers, we can compare the blue band magnitudes of supernovae at different redshift.

(b) The passbands available to us are fixed. Hence, we use the calibrated measurements in each passband to fit a calibrated SED model of the supernova. This, in turn, is what will allow us to compare the blue band magnitudes of supernovae at different redshift.

Figure 3.1: The objective is to compare the supernova fluxes highlighted in blue. The left hand figure shows us how to calibrate fluxes, whereas the right hand figure shows the necessity of a spectrophotometric model of SNIa.

3.1.3 The Cosmology Fit

Once we have determined the m_B (blue band magnitude), stretch, and color parameters for all supernovae in our sample, we are ready to fit a Hubble diagram. In doing so, we fit the values of α and β simultaneously with the cosmological parameters. Because the value of the distance modulus depends on α and β , its final values are not obtained until the cosmology fit, and the distance estimator of each supernova will actually slightly depend on the model we choose to fit. The free parameters are fit using a straightforward χ^2 minimization. We also construct ellipses in parameter space by estimating the χ^2 of the fit for values around the central value found.

3.2 The CFHT Legacy Survey

The **Canada-France-Hawaii Telescope (CFHT)** is a jointly operated telescope located in Hawaii, near the summit of Mauna Kea. Here we describe the survey from which SNLS draws its data, namely, the **Canada-France-Hawaii Telescope Legacy Survey (CFHTLS)**. France and Canada jointly decided to allot over 2300 hours of their observation time over a 5 year period (from mid 2003 to early 2009). This is roughly 450 nights of observations. Preliminary calibration and image pre-processing also took place at the CFHT. Subsequent data processing

took place at [Terapix](#). Finally, the **Canadian Astronomy Data Centre** (CADCC) took charge of storing and releasing the final data products.

The survey itself is subdivided into 3 surveys, each deeper but narrower than the last. In all 3 cases, all observations were made using the wide field optical imager MegaCam, which we will describe in more detail in section 3.4.5. Here, we will look at the 3 different subsurveys and their respective scientific objectives. A complete collection of all refereed publications using CFHTLS data can be found at [the CFHTLS paper repository](#).

3.2.1 The “Very Wide” Survey

The “Very Wide” survey covers an area of 410 square degrees, all contained inside a 4 degree band centered on the ecliptic. The primary objective of this survey was to provide a wide sample of images covering the transneptunian regions of our solar system, leading to a great deal of discoveries in the realm of Kuiper belt objects [Petit et al. \(2011\)](#). The survey was conducted in the g, r, and i bands. Given that some extra solar objects were visible in the images, this color information helped to glean stellar properties from this extra solar data, in particular for white and brown dwarfs. This survey was therefore also useful for studies of our own galaxy [Sesar et al. \(2011\)](#).

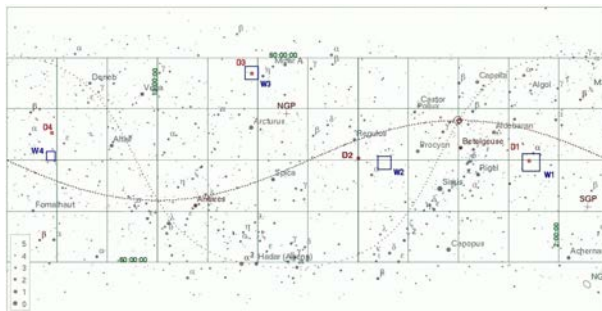


Figure 3.2: Location of the wide and deep fields in the night sky.

3.2.2 The “Wide” Survey

The wide survey covers a smaller area of 155 square degrees, spread out over 4 patches of varying size (from 25 to 72 square degrees), called W1, W2, W3, and W4 (see figure 3.2). All 5 bands are used for this survey (the u, g, r, i, and z bands), reaching a depth of 24.5 in magnitude in i band. Such images allow us to probe large areas of the low redshift universe, and even of our own galaxy. They are used to study local stellar populations, individual galaxies and clusters through their photometric and morphological properties, and finally to allow direct probing of the large scale structure of the universe through weak lensing and galaxy distributions, as done in [Hildebrandt & on behalf of the CFHTLenS collaboration \(2014\)](#).

3.2.3 The “Deep” Survey

The “Deep” survey provides the images used by the SNLS. It covers 4 patches of sky, each of 1 square degree, called D1, D2, D3, and D4 (see figure 3.2). The patches are located high in the galactic plane so as to minimize local extinction of the incoming light (see table 3.1). They are also chosen such that 2 of them are visible to the CFHT at any given time of the year. This survey also used all 5 available bands. The total observing time for each band is provided in

table 3.2. Due to its general unreliability, we choose to discard the u band for the SNLS analysis, especially given that the u band is so extinct and so blue its contribution to the determination of high redshift supernova parameters is minimal.

Table 3.1: Central coordinates of the CFHT Deep Survey fields. An estimated average value of Milky Way $E(B - V)$ is given using the Schlegel et al. (1998) maps, which will be discussed further in section § 6.3.4.

Field	RA	DEC	$E(B - V)$
D1	02:26:00.00	-04:30:00.0	0.027
D2	10:00:28.60	+02:12:21.0	0.018
D3	14:19:28.01	+52:40:41.0	0.010
D4	22:15:31.67	-17:44:05.0	0.027

As we will see in section § 3.3.1, such a long integration time is part of a search strategy meant to detect transient phenomena that appear between one image and the next. At the end of the 5 years, the CFHTLS Deep Survey had provided photometric images of 450 spectroscopically confirmed type Ia supernovae. In section § 3.5.1 we will see in more detail what data is released alongside the science images, and what pre-processing these have already undergone. These images will not only serve us for our supernova survey, but have also been used with other scientific objectives in mind such as cosmic shear studies (Semboloni et al. 2006) or high redshift structure studies (Mazure et al. 2007).

Table 3.2: Total integration time of the deep survey in different bands, *for each field* i.e. the total time allotted to the survey is 4 times what is shown.

band	u	g	r	i	z
time (in hours)	33	33	66	132	66

Furthermore, such long integration times over the same patch of sky can be used to create extremely deep stacked images of the science fields. By carefully excluding supernovae and other transient events before stacking, we can recover the original shape and brightness of very high redshift galaxies, providing insight into early galaxy and star formation. The production of such stacks is discussed in the soon to be released Hardin (2015).

3.3 Observation Strategy

Because SNLS uses CFHT Deep Survey images, we dedicate a section to understanding the survey strategy employed along with the accompanying observations essential to our scientific objective.

3.3.1 A Rolling Search

The SNLS is a rolling search. This means that we revisit the same field in rapid succession in order to find transient events. Every deep field run lasts about 18 days, when the moon is least bright in its cycle. At every run, 2 fields are simultaneously observed, so that each is observed every other night. Observations are made using either r and i band, or g and z band, depending on the lunar contribution to the background sky level.

After each night of observations, the images are scanned for signs of new transient events, some of which may be SNIa. As a check, two separate detection pipelines are put in place. In both cases, the goal is to compare the most recent image from a stack of earlier images, and to detect an excess of flux compatible with a point source (given the image’s **Point Spread Function** (PSF)). One pipeline uses the Alard algorithm described in [Alard & Lupton \(1998\)](#), whereas the other uses a non parametric approach. Detections from both pipelines overlap at the 90% level.

The number of transient events detected is far too large for all of them to be followed up spectroscopically, an essential observation if we are to confirm that the object is indeed an SNIa. Therefore, we use photometric methods to rank the most promising candidates before requesting spectroscopic follow up. On the one hand, we use the available images to fit a light curve model to the data, thus discarding many core collapse supernovae. An example of the light curve data collected during run time and the corresponding fits can be seen in figure 3.3. We also try to match the detection with previous ones, stored in a database. Indeed, **Active Galactic Nuclei** (AGN) and **variable stars** can flare up periodically. If a match is found, we store this new detection in the database and do not consider the event to be an SNIa candidate. After these cuts, we are left with a much more manageable sample of SNIa candidates.

3.3.2 Spectroscopic Follow Up

In order to confirm that we are indeed looking at type Ia supernovae, spectroscopic confirmation is required. This also gives us the redshift of the observed object, an essential measurement for constructing a Hubble diagram. Three sets of telescopes participated in these follow up observations, seen in figure 3.4. Here we review these telescopes and their capabilities briefly, as described in [Cellier-Holzem \(2013\)](#).

3.3.2.1 The VLT

The VLT telescope is a **European Southern Observatory** (ESO) telescope situated in the Southern hemisphere (in Chile). It was used to observe the D1, D2, and D3 fields. A total of 480 hours of VLT observing time was dedicated to the SNLS survey. For this reason, nearly half (about 200) of our confirmed SNIa sample comes from the VLT. The following papers describe the VLT spectroscopic data :

[Balland et al. \(2009\)](#) for the first, second, and third years.

[Cellier-Holzem and the SNLS collaboration \(in prep.\)](#) for the fourth and fifth year.

3.3.2.2 The Gemini Telescopes

The Gemini Telescopes are situated on opposite hemispheres (specifically, in Hawaii and Chile). Hence, between them, they have access to all 4 CFHT Deep Survey fields. The GMOS spectrograph, described in [Hook et al. \(2004\)](#), was used for measuring SNIa candidate spectra. They provided SNLS with 160 spectroscopic confirmations of type Ia supernovae, out of a total of 200 candidates. They preferentially observed high redshift candidates so as to exploit their *nod-and-shuffle* algorithm ([Glazebrook & Bland-Hawthorn 2001](#)). It consists of repeatedly positioning the spectroscopy slit on and off the observed object, and with each such motion transferring the collected charges that correspond to the object’s spectra to another area of the CCD. As such, during the same observation, the CCD will contain both the spectrum of the background sky and the measured object itself. This allows for a sky subtraction of much

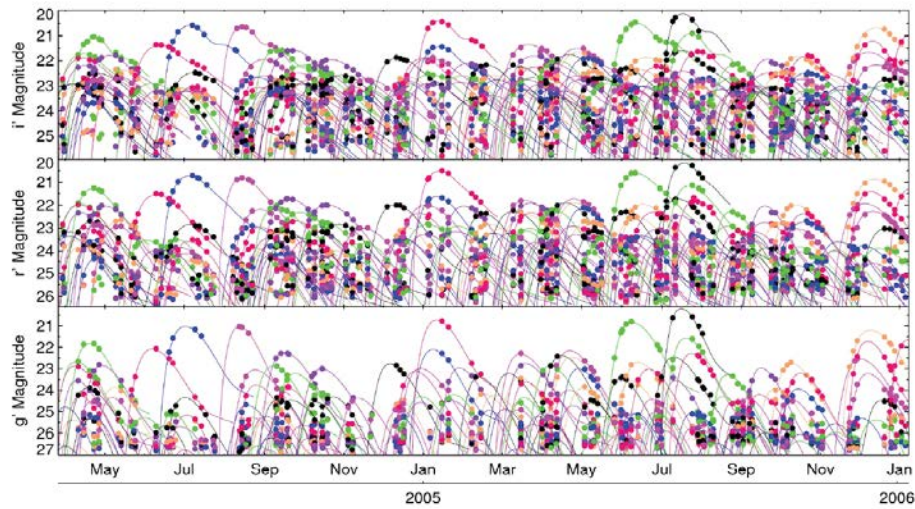


Figure 3.3: SNIa candidates, detected between May 2004 and January 2006, and their brightness in g, r, or i band as a function of time.

greater quality. This, combined with GMOS's high sensitivity in the red, allows it to go to higher redshifts than would otherwise be possible. The resulting data are described in :

[Howell et al. \(2005\)](#) for the first year.

[Bronder et al. \(2008\)](#) for the second and third years.

[Walker et al. \(2011\)](#) for the fourth and fifth years.

3.3.2.3 The Keck Telescopes

The Keck telescopes, being situated in the Northern hemisphere (Hawaii), were used to observe the D3 field. They provided 80 spectroscopic confirmations of type Ia supernovae, out of a total of 100 candidates. These were centered around a redshift of 0.5, as this was the optimal redshift range to analyze the ultraviolet properties of SNIa, a parallel objective of the Keck observations. The Keck data are described in :

[Ellis et al. \(2008\)](#) for the first and second years.

Fakhouri and the SNLS collaboration (in prep.) for the third, fourth, and fifth years.

(a) The **Very Large Telescope (VLT)** in Chile.(b) The **Keck I** and **Keck II** telescopes in Hawaii.(c) The **Gemini South** telescope in Hawaii.(d) The **Gemini North** telescope in Chile.

Figure 3.4: Telescopes used for spectroscopic confirmation of SNIa candidates for the SNLS.

3.4 MegaPrime

We now switch back to CFHT and describe in more details the imaging instrument. The instrument itself is made up of a series of components, collectively referred to as MegaPrime. In this section, we give a brief technical summary of each component, taken from [the CFHTLS website](#).

3.4.1 The Upper End

The “Upper End” is the name given to the metallic structure that holds the apparatus together. In addition to housing the various other components of MegaPrime, it also provides a temperature controlled environment for all electronics onboard, including the MegaCam camera. The upper end alone weighs 3000kg, and reaches a weight of 5700kg with all other components installed.

3.4.2 Wide Field Corrector

The quality of the outgoing image from the telescope’s main mirror is unsatisfactory to the level required by the survey. In particular, the field’s edges present significant distortions. To this end, a series of 4 spherical lenses are placed along the optical path. They are collectively referred to as the “Wide Field Corrector”. Their properties are an important component of the optical path model discussed in section § 3.4.7.



Figure 3.5: The MegaPrime instrument (from [the CFHTLS website](#)).

3.4.3 Image Stabilizing Unit

Telescope vibrations or atmospheric variations require high frequency corrections to the optical path in order to maintain a stable image. To this end, a small (48cm) glass plate is placed in front of the camera which can be tilted along an axis. These tilts displace the image on the focal plane in such a way as to counter any destabilizing effects.

3.4.4 Guiding and Focus

There are two important motions that MegaPrime needs to be capable of. The first concerns a change that occurs *within* a single exposure : the motion of the science field across the night sky. In order to follow it, the instrument follows a bright star called a **guide star**. CFHT actually uses 2 guide stars, each with a dedicated guider. The guiders are used to correct for any deviations by ensuring that the guide stars remain centered as MegaPrime chases the deep field across the night sky. An important element that changes *between* different exposures is the actual focal distance of the telescope. This is due to dilations of the mirror induced by temperature variations and small changes in the shape of the instrument due to mechanical tension. A model was developed to take into account both of these effects. The model is constrained through observations of a **focal star**. Once the new focal length is computed, the camera can actually move along the focal path, changing its distance from the mirror.

3.4.5 MegaCam

To meet the technical requirements of such an ambitious survey required the largest CCD mosaic ever built at the time, and a camera capable of housing it. In figure 3.6 we see the CCD mosaic and its corresponding numbering scheme as it was laid out in MegaCam. The technical specification of the CCDs are as follows :

Number of CCDs : 36 actually used in the mosaic, though a total of 40 were built, laid out in 4 rows each containing 9 columns.

CCD dimensions : 2048×4612 pixels

Pixel size : $13.5\mu m$, corresponding to 0.185 arcseconds on the sky

Focal ratio : $F/4.1$

Total image size : 340Megapixels across the whole mosaic

Required temperature : $-120^{\circ}C$

3.4.6 Around MegaCam

The CCD mosaic is housed in a cryostat which provides it with the required $-120^{\circ}C$ operating temperature. In addition, the readout electronics are designed so as to operate as quickly as possible in order to minimize wasted readout time in between exposures. To this end, each CCD is actually split in two, each half having its own amplifier, so as to halve readout time. The filters are housed in a filter wheel that allows us to quickly change the observed pass band in between exposures. Finally, we also need a shutter to open and close the camera so as to have control over the total exposure time. We summarize the technical specifications of these various components below :

Field of view : $0.96\text{deg} \times 0.94\text{deg}$

Readout time : 35 seconds

Readout noise : under $5 e^{-}$

Shutter diameter : 1 meter

Minimum exposure time : 1 second, guarantees uniformity of illumination of $10ms$ across the focal plane

Filter wheel : Contains up to 8 filters, though only 5 are used

Filter change time : 2 minutes

3.4.7 Modeling the Optical Path

The optical path can be characterized as an effective series of lenses, as seen in figure 3.7. Constraining the properties of this path and its impact on the observations comes down to determining the properties of this effective model, from the properties of each individual lens to their relative positions, as well as aberrations that may occur along the line of sight. The study of this optical path was the subject of the PhD projects [Villa \(2012\)](#) and [Guyonnet \(2012\)](#).

One method of constraining this model is known as the **DICE** method. It consists of illuminating the focal plane with a series of LEDs at various wavelengths. Of note is that this LED is placed close enough to the focal plane that it cannot be approximated as an infinitely distant source. To understand the significance of this, we first consider what occurs when observing distant sources.

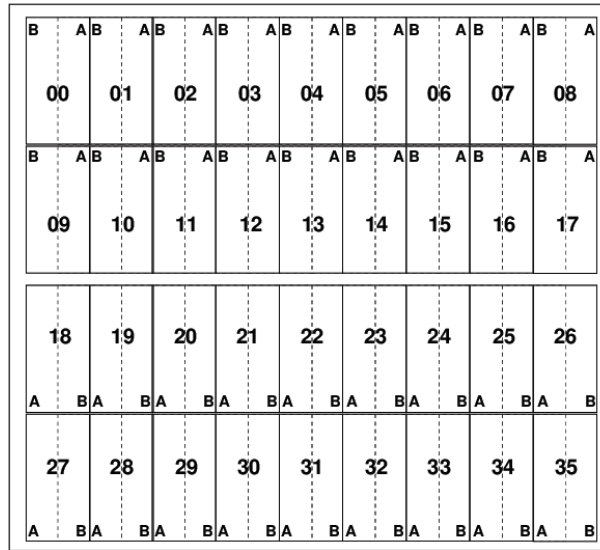


Figure 3.6: Arrangement and numbering scheme of the CCD mosaic. **A** and **B** correspond to the 2 amplifiers used during readout. Taken from [Terapix](#).

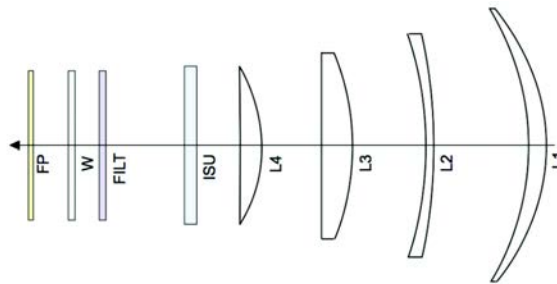


Figure 3.7: Effective model of the optical path within the MegaPrime instrument. The model’s free parameters include the properties of each lens, the distance from one lens to the next, and also an offset between the lens center and the central axis, in order to model the impact of misalignment of the various components. Taken from [Villa \(2012\)](#).

When observing distant objects, we can consider that at any given wavelength the incoming light from a given object can be approximated as a plane wave. Obviously, the optical path is designed such that all parallel light rays end up on the same point on the CCD (i.e. a photon’s final destination on the CCD only depends on its angle of entrance into the optical path). Hence each pixel on the CCD represents all possible optical paths from the object to that point. Conversely, when we consider a nearby source, the opposite is true. Each light ray will enter the optical path at a different angle, and therefore end up at a different pixel on the CCD. This means that each pixel on the CCD is the result of one (or a few in the case of reflections) optical path from the LED to the CCD. Thus, the resulting patterns on the CCD (as see in figure 3.8) constrain the inner workings and reflections of the optical path.

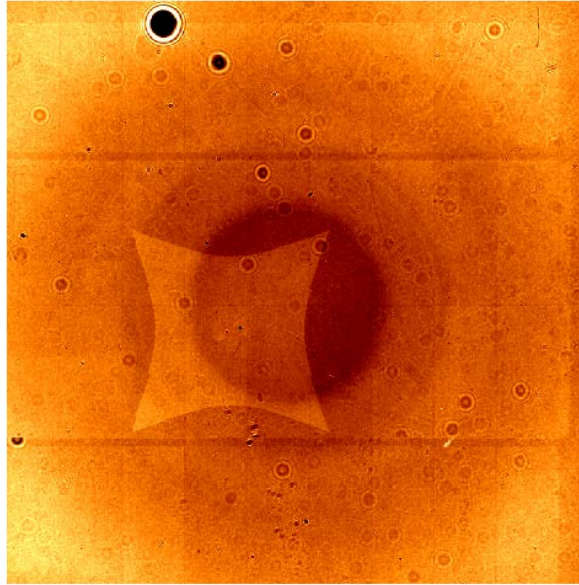


Figure 3.8: Example of the end result on the CCD of illumination of the focal plane by a given LED. The deformed square near the middle is the result of inner reflections. Taken from [Villa \(2012\)](#).

3.5 Overview of the Data Flow

Once the data is acquired, it must undergo a significant amount of processing before it can be used for supernova cosmology. In this section, we present an overview of these steps, categorizing them depending on whether they take place on site at the CFHT, or “locally” prior to the cosmology analysis.

3.5.1 Preprocessing at CFHT

Pre-processing of the images is performed on site using the Elixir pipeline, making the images immediately available to the detection algorithms discussed in section § 3.3.1. Indeed, the detection algorithms require us to be able to align the latest image to some reference image, as well as have at least a rough idea of the relative calibration between the two images. Beyond its use in detection algorithms, the objective of this first round of processing is to disentangle instrumental effects from actual science data. This is referred to as detrending. The data delivered by this step consists of :

- A pixel mask map, which flags pixels that are thought to be faulty.
- A so called “dark frame” obtained by reading out the CCDs after a completely dark exposure.
- A flat field image that maps non uniformities in the photometric response of the CCDs.
- Fringe pattern maps for the i and z bands.

- Sky subtracted images for all bands.
- Saturation maps.
- Cosmic ray flags.

The flat field maps are obtained by observing the sky during twilight hours. The twilight provides a uniform lighting across the field of view. A series of such exposures are taken. The final flats are the result of stacks of such exposures, where outlier exposures have been visually discarded. The aim of such images are to incorporate the spatial non-uniformities of the instrumental response for a fixed illumination. The observed non uniformities are on the order of 15% when comparing the central value to the outer areas of the field of view. The flat shapes essentially follow a circular pattern due to the process with which the filters are tinted. The images delivered have already been multiplied by the corresponding flat value.

The sky level is computed by masking all pixels thought contain significant portions of star or galaxy light. The sky level is then determined to be the average value of the remaining pixels, and is subtracted from the entire image.

The saturation maps are produced simply by flagging all pixels that are at 98% of the saturation level. Unfortunately, this was done *after* the flat field corrections were applied, which means that the actual value of saturated pixels varied across the sky. For this reason, we could not reliably count on these saturation maps. Instead, stars containing saturated pixels were eventually identified using the quality of their flux fit.

3.5.2 Local Processing

After receiving the data from the CFHT, a few more processing steps are required before the images become useful for further analysis :

1. SExtractor is used to create a catalog of objects present in the image.
2. Satellites leave long bright trails in the image. These are identified using a simple algorithm, and the corresponding pixels are flagged as unusable.
3. We need to compare the sextractor catalog of each image to a catalog of stars whose positions are known. This gives a first approximation as to the WCS ([Calabretta & Greisen 2000](#)) of the image, and allows for rudimentary position transformations between images.
4. We are now ready to compute the **Point Spread Function** that describes the point sources in our image. This process is explained in detail in section § 4.1.3. In short, we select only those objects whose Gaussian second moments cluster into an area of circle like objects, and use them to fit an elliptical Moffat function. This step also provides a rudimentary first estimate of the flux of the stars in the image.
5. A rudimentary calibration is obtained by comparing these fluxes to the calibration catalogs. This is useful in order to identify and exclude particularly extinct images.

After this image per image processing, we are ready to analyze the image stacks as a whole. Before moving on to photometry, we need to :

1. Compute the proper motion of stars in the sky.
2. Compute the lightcurves of all tertiary calibration stars present in the images.
3. Average the flux value of these lightcurves, discarding variable stars in the process.
4. Compare the obtained fluxes with the calibration catalog magnitudes in order to compute zero points.

These steps are described in detail in the next chapter.

Chapter 4

PSF Photometry of Dim Supernovae

Photometry is the process of transforming the image of a supernova into a number that corresponds to that image's brightness. The challenges of supernova photometry are twofold : on the one hand, supernovae are dim objects and thus can have very low S/N ratio, on the other, they are explosions that take place within galaxies and thus their luminosity must be disentangled from that of their host galaxy. The definitive version of the photometric techniques used to address these challenges in SNLS can be found in [Astier et al. \(2013\)](#). Here we present a comprehensive review of the methods described in that paper.

In section § 4.1, we begin with a more in depth look at the steps presented at the end of the last chapter, namely the image preprocessing required prior to being able to perform accurate photometric measurements. Afterwards, in section § 4.2, we will present the photometry algorithm used by our analysis. In section § 4.3 we conclude by looking at simulations that aim to verify the linearity of our method.

4.1 Local Image Preprocessing

CFHT images are released after being processed on site by the Elixir pipeline ([Magnier & Cuillandre 2004](#)). The objectives of this pipeline are twofold. On the one hand to produce and apply flat field images obtained using twilight images, and on the other to correct for fringe patterns in the i and z bands. While these data products are a good start, more image preprocessing is required before our PSF photometry algorithm can be applied. Note that not all images used are part of the official CFHT Legacy Survey data sample, given their poor quality. Rather than use only those images included in CFHTLS, we consider all CFHT deep images and apply our own quality cuts. These are :

- Reject all images whose **image quality** (IQ), as defined below in 4.2, is above 3.5.
- Reject all images whose atmospheric extinction is 2 magnitudes greater than the average.

4.1.1 Sky Subtraction

The first step is to subtract the background sky level of all images. We use SExtractor ([Bertin & Arnouts 1996](#)) to compile a preliminary image catalog. The sextractor routine delivers an

image where each pixel is given a number corresponding to its associated object. This is known as a “segmentation map”. We enlarge the image patches associated with each object by 5 pixels, producing a mask for each image. Assuming that the unmasked pixels are dominated by the sky luminosity, we use these to compute the sky level, again using SExtractor. This sky level is subtracted from the images, and from hereforth it is to be assumed that we work with sky subtracted images. At this point, we are ready to investigate the objects detected.

4.1.2 Star Catalog

It is important to have a catalog of stars for each image. These will be used to compute both the PSF of each image and its **zero point**, an important calibration quantity which we will explore in the next chapter. We distinguish stars from other objects by computing gaussian second moments. The second moments of the Gaussian weighting function are iteratively adjusted to the ones of each object, i.e. the matrix of weighted second moments should satisfy :

$$\vec{M}_g = 2 \frac{\sum_{pixels} (\vec{x}_i - \vec{x}_c)(\vec{x}_i - \vec{x}_c)^T W_g(\vec{x}_i) I_i}{\sum_{pixels} W_g(\vec{x}_i) I_i} \quad (4.1)$$

$$W_g(\vec{x}_i) \equiv \exp \left[-\frac{1}{2} (\vec{x}_i - \vec{x}_c)^T \vec{M}_g^{-1} (\vec{x}_i - \vec{x}_c) \right]$$

where \vec{x}_i are pixel coordinates, \vec{x}_c the Gaussian weighted centroid, and I_i is the (sky subtracted) image value at pixel i . This is equivalent to a least squares fit of a 2D-Gaussian, so long as the noise is the same for every pixel in the object. We therefore choose to compute these second moments by ignoring the object contribution to the variance, which is flux dependent. This means that the offset produced by a 2D-Gaussian’s inability to perfectly reproduce the PSF will not be flux dependent, and will shift the computed second moments uniformly across the flux range.

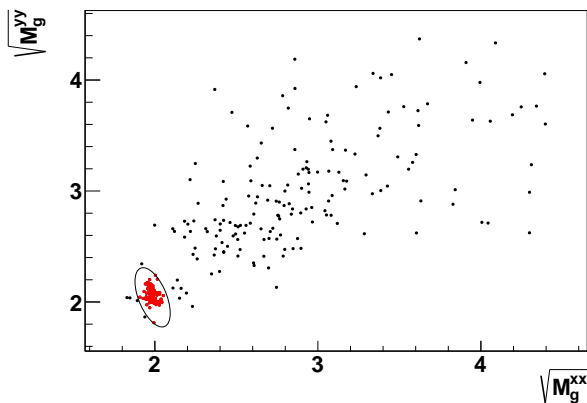


Figure 4.1: Gaussian-weighted second moments from a single typical image, with the found star clump and the star selection (red points within the ellipse).

In figure 4.1, we see the distribution of second moments in the (M_g^{xx}, M_g^{yy}) plane. Note that we do not expect all stars to have exactly the same shape given the variation of the PSF across the image. Hence, stars are not defined by a single point on this plane, but rather by a dense area of points. The shape and limitations of this clump is itself determined using a 2D-Gaussian in the (M_g^{xx}, M_g^{yy}) plane. Stars are selected by only including objects within the 5σ ellipse of

the fitted gaussian. Using the average second moment matrix, we are now ready to define image quality as :

$$\sigma_{IQ} \equiv \sqrt[4]{\det(\bar{M})} \quad (4.2)$$

We compute the WCS of each image by using the obtained gaussian weighted positions, and comparing them to a deep stack of the SNLS images, itself anchored using the USNO catalog. This is useful for first order image to image position transformations.

4.1.3 PSF fitting

Now that we have a collection of objects we can reliably count on as being stars, we are ready to fit the PSF. Moffat (1969) provides a suitable analytical description of PSFs. We choose to complement this description with a pixellized correction meant to take into account guiding errors and other aberrations. The PSF model used is therefore a combination of these 2 elements, whose free parameters are fit using the identified stars on the image. We therefore have one PSF model per image. This is the same strategy adopted in Stetson (1987). The analytical component, referred to as an elliptical Moffat function, is given by :

$$\begin{aligned} P(x, y) &= A [1 + r^2]^{-\beta}, \\ r^2 &\equiv w_{xx}x^2 + w_{yy}y^2 + 2w_{xy}xy \\ A &\equiv \frac{\beta - 1}{\pi} \sqrt{w_{xx}w_{yy} - w_{xy}^2} \end{aligned}$$

We set the value of β as 2.5. The parameters w_{xx} and w_{yy}, w_{xy} and the values of the pixellized correction are fit as a linearly varying function across the image in both the x and y directions.

4.1.4 Astrometry

Stars are known to move significantly across the sky. This is obviously a problem if not taken into account, as an error on the position of a star will lead to a systematic underestimation of its flux. This problem is exacerbated by the fact that the brightest stars, and therefore the most heavily weighted during calibration, are also the closest ones, whose proper motions correspond to more significant angular shifts over time. It also becomes more significant as the length of the survey increases. For the 3 year analysis, the induced effect was at the edge of acceptability. For the 5 year analysis, correcting for it becomes essential. This motion must therefore be computed before we can proceed with flux estimation. Because our photometry method will estimate fluxes *and* positions using a certain PSF model, the astrometric catalog is computed using coordinates obtained through the same PSF model, as opposed to some other estimator of position (such as a gaussian centroids).

Each image series (i.e. collection of images in the same field, band, and CCD) contains about 200 stars, which leads to about 50,000 position measurements across the series. WCS transformations allow us to transform positions from one image to another within subpixel precision, which is enough to identify stars with themselves across images. We therefore use the relative position of stars from one image to the next to fit a proper motion vector. The position P_{ij} of a given star i in image j is no longer static in time, and instead becomes :

$$\vec{P}_{ij} = T_j(\vec{X}_i + \vec{\mu}_i(t_j - t_0)) \quad (4.3)$$

where T_j is the coordinate mapping from a reference system to pixels in image j , \vec{X}_i refers to the coordinates of star i in this reference system, $\vec{\mu}_i$ the proper motion of this star, t_j the epoch of image j and t_0 some reference epoch. t_0 is chosen as the mean date in the image series. The reference image is chosen as being that with the best image quality. The free parameters of this fit are therefore T_j (one per image), \vec{X}_i , and $\vec{\mu}_i$ (one per star). The transformations T_j are quadratic polynomials in x and y . We did not go to higher degree polynomials as it led to nearly no improvement in the residuals. We can intuitively guess at a major degeneracy in the fit. Namely, we can add any chosen proper motion uniformly across all stars, as this would lead to the same relative position of the stars across the image series. If the transformations T_j are linear (which they very nearly are), we can even generalize this degeneracy further by adding any proper motion whatsoever to any star and compensating for it in the transformation. Formally speaking, this means that one can always operate the following substitution and our fit would have no way of telling the difference :

$$\begin{aligned} T_j(\vec{X}_i) &\leftarrow T_j(\vec{X}_i + (t_j - t_0)g(\vec{X}_i)) \\ \vec{\mu}_i &\leftarrow \vec{\mu}_i - g(\vec{X}_i) \end{aligned}$$

where g is any arbitrary function. This degeneracy is resolved by imposing that certain stars are fixed on the sky. We could have chosen instead to use galaxy positions, but chose not to as this is an ill defined concept that would most likely be sensitive to PSF modeling errors. The fit begins by assuming that all stars are fixed, and iteratively allows one star at a time to move so long as this halves its contribution to the χ^2 . This is done until all stars have converged into their final status of fixed or moving. The uncertainties estimated are a combination of 2 elements. On the one hand we propagate the shot noise from the PSF position measurements. On the other, we added a position noise floor of 0.013 pixels after noticing that the shot noise was inadequate at describing the position residuals of bright stars. The position RMS around the fitted value and a comparison to the estimated uncertainty can be seen in figure 4.2. Note that, as we shall see in equation 4.5, we can calculate the flux bias induced by such a position RMS. Plugging in the highest observed position RMS (about 0.06) and using a good image quality of 1 (which increases the bias), we find that the induced flux bias is still under 10^{-3} . Indeed, for most images, it is expected to even be on the order of 10^{-4} .

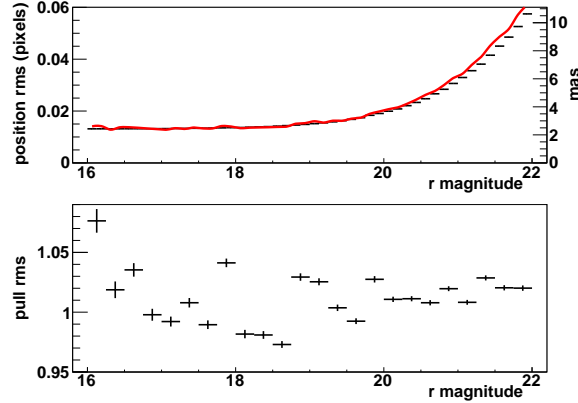


Figure 4.2: Astrometric 1-D residuals scatter as a function of star magnitude for the D3 field in r band. The top plot compares, as a function of magnitude, the measured residual RMS (points) with the average expected RMS (curve) including a noise floor of 0.013 pixels. They are roughly compatible, but not necessarily equal because the expected RMS varies with IQ at fixed magnitude. The bottom plot displays the RMS of the residual pulls (i.e. residuals in unit of expected RMS), which are close to 1 at all magnitudes. We hence conclude that adding the position noise floor of 0.013 pixels (2.4 mas) in quadrature to the position uncertainty expected from shot noise fairly describes the residuals. This figure only considers residuals along y for reasons explained in section § 4.2.3.

4.2 Direct Simultaneous Photometry

4.2.1 Algorithm

For the SNLS3 analysis, images were resampled prior to a photometric fit taking place. This was to get all images in the astrometric frame prior to fitting the position and flux levels of the measured objects. We refer to this as **Resampled Simultaneous Photometry** (RSP). In SNLS5, the fit resamples the model internally rather than taking as input resampled images. We call this **Direct Simultaneous Photometry** (DSP). There are several advantages to DSP, namely :

- Avoid resampling pixels thereby removing the unaccounted for covariances in your data.
- Save storage space by only needing the original images on disk.
- Have a more wieldy image processing pipeline. Since resampled images depend on the image to image transformations, any modifications to those transformations do not require a complete recomputation of the resampled images.

In DSP, we model the estimated flux for image i at pixel p as :

$$M_{i,p} = \left[f_i \times \phi_i(\vec{x}_p - T_i[\vec{x}_{obj}]) + G \left(T_i^{-1}(\vec{x}_p) \right) \otimes K_i + S_i \right] R_i \quad (4.4)$$

where f_i is the object flux in image i , ϕ_i the PSF function in the same image, T_i is the coordinate transformation to the reference image (defined in Eq. 4.3), G is the galaxy pixelised model for

the PSF of the reference image, K_i the convolution kernel that matches the PSF of the reference to the one of image i (at the object position), S_i is the sky level in image i , R_i the photometric ratio of the reference to image i , and \vec{x}_{obj} is the coordinate of the object (in the reference frame). The output parameters of the fit are therefore f_i , G , S_i and \vec{x}_{obj} . The convolution kernels K_i are fitted by comparing the shape of the PSFs of the reference image and the image i . The R_i are computed internally prior to the fit of the other parameters by comparing the fluxes of the same stars across images. Those fluxes were obtained during PSF modeling. Uniform photometric ratios over a CCD are an adequate assumption because we have found a high correlation of photometric ratios of different CCDs within an exposure. Because the stars are spread throughout the image, the approximation does not induce a flux bias, but rather merely contributes a small random error to the flux estimator. This error is bounded by the ~ 6 mmag reproducibility of bright star fluxes which we will see more closely in section § 4.3.5.3. Note that because we include this photometric ratio in our model, the flux estimators produced are in units of reference image ADUs. For this reason, as we will see in the next chapter, we only need to calibrate one image per image series.

4.2.2 Preserving Linearity

To ensure the validity of our calibration measurements, a central concern of high precision photometry is to maintain the linearity of the flux estimator. As we will come to understand in the next chapter, the absolute scale of the flux estimator is itself irrelevant, and is perfectly equivalent to a redefinition of the calibration zero points. For this reason, we are particularly sensitive to any flux dependent elements of our algorithm. With this in mind, we explore 2 potential mechanisms that may induce errors in our flux ratios.

Guy et al. (2010) discusses the effects of position uncertainty on PSF flux estimates. Here we would like to summarize the key points of that discussion. For a Gaussian PSF, it can be shown that a position error underestimates the flux by:

$$\frac{\Delta f}{f} = \frac{1}{4} \frac{\delta x^2 + \delta y^2}{\sigma_{TQ}^2} \quad (4.5)$$

which is quadratic in the position error. It therefore does not average out from one measurement to another, and leads to a systematic bias inherent to PSF photometry. More generally, a PSF flux estimation on a single image suffers from a bias at low S/N:

$$E[\hat{f}] \simeq f \left\{ 1 - \frac{\text{Var}[\hat{f}]}{f^2} \right\} \quad (4.6)$$

where the approximation obviously breaks down when S/N approaches 1. Since we have to cope with measurements of SNe at low S/N (we occasionally deal with $S/N < 1$), we impose a single common position on all images. Since we are concerned by the accuracy of flux ratios, the tertiary stars should also be measured imposing a common position, so that they are affected by inaccuracies of coordinate mappings between images in the same way as SNe.

Secondly, including the shot noise of an object while fitting its flux also leads to non-linearities in the flux estimator. Here we will explore this in depth, explaining why this is so and what can be done about it. First, consider the least-squares PSF flux estimator :

$$\hat{f} = \frac{\sum_i w_i P_i I_i}{\sum_i w_i P_i P_i} \quad (4.7)$$

where P is the PSF, I is the sky-subtracted image, w denotes the pixel weights in least squares, and the sums run over pixels. The statistically optimal weights read $w_i^{-1} = \text{Var}[I_i] = \text{Var}[sky] + kfP_i$, where k is the ratio of a pixel content to its shot noise variance, usually the inverse of the gain. For a faint source, this leads to $\hat{f} \propto \sum_i P_i I_i$, whereas for a bright source we get $\hat{f} \propto \sum_i I_i$, so that the relative weights of image pixels I_i vary with source brightness. Flux ratios are then accurate only if the PSF model is faithful. Setting $w_i^{-1} = \text{Var}[sky]$ preserves the statistical optimality for faint sources and makes flux ratios independent of the accuracy of the PSF model, at the expense of a suboptimal flux estimator for brighter sources. Since the flux ratio uncertainty is dominated by the uncertainty of the fainter source, and we have several tertiary stars for each SN, we settled for $w_i^{-1} = \text{Var}[sky]$ for *both* the photometry of SNe and tertiaries. Note that the reason for assuming a stationary noise when estimating Gaussian second moments (Eq. 4.1) is essentially the same.

We however use the optimal pixel weights (i.e. account for all noise sources including the object itself) when modeling the PSF (§4.1.3), in order to obtain a PSF model as faithful as possible. It is worth stressing that there is a systematic difference between using $w_i^{-1} = \text{Var}[sky] + kfP_i$ (where the Poisson noise is estimated using the fitted model) and $w_i^{-1} = \text{Var}[sky] + kI_i$ (where the Poisson noise is estimated using the flux value at each pixel) in expression 4.7, although these two expressions should agree on average. With the second expression, the flux estimator becomes seriously non linear with respect to pixel values I_i and this leads to unacceptable flux biases, analogous to the ones described in Humphrey et al. (2009).

To this end, and again as we have previously done, we deliberately ignore the contribution of the measured object to the noise when estimating fluxes, in order to ensure linearity, independently of the fidelity of the PSF. As a consequence, the flux uncertainties obtained from the second derivatives of the χ^2 at minimum are underestimated. The parameters, and their actual uncertainties read :

$$\begin{aligned}\hat{\theta} &= (A^T W A)^{-1} A^T W D \\ \text{cov}(\hat{\theta}\hat{\theta}^T) &= (A^T W A)^{-1} A^T W \text{cov}(D D^T) W^T A (A^T W A)^{-1}\end{aligned}\quad (4.8)$$

with $\chi^2 = (A\theta - D)^T W (A\theta - D)$, and :

\mathbf{W} is the weight matrix actually used in the fit.

\mathbf{D} is the data vector.

θ is the vector containing the model parameters.

\mathbf{A} is the design matrix, i.e. $E[D] = A\theta$.

In standard least squares, we would have $W^{-1} = \text{cov}(D D^T)$, and $\text{cov}(\hat{\theta}\hat{\theta}^T) = (A^T W A)^{-1}$, which is the minimum variance bound. Since we have chosen $w_i^{-1} = \text{Var}(Sky)$, this leads to a suboptimal fit, as indicated by the Gauss-Markov theorem, but we find that the loss in precision is insignificant. Indeed, comparing both uncertainty estimators at fluxes typical of tertiary stars indicates an average increase of around 2.5% above the minimum variance bound.

4.2.3 Effects of Refraction

Depending on the position in the sky of the observed field, and the time of observation of each image, the measured light will enter the atmosphere at a different angle, leading to shifts in the observed position of objects. These are given by :

$$\delta x = [n(\lambda) - 1] \tan z \sin \eta \quad (4.9a)$$

$$\delta y = [n(\lambda) - 1] \tan z \cos \eta \quad (4.9b)$$

where $n(\lambda)$ is the refraction index of the atmosphere, z is the zenith angle and η is the parallactic angle, the direction of the refraction-induced displacement in the image plane. These formulae are obtained by taking advantage of the fact that, for MegaCam, x and y are well aligned with right ascension and declination. In table 4.1, we present the average value and RMS of the distributions of $\tan z \sin \eta$ and $\tan z \cos \eta$ within each image series. The effects of these refractions are noticeable on two fronts.

Field	$E[\tan z \cos \eta]$	$\sigma(\tan z \cos \eta)$	$E[\tan z \sin \eta]$	$\sigma(\tan z \sin \eta)$
D1	0.031	0.46	0.48	0.04
D2	-0.049	0.49	0.36	0.043
D3	0.11	0.53	-0.59	0.056
D4	-0.075	0.38	0.79	0.031

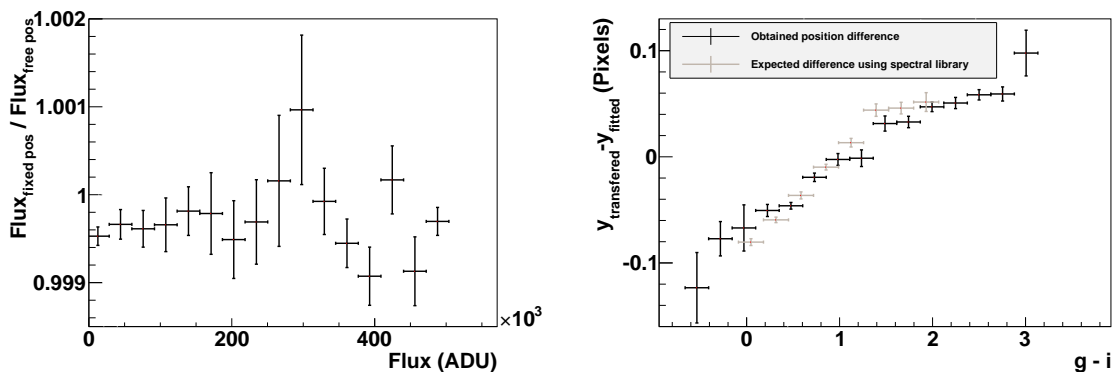
Table 4.1: Average and standard deviation of $\tan z \cos \eta$ and $\tan z \sin \eta$ across all fields. Note that within the same field the values are very similar from band to band.

First, the RMS of the distribution of $\tan z \sin \eta$ or $\tan z \cos \eta$ will contribute to the RMS in the observed position of a star *within the same image series* (i.e. for the same passband). As expected from table 4.1, we do indeed find that the RMS in the x position of stars is systematically greater than in the y position. This is not particularly problematic, for as we have seen in section § 4.1.4 the position RMS of stars has a negligible impact on its photometry.

Second, the difference in the average value of either $\tan z \sin \eta$ or $\tan z \cos \eta$ from one band to the next will lead to a difference in the average observed position of the star *between different image series* (i.e. for different passbands). This is a problem because a significant difference between supernova and tertiary star photometry comes from the fact that the supernova position is not fitted in g and z bands due to the expected low S/N. Instead, we transfer the fitted position from the r and/or i bands. To transfer the supernova position from, for example, r to g , we evaluate the position of stars in both astrometric catalogs at the epoch of the reference image in g band using the fitted proper motions, fit the geometric transformation that maps r positions to the ones in g , and apply this transformation to the supernova position in r band. We then fit the supernova in g at this fixed position. To ensure that this does not lead to significant differences between supernova and tertiary star photometry, we do the same for a sizable number of tertiary stars (more precisely : all tertiary stars in g band in the D1 field). In other words, we compute light curves for these stars at fixed positions using their fitted position in r band, after transferring it in the same way we do for supernovae. We then compare the light curves obtained with those fitted in the regular way, i.e. fitting both fluxes and position. In figure 4.3a, we find that the transformation incurs a flux underestimation of about 4×10^{-4} independently of the flux of the object considered. In comparing the difference between the fitted position in g band and the transferred position from r band, it is clear that the difference is dominated by

the y coordinate term. In figure 4.3b, we see a clear trend between the discrepancy in y and the color of the star, pointing to a refraction effect.

Because for the SNLS we have that $E[\tan z \cos \eta]$ is much greater than $E[\tan z \sin \eta]$, we can understand why, recalling equations 4.9a and 4.9b, the effect is much greater along y than along x . In table 4.1, we have seen the expectation values and RMS of $\tan z \cos \eta$ and $\tan z \sin \eta$ across all fields (note that the values are the same for all filters). We find that we do not expect the effect to be much more significant in other fields, and other bands are less affected. Using the Pickles (1998) spectrophotometric library of typical stars, and computing the atmospheric refraction shifts for a standard Mauna Kea air column at $\tan z \sin \eta = 0.48$, we are able to reproduce the slope displayed in figure 4.3b, which adequately reproduces the observed shift, confirming our understanding of the observed flux underestimation.



(a) Ratio of the fitted flux at fixed position to the fitted flux with free position as a function of flux. We see no clear flux dependence in the flux underestimation resulting from the transformation.

(b) Difference between the fitted position in g band and the transformed position from r band as a function of color. This is done for all stars in the D1 field. We also plot the expected difference obtained by computing the atmospheric refraction shifts for the stars in Pickles (1998).

Figure 4.3

4.3 Validations with simulations

4.3.1 Simulation goals

As we will understand in more detail in the next chapter, the fundamental requirement of supernova photometry is the preservation of flux ratios between field stars and supernovae. We therefore designed a simulation whose aim is to ensure that this ratio is maintained across a wide range of photometric conditions. In particular we want to ensure that :

- Fitting a galaxy model during supernova photometry does not induce any biases. Indeed, galaxy fitting is the only algorithmic difference between supernova and tertiary/calibration star photometry.
- Flux ratios are properly recovered over a wide enough range of IQ and S/N.

- After tuning some aspects of the uncertainty model, it properly describes the observed scatter.
- Sampling the galaxy model at the same spatial sampling as the images is fine enough.

Note that we also run this simulation for both RSP and DSP.

4.3.2 Simulation method

The simulation consists in modifying real SNLS science images by adding so called **fake stars** to them. These fake stars are constructed by copying and pasting image stamps of bright, high quality photometric stars, dubbed model stars, onto a nearby galaxy after being appropriately dimmed. We translate the model star by an integer number of pixels before pasting, thus avoiding any shortcomings of resampling. Note also that the time window during which the fake supernova is turned on is randomly selected. We also add a Poisson noise at each pixel based on the pasted flux level. At variance with many other tests of supernova photometry (such as Schmidt et al. (1998) and Holtzman et al. (2008)), this copy-paste method is independent of PSF modeling¹, astrometric mappings, and photometric ratios between images, and hence might detect the effects of improper estimates of these inputs.

The idea, then, is to test a photometry by its ability to reproduce the photometric factor used to dim the model star. To construct a model and fake star pairing, this cut and paste procedure is applied to the model star on each image in the image series. As the RSP photometry runs on aligned images, one can translate the pixels of the model star by the same amount on all images and is guaranteed to always land on the same position on the sky. For the DSP photometry, this is clearly not the case, and we must be careful to select unaligned (and therefore un-resampled) images that are, by sheer happenstance, very nearly aligned up to a translation. Otherwise, the same pixel displacement vector going from the model star would lead to a different position on the sky. The underestimation of the flux as a result of a position error, for a Gaussian PSF, is given by equation 4.5. Given a rotation between 2 images of angle $\Delta\theta$, a relative difference in image stretching noted $\Delta\lambda/\lambda$ and a displacement vector \vec{v} between the model and fake star, equation 4.5 can be rewritten as:

$$\frac{\Delta f}{f} = \frac{1}{4} \left(\frac{\|\vec{v}\|}{\sigma_{seeing}} \right)^2 [(\Delta\theta)^2 + (\Delta\lambda/\lambda)^2] \quad (4.10)$$

We use equation 4.10 to select bunches of consecutive images such that they yield a difference in flux under the 10^{-3} level if $\|\vec{v}\| = 100$ pixels. Fake stars constructed with a larger value for $\|\vec{v}\|$ are not considered in the analysis. We indeed find un-rotated successive image bunches because CFHT enjoys an equatorial mount and the camera (which has no rotation capability) is usually mounted on its top end once for a whole dark-time run. The fake stars are only pasted during these lunations, leaving their flux at 0 for the remaining images, thereby simulating top-hat lightcurves for these fake “supernovae”. Note that to avoid correlations, we only cut and paste one fake star per galaxy per lunation. For this simulation, we use r-band images in CCD 13 of field D1, in CCD 11 of field D2, and in CCD 12 of field D4. The chosen CCDs are near the center of the CCD mosaic. We end up with a total of 1181 fake stars constructed using 121 model stars.

¹Note that this is only true if the PSF is constant across the image, but the variations are known to be small enough that for the small displacements incurred during the cut and paste their induced effect is negligible.

4.3.3 Expected biases

4.3.3.1 PSF spatial variation bias

We expect a small simulation-induced bias as a function of displacement from model to fake star due to variations in the PSF as we move across the image. Indeed, the fake star generation process cuts a star with a given PSF and pastes it in a location where the PSF is slightly different. The induced bias as a result of this is given by:

$$\frac{\hat{f}}{f} = \frac{\sum_{ij} PSF_{ij}(\vec{x}) PSF_{ij}(\vec{x} + \vec{v})}{\sum_{ij} PSF_{ij}^2(\vec{x} + \vec{v})} \quad (4.11)$$

Because the change in the PSF model is linear by construction with respect to position in an image, expression 4.11 depends linearly on \vec{v} . To directly observe this bias, we run simulations with a photometric ratio of 1 and avoid adding Poisson noise. We also compute the expected trend using equation 4.11 for a wide range of \vec{v} summed across all images used during the simulation. The trend expected by direct computation matches the one observed for simulations, and the effect is clearly linear in \vec{v} . This bias is well below the 10^{-3} level for typical \vec{v} used during the simulation. Furthermore, the bias disappears when one averages over \vec{v} directions. We hence did not take any action to account for the PSF variation from model to fake star positions in our simulations.

4.3.3.2 Low S/N bias

We have seen in § 4.2.2 that PSF flux measurements are biased at low S/N, due to position uncertainties. When a common position is fitted for a source in an image series, the bias is lower but does not disappear. For a flux measurement on a single image i of flux f_i , the S/N ratio is defined simply as the ratio of f_i to $\sigma(\hat{f}_i)$. For a light-curve of any shape, the least-squares estimator of its amplitude A has a variance that satisfies:

$$\frac{A^2}{\text{Var}[\hat{A}]} = \sum_i \frac{f_i^2}{\text{Var}[f_i]} \quad (4.12)$$

where f_i is the expected flux in each image.

In appendix B of [Guy et al. \(2010\)](#), it is shown that the bias of \hat{A} follows the same law as for a single image (described in Eq. 4.6), namely:

$$\frac{\text{E}[\hat{A}]}{A} \simeq \left\{ 1 - \frac{\text{Var}[\hat{A}]}{A^2} \right\} \quad (4.13)$$

For the noisiest supernovae observed, this is expected to correspond to a bias of a few per mil. To make precision tests of the photometric accuracy at low S/N we need to take into account this bias. The photometry's ability to reconstruct the photometric ratio will therefore be tested as a function of its S/N, as defined in equation 4.12. To detect any remaining bias, we fit equation 4.13 with an additional constant offset term b :

$$\frac{\hat{r}}{r} - 1 = -\frac{1}{(S/N)^2} + b \quad (4.14)$$

where r is the flux ratio used during the cut and paste, \hat{r} the reconstructed flux ratio, S/N is the signal to noise ratio of the entire lightcurve (and not just of a single flux measurement), and b is a free parameter.

4.3.3.3 Model star correlations

Because the same model star is reused in multiple model fake star pairing, we take into account possible correlations induced by this repetition and their impact on the simulation's precision. To do this, we increase the uncertainty on the model star flux until the χ^2 per degree of freedom becomes 1 when fitting equation 4.14. We find that we must add 1% uncertainty to the DSP fluxes of the model star, and 0.8% to the RSP fluxes. Note that these added uncertainties are only used when we want to take into account the correlations induced by reusing the same model star. These uncertainties are irrelevant when looking at the dispersion within the same lightcurve in order to investigate the accuracy of our uncertainty model, as we will do in section 4.3.5.3.

4.3.4 Simulation parameters

We compare the fake star's simulated parameters with those of real supernovae, measured during the SNLS 3-year analysis in order to ensure that the simulation tests the photometry in a wide range of realistic conditions. In figure 4.4 we show density plots in the plane of the ratio of the galaxy flux to the supernova flux as a function of the supernova S/N for both real data and the simulation. The galaxy flux is defined as the integral of the galactic flux weighted by the PSF. For a galaxy model $G(i, j)$, this is computed as :

$$F_{gal} = \frac{\sum_{i,j} PSF_{\bar{x}_{SN}}(i, j) \times G(i, j)}{\sum_{i,j} PSF_{\bar{x}_{SN}}(i, j) \times PSF_{\bar{x}_{SN}}(i, j)} \quad (4.15)$$

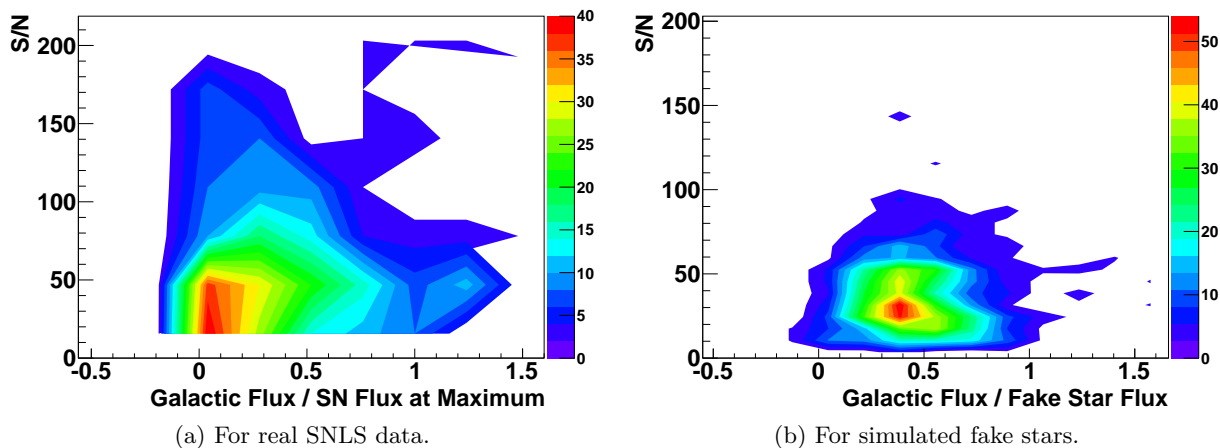


Figure 4.4: Above are density plots comparing the distribution of real supernovae and simulated fake stars in the plane of S/N of the supernova lightcurve VS the ratio of the galaxy flux to the supernova flux at maximum.

In figure 4.4, we compare density plots in the plane of galactic flux VS signal to noise. With this comparison, we see that the distribution of simulated parameters resembles that of real data, however with more galaxy flux on average in simulations than in real data. This helps

in detecting possible shortcomings of fitting a structured galaxy. We recall that the images used during fake star photometry are the same as those used for SNLS photometry, and we can therefore be confident that the simulation closely mimics the observing conditions of supernova photometry.

In addition to selection factors that are aimed at mimicking the supernova population, we perform cuts necessary for proper analysis of the simulation results. A number of model stars used turned out to be variable stars. These are cut from the analysis. We also cut all fake stars generated using a photometric factor above 0.1 so that the original Poisson noise of the model star becomes negligible compared to that added to the fake star during the cut and paste. Finally, model stars that are catalogued as having a significant proper motion are also cut, because the DSP photometry will take into account their motion but not that of the corresponding fake supernova.

4.3.5 Results

4.3.5.1 Photometric accuracy of RSP

We begin by analyzing the results for the RSP. This technique was used for measuring the SNLS supernovae reported in [Astier et al. \(2006\)](#), [Guy et al. \(2010\)](#), and [Betoule et al. \(2014\)](#). In figure 4.5, we see the result of fitting equation 4.14 to the photometric ratios obtained. We find that this method overestimates the flux of supernovae by a factor of $(1.75 \pm 0.83) \times 10^{-3}$. This bias has not been found to depend on galactic flux, model or fake star flux, star color, or IQ. A number of tests were performed in an attempt to determine its origin. These are:

- Reducing the vignette size used by RSP. A change would indicate that pollutions in the vignette are causing the flux bias, but the bias remained.
- Keeping the photometric factor at 1, and pasting the fake star on a dark patch of sky. We then compare the photometry of the fake star with and without a galaxy fit. A difference would indicate that flux transfers between fitted galaxy and fitted supernovae are causing the bias. No significant difference was observed.
- Fitting the flux average of the RSP fake star lightcurve using the covariance matrix produced by DSP, to see if the error model of RSP was biasing. The bias remained.
- Switching to i band. Again, the bias remained. The bias for the i band alone is $(1.95 \pm 1.84) \times 10^{-3}$. While this measurement alone is nearly compatible with 0, the null hypothesis fluctuation would mean that the i band bias fluctuated in the same direction as the r band bias.

We cannot rule out that the observed bias is a statistical fluctuation of the simulations at the 2σ level. Nevertheless, we recommend adding a correlated 1.75×10^{-3} relative systematic uncertainty to this data set, which amounts to less than 1/3 of the photometric calibration uncertainty.

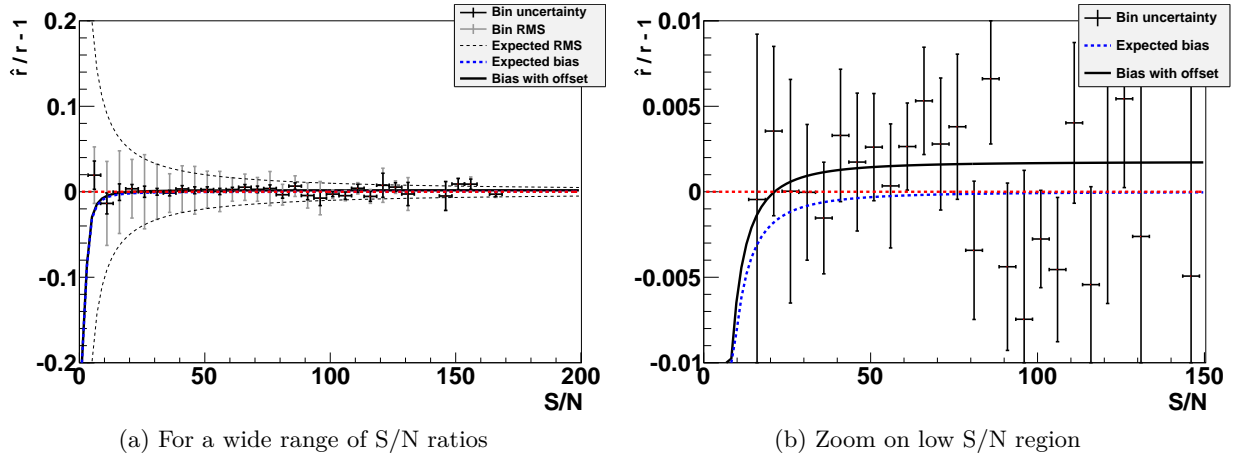


Figure 4.5: Photometric factor accuracy as a function of S/N for the RSP method. We have binned the estimated \hat{r}/r in S/N bins. We plot both the uncertainty on the bin mean as well as the dispersion in the bin so as to compare it to the expected dispersion at that S/N . We also plot the expected S/N bias, as well the obtained fit for equation 4.14.

4.3.5.2 Photometric accuracy of DSP

From this section on, the results refer to those obtained using the DSP method. We begin by fitting equation 4.14 to the data. The fit is seen in figure 4.6. We find that no offset exists beyond the 10^{-3} level. The fitted offset value is $(0.12 \pm 0.9) \times 10^{-3}$.

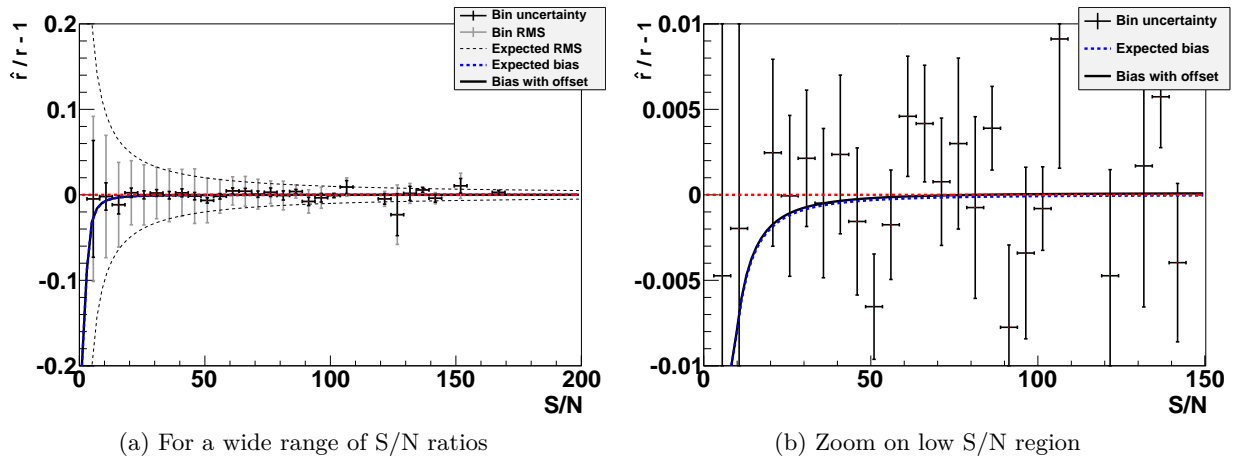
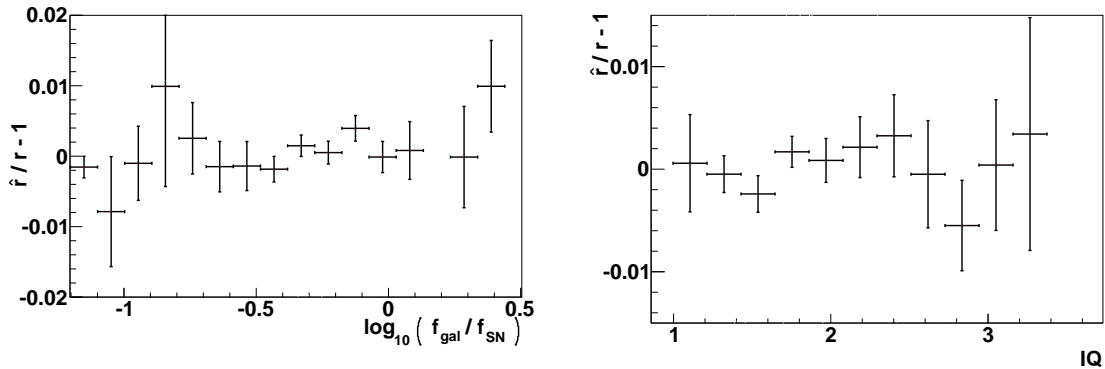


Figure 4.6: Photometric factor accuracy as a function of S/N for the DSP method. We have binned the estimated \hat{r}/r in S/N bins. We plot both the uncertainty on the bin mean as well as the dispersion in the bin so as to compare it to the expected dispersion at that S/N . We also plot the expected S/N bias, as well the obtained fit for equation 4.14.

Field star and supernova photometry differ most crucially in that during the supernova fit we also fit a galaxy model. We therefore also investigate photometric accuracy as a function of galactic flux, as defined in equation 4.15. In figure 4.7a we look at the evolution of photometric

accuracy as a function of galactic flux *after* we have corrected for the S/N ratio bias. No significant remaining bias is observed.

Finally, we also find that preservation of flux ratios does not vary with image quality, as shown in figure 4.7b. Again, the S/N ratio bias is corrected prior to investigating any bias as a function of IQ.



(a) Here we consider photometric accuracy as a function of galactic flux. No significant bias is observed. (b) Here we consider photometric accuracy as a function of image quality. No significant bias is observed.

Figure 4.7

4.3.5.3 Photometric uncertainty results

The output covariance matrix includes the Poisson noise of the sky and the signal itself (both star and galaxy if present), as described in equation 4.8. We assume that there exists an additional quadratic term which describes contributions to the variance coming from errors in the PSF model, the photometric ratio, and/or the residual photometric non-uniformity in the images. The variance therefore takes the form:

$$V_{flux} = V_{sky} + \frac{1}{G}F + \beta^2 F^2 \quad (4.16)$$

where G is the gain in e^- per ADU. To estimate the value of β , we use the photometry of bright (non variable) tertiary stars. For such stars, we assume that the $\beta^2 F^2$ term dominates the variance. Fitting a linear relationship between the RMS of a high flux light curve and its average flux should therefore yield the value of β . In figure 4.8, we see the result of the fit, for which we obtain $(5.6 \pm 0.1) \times 10^{-3}$. This is essentially identical to the repeatability of 6 mmag for aperture measurements on the same data set reported in section § 4.1 of [Betoule et al. \(2013\)](#). We therefore attribute most of this noise floor to flat fielding rather than photometry techniques.

We check that the fitted value is accurate in the low flux regime of the fake supernova. To do so, we compare the squared RMS of their light curves with the estimated variance before and after adding a quadratic correction. Note that because the galaxy flux contributes to the variance, we look at the evolution of the variance as a function of the sum of the fake star and galaxy fluxes. This is seen in figure 4.9. We see that the fitted quadratic term is compatible with data at these low fluxes, but is also almost negligible for such dim objects. For actual SNLS supernova, this leads to a noticeable but small increase in the χ^2/N_{dof} when computing their nightly average flux at redshifts of 0.3 and less, as seen in figure 4.10. Such nightly fits assume

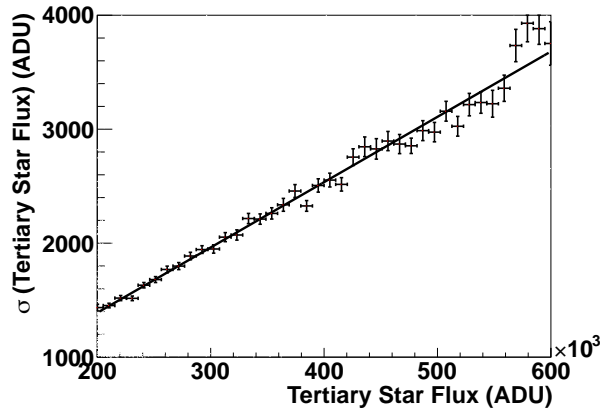


Figure 4.8: Standard deviation of flux estimates over the lightcurve as a function of the average flux. The relation is shown here for high-flux field stars, and we see a clear linear relationship, indicative of a contribution to scatter beyond shot noise from the sky and the object.

that the supernova flux is constant in a single night, which is true enough relative to the flux uncertainty of supernovae.

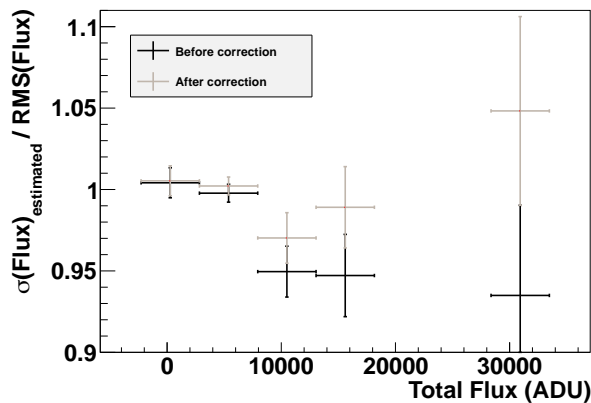


Figure 4.9: We plot here the ratio of the modeled uncertainty to the RMS of the light curve, as a function of the sum of the fluxes of the fake star and galaxy. The two set of points refer to before and after adding a β term to the model uncertainty (Eq. 4.16). We see that the correction makes only a small difference.

4.3.5.4 Position reconstruction results

By assuming that the position fit of the model star is perfectly accurate, we can conclude that the actual position of the fake star is that of the model plus the displacement vector used during fake star construction. We are therefore able to compare the fake star's fitted position with what we can reasonably assume is the correct one. In figure 4.11, we plot the ratio of the error on position computed in this way to the average seeing in the image sample in which the fake star was generated versus the S/N ratio.

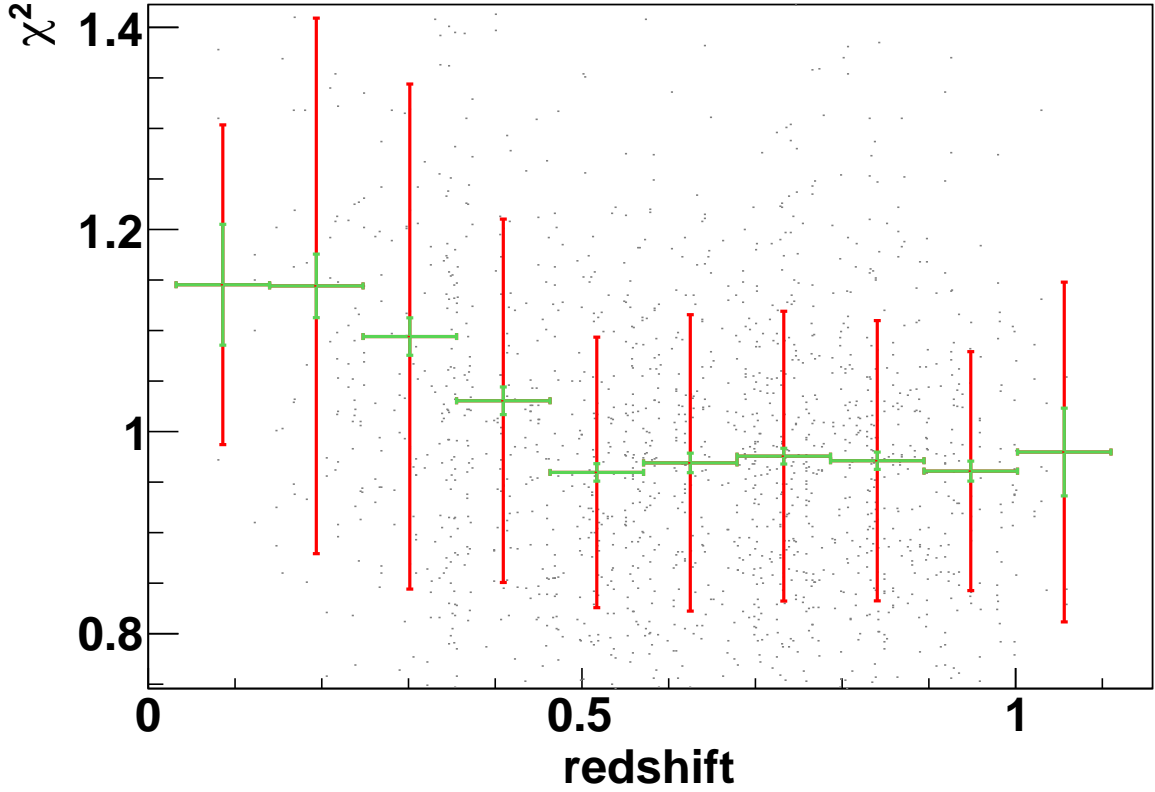


Figure 4.10: Evolution of χ^2/N_{dof} of night fits of real SNe as a function of redshift.

We have also plotted the expected relationship between the two, using a slightly modified version of equation 4.5 that allow for a form factor. This is because equation 4.5 is valid only for a gaussian PSF. When allowing for a form factor F , equation 4.5 becomes :

$$\mathbb{E}[\hat{f}] = f \left\{ 1 - F \times \frac{(\Delta x)^2 + (\Delta y)^2}{4\sigma^2} \right\} \quad (4.17)$$

To find the value of F , we use the exact expression for the flux estimator expectation for any given PSF model which is :

$$\mathbb{E}[\hat{f}] = f \frac{\overbrace{\int PSF(x,y)}^{\text{Data}} \overbrace{PSF(x - \hat{\delta}_x, y - \hat{\delta}_y) dx dy}^{\text{Fitted PSF}}}{\int PSF^2(x,y) dx dy} \quad (4.18)$$

We then compute equation 4.18 numerically for a range of displacements using the PSF model of the reference image. When fitting equation 4.17 to the results, as seen in figure 4.12, we obtain $F = 0.788$. Note, however, that because the actual relation cannot be perfectly approximated by a linear correction to equation 4.5, the form factor will depend on the displacement range in which we choose to fit it. In addition, this linear correction will first underestimate then overestimate the flux bias, as expected from figure 4.12, and as observed in figure 4.11.

Of note is that while the position errors do roughly follow the expected trend, a few outliers remain. We attribute these to be due to model stars affected by significant proper motions that have not been flagged as moving during simultaneous astrometry.

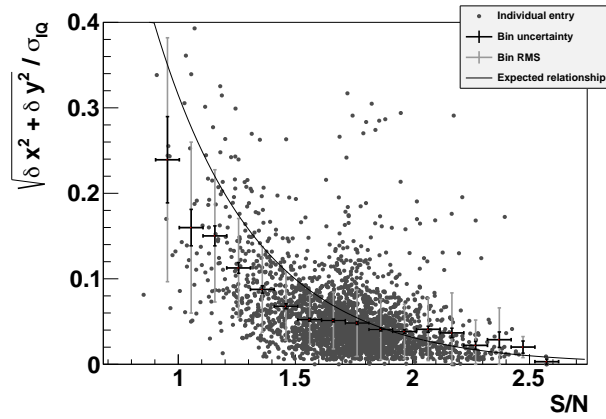


Figure 4.11: We consider the error in the fitted position in units of σ_{IQ} as a function of the S/N ratio. We also plot the expected relation between the two using equation 4.17.

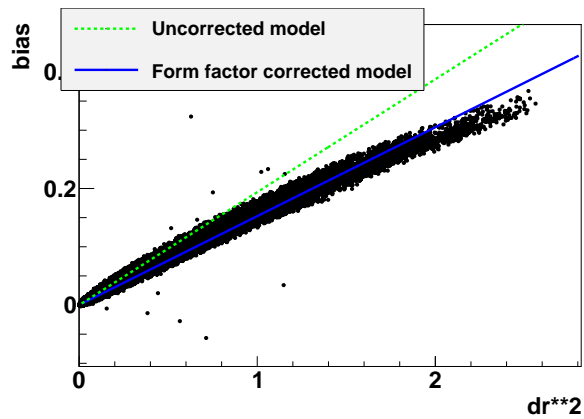


Figure 4.12: To fit the form factor, we fit a slope in the r^2 VS flux bias plane, where r is the error on the position. Each black point represents the computed bias using equation 4.18 for a random position on the image and a random displacement across it.

Chapter 5

Photometric Calibration of the SNLS Supernova Sample

Photometric measurements merely reflect the number of photons received in an image during observation. On its own this is not a measurement of the intrinsic luminosity of the observed object, given that this number also depends on the observing conditions. To obtain a useful quantity, we must calibrate our measurements. Understanding that process and how it was done in the context of SNLS is the goal of this chapter. We begin by presenting the general concepts involved in photometric calibration of supernovae, which consists of comparing the supernova flux to the flux of a known object. Afterwards, we characterize the instrument response model, an important step if we are to properly interpret the calibrated fluxes. Finally, we look at how all this was applied to the SNLS images to compute what are called **zero points**, the principal quantity that determines the flux scale of our measurements.

5.1 Calibrating Supernova Measurements

5.1.1 An Introduction to Photometric Calibration

The flux of a given object is defined as a direct measure of the electron count in a CCD. Therefore, these are completely uncalibrated quantities as they depend on exposure time, atmospheric extinction, and other factors unique to any given image. In order to obtain a calibrated quantity whose value corresponds strictly and solely to the luminosity of the observed object, one must compare flux measurements between the object of interest and an object whose properties have already been understood. This is a classical concept of calibration, as is often used and understood in many other areas of physics. To understand the specifics of our photometric calibration scheme, we begin by defining a few basic concepts.

Recall that, as we have seen in section § 2.3.2, the light received depends on the instrumental response $T(\lambda)$, itself of course also a function of wavelength, as seen in equation 2.3. The calibrated quantity is then obtained by comparing this integral to the same integral for a well defined SED $\phi_S(\lambda)$, referred to as the standard star, as seen in equation 2.4. Recall that we use a logged value of this quantity called a magnitude, as seen in equation 2.5. This allows for a noteworthy reformulation of the calibrated quantity :

$$\begin{aligned}
 m &= -2.5 \log_{10} \left(\frac{\int \phi(\lambda) T(\lambda) \lambda d\lambda}{\int \phi_S(\lambda) T(\lambda) \lambda d\lambda} \right) \\
 &= -2.5 \log_{10} \left(\int \phi(\lambda) T(\lambda) \lambda d\lambda \right) + 2.5 \log_{10} \left(\int \phi_S(\lambda) T(\lambda) \lambda d\lambda \right) \\
 &= -2.5 \log_{10} F + zp
 \end{aligned} \tag{5.1}$$

The zp quantity above is called a zero point, and it sets the relative flux scale of our measurements. The process of calibration therefore comes down to computing this zero point.

Now that we have a definitional understanding of calibration, we can move on to the practical details of how this comparison is carried out. Remember that the zero point of an image is defined as $2.5 \log_{10}(F_S)$ where F_S is the observed flux of the standard *in the same observing conditions*. This poses a problem, because no primary calibration stars are in the science fields. We must therefore compare the flux of our supernovae with those of stars from other images. This presents 2 challenges :

1. The first is that not all nights are photometric nights. Photometric nights are nights on which observing conditions are stable enough that the difference in extinction between 2 separate images can be almost entirely attributable to an airmass difference, which we can then correct for. Only using images on photometric nights would discard about 30% of images (see [observer statistics of MegaPrime observations](#)), an unacceptably large loss of data.
2. The second is that PSF photometry is only guaranteed to preserve flux ratios so long as the PSF model is the same for both objects. That way, PSF modeling errors affect both objects similarly and maintain linearity. To make matters worse, some primary standard stars are too bright to be observed regularly, and require a defocusing of the camera lens so as to not saturate the CCD too quickly (thus significantly increasing the impact of exposure time uncertainty). This makes PSF modeling nearly impossible.

The first issue is only an issue if you want to calibrate supernova fluxes, because their flux varies from image to image. Non variable stars present in the science field, referred to as tertiary stars, can be counted on to always have the same flux. We therefore calibrate the tertiary stars on photometric nights, which then serve as local standards, whose fluxes can then be locally compared with supernova fluxes on any night. The calibrated flux ratio therefore becomes the product of multiple ratios. As noted previously (see section § 4.2.1), because our photometry method's flux estimator is in units of ADUs *in the reference image*, this whole process boils down to computing only one zero point per image series. Continuing on from equation 5.1, it is clear that we can construct an estimator for the zero point using the following average :

$$zp = \langle m_{APER} + 2.5 \log_{10} \hat{f}_{PSF} \rangle_{\text{over all field stars}} \tag{5.2}$$

Where the magnitudes m_{APER} of the tertiary stars have been obtained by calibrating them on photometric nights, and \hat{f}_{PSF} is the flux estimated using PSF photometry. The magnitudes used are delivered by the [Betoule et al. \(2013\)](#) catalog. Recall, however, that calibrating the tertiary stars in this fashion cannot be done using PSF photometry, and we rely instead on aperture photometry. However, the fluxes used while computing the zero point must be obtained using the same photometry method as the supernovae to ensure linearity. This means that the photometry employed to obtain the tertiary star magnitudes is different than the fluxes we then

compare those magnitudes to. Any systematic difference between the 2 methods will lead to a calibration bias.

5.1.2 The SNLS Magnitude System

Here we summarize the work done in [Betoule et al. \(2013\)](#), which defines the magnitude system used in the SNLS5 analysis. It is the result of an effort to intercalibrate both the SNLS and SDSS surveys, and came to fruition thanks to the JLA collaboration.

As we have described previously, the process of photometric calibration consists in comparing measured fluxes to the flux of an object of known magnitude. In practice, this is a multi-tiered process. The tertiary stars are compared to what are called secondary stars, and these are in turn compared the primary stars that set the absolute scale of flux calibration.

In SNLS, the secondary stars used are those of the [Landolt \(1992\)](#) catalogue, and were observed using MegaCam. The Landolt catalogue provides photometric standards, and not spectrophotometric standards. This means that only some of their broadband magnitudes are accurately known, namely in the U, B, V, R, and I bands, which are poorly defined in the Landolt catalogue, and differ significantly from the MegaCam bands. Indeed, when using the Landolt catalogs we rely on color transformations because the filters used to measure those secondaries are never clearly defined. The ensuing color transformations lead to significant uncertainties in the calibration transfer. Because the HST standards are spectrophotometric standards, that is, the flux scale of the entire SED is known, no color transformations are required when transferring the calibration from the standards to the secondaries.

In SDSS, a network of secondary star patches spread throughout the SDSS survey area was constructed using the dedicated **photometric telescope** (PT). The patches are observed using both the PT and the SDSS science field telescope. In turn, the PT is used to observe both these patches and the primary standards used, which are the same HST standards used by SNLS. This last calibration transfer transforms the stars in the PT patches into photometric standards. Here again, color transformations are required because the PT filters are not exactly the same as those of SDSS.

Each calibration transfer and each color transformation further increases the uncertainty on the final zero points. To circumvent many of these limitations, complementary observations were done with MegaCam. First, the SNLS science fields tertiaries were compared to the HST standards. This was done by observing the SNLS science fields and the HST standards on the same photometric nights and applying an air mass correction to both based on the telescope pointing. This allows us to compute reliable flux ratios between the two. This means that the flux calibration transfer from standard star to SNLS tertiary star is done in a single comparison, with no need for color transformations given that both sets of measurements were made using the same camera and filters. Second, the SNLS tertiaries were also compared directly to the SDSS tertiaries. This allows for the two surveys to be directly intercalibrated, as opposed to indirectly through their common point in the calibration chain (the HST standards). This calibration path is represented diagrammatically in figure 5.1. The final uncertainties obtained from this process will be explored in section § 5.3.3. When computing a zero point using the averaging scheme of equation 5.2, it is important that any induced uncertainty remains largely subdominant to the smallest calibration induced zero point uncertainty.

Note that the SED of the $\phi_S(\lambda)$ in equation 5.1 is not that of any of the HST standards. Instead, a power law is used. This is known as the AB magnitude system (see, for example, a description of such a magnitude system for the **Sloan Digital Sky Survey** in [Fukugita et al. \(1996\)](#)). This does not present a problem as the choice of $\phi_S(\lambda)$ merely defines how we interpret

magnitudes during flux calibration transfers. It does not have to be an actually measured star itself. The AB magnitude system is still anchored using observations of standard stars, but because the SED of those stars is fully known their observed fluxes can easily be converted to AB magnitudes.

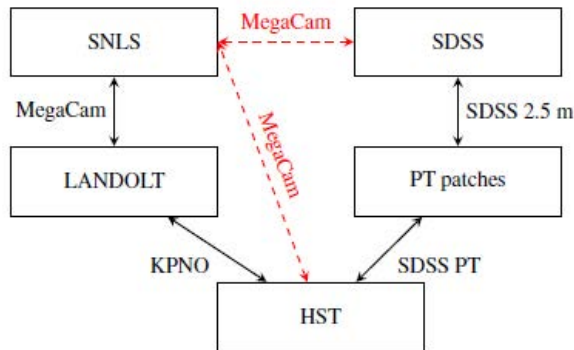


Figure 5.1: The solid black lines represent the old calibration transfer scheme, as described in [Regnault et al. \(2009\)](#). The dotted red lines represent the work done in [Betoule et al. \(2013\)](#). The instrument names indicate that both sets of stars were observed with the said instrument, hence making flux calibration transfer possible.

5.2 Instrument Response Model

As we have seen in section § 2.3, accurate measurements of supernova distances require photometric data from different wavelength ranges. It is for this reason that MegaCam observations are obtained using different filters. In this section we explore the various filters used and the measurements required to understand them.

5.2.1 Transmission Model

We begin by describing the passband model used. Afterwards, we will go over the various measurements required to characterize each component of the passband model.

The filters are not the only medium the supernova light must traverse before reaching MegaCam. At each medium, a certain fraction of the light received is lost, depending on the wavelength. We define the product of all those fractions as the transmission function. Because the filter transmission actually varies throughout the filter, this transmission function is also a function of the position on the focal plane. It is modeled as :

$$T_x^b(\lambda) = T_b^f(\lambda, x)T_c(\lambda)R_m(\lambda)T_a(\lambda)\epsilon_{ccd}(\lambda) \quad (5.3)$$

Where :

$T_t^b(\lambda, x)$ is the total transmission function a distance x away from the center, at wavelength λ , for filter b (where b can be any of g , r , i , and z).

$T_f^b(\lambda, x)$ is the transmission function of the filter b . Note that it assumes a radial symmetry, whose observed deviations are entirely negligible.

$T_c(\lambda)$ is the transmission function of the wide field corrector.

$R_m(\lambda)$ is the primary mirror reflectivity.

$T_a(\lambda)$ is the atmospheric transmission.

$\epsilon_{ccd}(\lambda)$ is the quantum efficiency of the CCD.

Recall that when measuring objects at essentially infinite distance, each point on the focal plane is actually the result of multiple optical paths, each with a particular angle of incidence on the filter. For an incidence angle θ , this shifts the filter transmission by :

$$T_f^b(\lambda) \approx T_f^{b,0} \left(\frac{\lambda}{\sqrt{1 - \sin^2\theta/n^2}} \right) \quad (5.4)$$

Where $T_f^{b,0}$ corresponds to the filter model when refraction is not taken into account. To correct for the effects of refraction, the filter model used is blueshifted using equation 5.4 for θ set to the average incident angle of the CFHT.

Recall that the flat fields are meant to measure variations in the instrument response as a function of position. However, because these are obtained using twilight images, there are some differences between twilight flats and the same measurements for point like objects. This is mainly due to the fact that internal reflections produce a characteristic pattern of stray light during twilight observations. These reflections are negligible for the science images, as only certain points in the sky are illuminated, as opposed to all optical paths being flooded by twilight light. Indeed, as we have already seen in figure 3.8, internal reflections play a significant role in the light's trajectory. Because these differences are expected to be stable in time, we can construct a single correction that will transform twilight flats into flats acceptable for the photometry of point sources. This correction is referred to as the grid correction. The results of these corrections can be seen in figure 5.2.

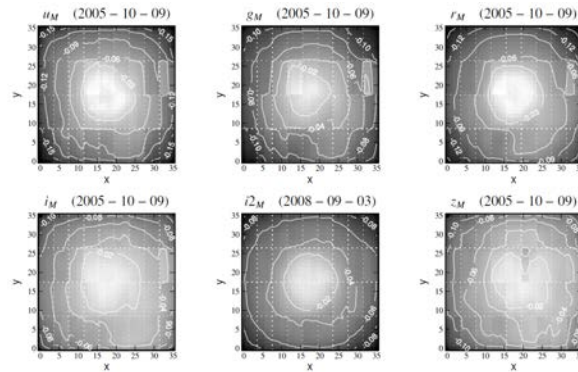


Figure 5.2: Relative corrections to the twilight flat fields due to grid corrections.

In figure 5.3, we see a summary of the steps and measurements required before arriving at a complete characterization of the instrument's transmission function, as required for precision photometry. In the next section, we will explore these measurements.

5.2.2 Filter Measurements

The filter manufacturers provide measurements of the filter transmission function at various positions throughout the focal plane. Starting at the center of the focal plane, measurements are

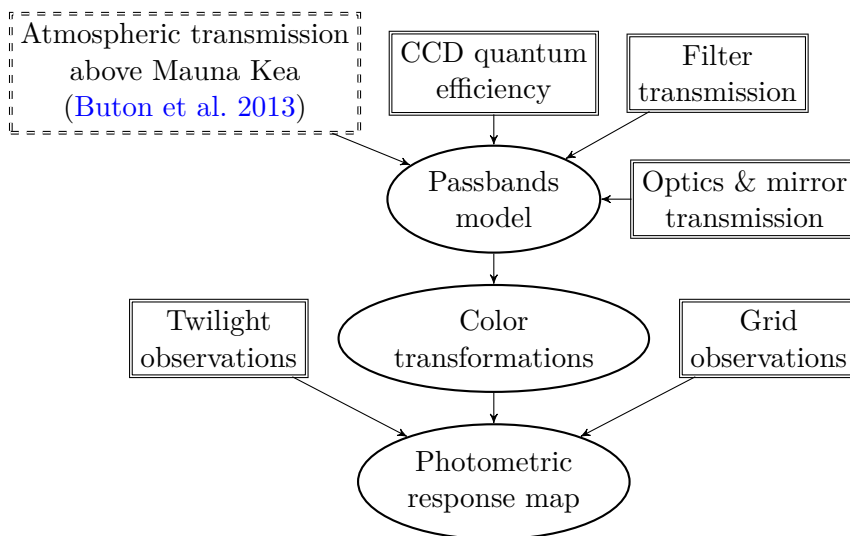


Figure 5.3: Overview of the MegaPrime photometric response analysis. Boxes describe the various data sets involved in the construction of the model (dashed for external data). Ellipses represent the main steps of the analysis. Taken from [Betoule et al. \(2013\)](#). Using the lessons learned from surveys such as SNLS and SDSS, newer surveys such as DES and LSST will regularly measure the combined impact of the optics, the filters, and the CCDs rather than dealing with them separately.

also provided at 23, 47, 70, 93, 117, 140, 163, 186, and 210 mm from the center. A continuous model for $T_f^{b,0}(\lambda, x)$ is obtained by linearly interpolating the observed values.

The filter transmissions were also measured at CFHT at varying angles, between 0° and 8° . These measurements both validate equation 5.4 and allow us to estimate the value of n , the refractive index of each filter.

The grid corrections are obtained using dithered¹ observations of dense stellar fields, by considering the change in observed brightness from one dithering to the next, and comparing them to the corresponding flat. However, because the shape of the transmission function varies across the focal plane, dithering induces a color dependence in the instrumental response to a given star unrelated to the grid corrections. Thus, the magnitude difference observed when dithering are a combination of 2 effects, that we model as :

$$\delta m(x, c) = \delta z p(x) + \delta k(x) \times c \quad (5.5)$$

Where $\delta m(x, c)$ corresponds to the change in magnitude due to the dithering, $\delta k(x) \times c$ corresponds to the color dependent shift induced by changes in the transmission function, and $\delta z p(x)$ corresponds to the grid corrections. In other words, we need to subtract the color transformations from the magnitude shifts in order to obtain the grid corrections that we are after. To understand how these color transformations are obtained, we recall the definition of magnitudes :

$$m = -2.5 \log_{10} \left(\frac{\int \phi(\lambda) T_x^b(\lambda) \lambda d\lambda}{\int \phi_S(\lambda) T_x^b(\lambda) \lambda d\lambda} \right) \quad (5.6)$$

¹Dithering corresponds to slight differences in telescope pointing from one image to the next.

Where $\phi(\lambda)$ corresponds to the SED of the observed object, $\phi_S(\lambda)$ corresponds to the SED of the standard calibration star, and $T_x^b(\lambda)$ the transmission of the filter at distance x from the focal center. By using a spectroscopic library of stars (Gunn & Stryker 1983) that contain a full description of the SED for typical stars, one can compute the corresponding m at both $x = 0$ and at an off center x . We plot the difference between the two as a function of color, as seen in figure 5.4. By fitting a slope to these values, the value of $\delta k(x)$ of equation 5.5 can be determined for any given x . This is done for a number of x , and interpolated to obtain a continuous model.

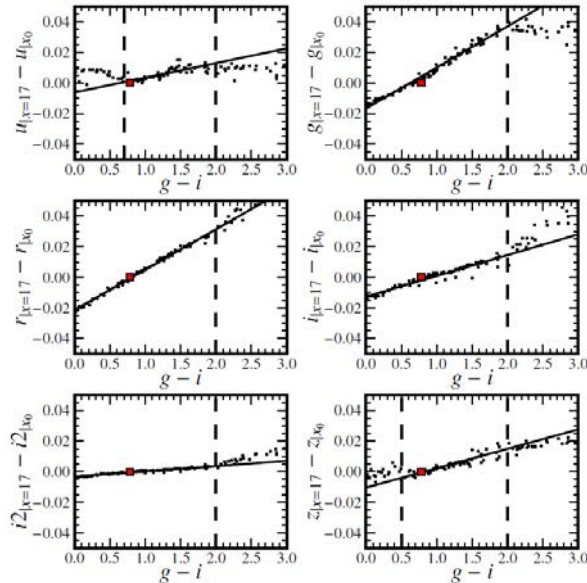


Figure 5.4: Filter induced color dependence of magnitudes at 17cm from focal center in u, g, r, i, i2, and z bands.

Once the color transformations are determined, it becomes possible to isolate the grid correction component of equation 5.5. Once these grid corrections are obtained, rather than directly applying them to the images, they are applied to the photometric measurements discussed in the previous chapter.

5.3 Zero Point computation

Recall that the magnitudes and fluxes involved in equation 5.2 come from aperture and PSF photometry respectively. In order to minimize the systematics induced by this averaging, it is important to control for any differences between the 2 photometry methods. We find that there are two significant difference between the two methods :

- First, aperture photometry makes no attempt at accounting for sky subtraction residuals. Indeed, this is why sky subtraction is required the first place, as aperture photometry does not take sky levels into account at all. In other words, the obtained flux will be artificially modified by the total flux contribution of sky residuals in the aperture. On the other hand, PSF photometry actually fits the remaining sky level integrated by aperture photometry (this is the s_i term of equation 4.4). Imperfections of sky subtraction lead to

a bias, particularly significant at low fluxes where the sky level is more significant relative to the star's flux.

- Secondly, PSF photometry does not take into account the chromatic dependence of the PSF. The model assumes that the PSF is the same for all stars, regardless of color, which obviously leads to a color dependency in the produced PSF fluxes. Because aperture photometry does not depend much on the shape of the PSF, it is not affected by this. This also leads to a significant difference.

Here we will explore the solutions employed to get around these issues.

5.3.1 Sky Pollution Bias

The sky level subtracted from the images is obtained using the average of the image pixels computed over all pixels, except for masks placed over all detected objects, as described in section § 4.1.1. Despite these masks, residual contamination from the tails of the flux distribution of bright objects affect the remainder of the image. We note that a prominent criteria in the selection of tertiary calibration stars is their level of isolation, and they will therefore be systematically less contaminated than the average pixels over which the sky level was computed. This is why the residual sky level *at the position of tertiary calibration stars* does not average out to 0 when averaged over all images for any given star. Note that such an effect manifests itself as a flux dependent bias because the same residual sky level will affect the ratio of \hat{f}_{PSF} to \hat{f}_{APER} more significantly for lower fluxes. This is seen clearly in figure 5.6a. It is possible to compute the expected effect by comparing the PSF tail pollutions expected at the average distance from the nearest bright objects for tertiary stars to the average PSF tails pollutions over the pixels used to compute the sky level (see fig. 17 of [Betoule et al. \(2013\)](#)). These can reach up to one percent of the total flux for the dimmest tertiary stars (of magnitude 21). The calibration catalogs given employ such a correction.

Such a correction provides only a crudely averaged estimate of the effect. Indeed, this only produces one single correction to be applied to all stars equally. During the calibration process described here, we undo this correction using the figures provided in section § 4.3.4 of [Betoule et al. \(2013\)](#) and implement our own. By using the fitted sky level of PSF photometry, we can instead provide one correction per star. However, such a correction only makes sense if we can reasonably believe that the fitted sky level actually corresponds to the left-over sky level. We expect for the fit to make up for errors in the PSF model by artificially altering the fitted sky level with a fraction of star's actual flux, while the actual sky level obviously should not scale with the star flux. To allow for a chromatic component to PSF modeling errors, as we will discuss in section § 5.3.2, we model the fitted sky level as:

$$\hat{s} = [a + b \times (g - i)] \hat{f}_{PSF} + \hat{s}' \quad (5.7)$$

- \hat{s} : is the average fitted sky level
- $g \& i$: are the g and i magnitudes respectively
- \hat{s}' : is the new estimate of the average sky level
- $a \& b$: are fitted parameters

The a term is meant to accommodate both that colors are arbitrarily defined, and that achromatic PSF errors cause transfers between object flux and sky level. By definition, \hat{s}' is expected to be the true sky level and hence not to scale with \hat{f}_{PSF} . So, \hat{s}' becomes negligible at the high-flux end of our stars, and we fit a & b in this regime, thus rewriting model 5.7 as:

$$\frac{\hat{s}}{\hat{f}_{PSF}} \approx a + b \times (g - i) \quad (5.8)$$

The fitted relation is illustrated in figure 5.5 and the a & b values for each band are displayed in table 5.1.

Table 5.1: Parameters relating fitted sky level and flux as a function of color for bright stars (Eq. 5.8).

Band	$a \times 10^6$	$b \times 10^6$
g	14 ± 0.7	-13 ± 0.5
r	8.4 ± 0.3	-5.4 ± 0.2
i	7.7 ± 0.5	-4.8 ± 0.2
$i2$	10 ± 0.5	-6 ± 0.2
z	-1.6 ± 0.1	2.5 ± 0.1

Using these new \hat{s}' sky values, we can correct the aperture fluxes from [Betoule et al. \(2013\)](#), using their standard aperture area:

$$N_{APER}^{effective} = \pi [7.5 \times \langle \sigma_{IQ} \rangle]^2 \quad (5.9)$$

where the effective σ_{IQ} used is also given by the [Betoule et al. \(2013\)](#) downloadable catalogs.

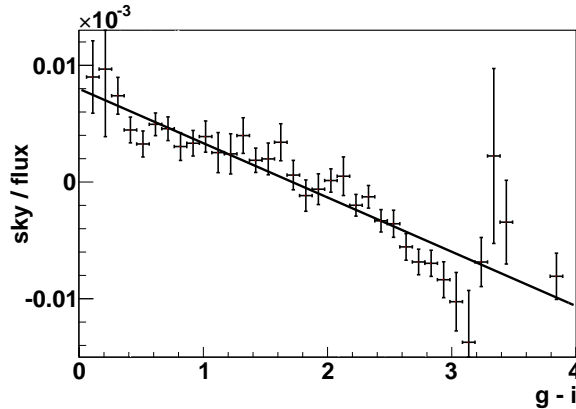


Figure 5.5: Ratio of the fitted sky level to the flux of the star as a function of color, for high flux stars only in i band. For such stars we assume that the fitted sky level is predominantly a fraction of the flux incorrectly fitted as the sky level. We see that the fraction of flux that goes into our sky level estimator evolves linearly with color.

In theory, we should now remove this flux from the aperture magnitudes. However, since the sky values are fitted in units of the PSF fluxes, we instead add this correction to PSF fluxes. These two methods are perfectly equivalent. The new zero point averaging scheme therefore becomes :

$$zp = \left\langle m_{APER} + 2.5 \log_{10} \left(\hat{f}_{PSF} + N_{APER}^{effective} \hat{s}' \right) \right\rangle \quad (5.10)$$

where $N_{APER}^{effective}$ is defined in Eq. 5.9. Using these corrections, we are able to eliminate the magnitude bias of the zero point residuals, as shown in figure 5.6b: the zero point residuals become flat over the entire range of used magnitudes. This is good evidence that we have, on the one hand, properly understood the origin of this bias, and, on the other hand, properly understood the fitted sky level.

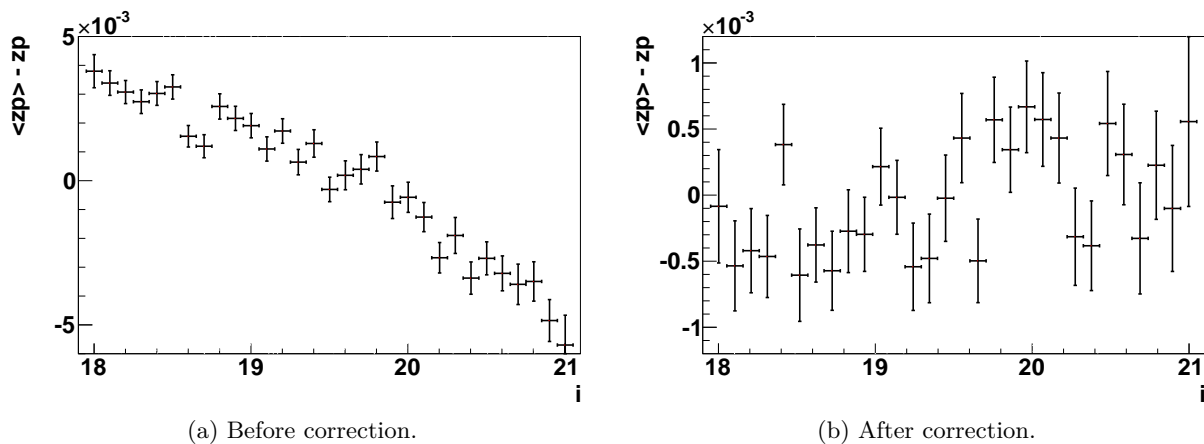


Figure 5.6: Plot of zero point residual vs magnitude in i band, before and after correcting for aperture sky pollutions.

5.3.2 Chromatic PSF Bias

In figure 5.7a, we display the values of the zero-point residuals as a function of star color after application of the sky level correction just discussed. A clear chromatic difference is observed. We interpret this trend as resulting from the chromaticity of the PSF which is not accounted for in the PSF model: blue and red stars are measured using the same PSF model, although blue stars are fatter than red stars (except in z band where the effect is apparently reversed). Such an effect is expected because IQ tends to improve towards red wavelengths. We call α the slope of the observed relation. Its value is significant enough that the effect must be corrected, in particular in g band. We set out to construct a natural magnitude system for PSF fluxes that circumvents this effect. In other words, we want to be able to convert PSF fluxes to magnitudes despite having no knowledge of the object's color, which will be the case for supernova measurements. Explicitly, we want to be able to write :

$$m_{PSF} = -2.5 \log_{10}(\hat{f}_{PSF}) + zp \quad (5.11)$$

It is clear from this requirement that PSF magnitudes will differ from aperture magnitudes via a color term :

$$m_{PSF} = m_{APER} + \alpha(c - c_{AB}) + \epsilon \quad (5.12)$$

where, for the time being, ϵ is an arbitrary offset that we have not yet constrained. Note that in the AB magnitude system, c_{AB} is 0 by definition. We write it nonetheless to emphasize that the relevant color term is the color difference *relative to* the standard used. Recall now the definition of magnitude for a given spectral energy density $\phi(\lambda)$, given in equation 2.5. For the aperture

magnitudes given in the calibration catalog it is :

$$m_{APER} = -2.5 \log_{10} \left(\frac{\int \phi(\lambda) T(\lambda) \lambda d\lambda}{\int \phi_{AB}(\lambda) T(\lambda) \lambda d\lambda} \right) \quad (5.13)$$

The transmission function $T(\lambda)$ used is that derived in [Betoule et al. \(2013\)](#). We choose to construct our own natural magnitude system for PSF fluxes using an additional effective filter $C(\lambda)$. We expect this to be an accurate model because ignoring the PSF dependence on wavelength favours red wavelengths over blue wavelengths (except for z band where the effect goes the other way). This is indeed equivalent to an additional filter. In this new magnitude system, for a given spectral energy density $\phi(\lambda)$, the PSF magnitude is given by :

$$m_{PSF} = -2.5 \log_{10} \left(\frac{\int \phi(\lambda) T(\lambda) C(\lambda) \lambda d\lambda}{\int \phi_{AB}(\lambda) T(\lambda) C(\lambda) \lambda d\lambda} \right) \quad (5.14)$$

This effective filter is chosen in such a way that it emulates the chromatic discrepancy between PSF and aperture magnitudes described in equation 5.12. We chose to parametrize this extra-filter as a linear function of wavelength. In effect, we require that for a given spectrophotometric library of stars (here we used the [Pickles \(1998\)](#) library), the difference between PSF and aperture magnitudes described in equations 5.13 and 5.14 has the same chromatic dependency as that described in equation 5.12. In figure 5.7b, we see that the constructed linear filter can indeed produce the required chromatic dependency. It is clear from the definitions of m_{PSF} and m_{APER} that the two yield the same value for ϕ_{AB} . It is also clear from figure 5.7b that the discrepancy between the two magnitude systems is not 0 for a typical star whose color is the same as that of AB, because of the peculiarity of the AB spectral energy density. This constrains the free offset term ϵ in equation 5.12 in that it must account for this. In other words, to convert the magnitude of a star from the aperture system to the PSF one, in addition to a color correction term $\alpha(c - c_{AB})$, we must also apply an offset ϵ which corresponds to the magnitude discrepancy between the 2 systems at the color of AB. The values obtained for α and ϵ are presented in table 5.2, with a description of the constructed linear filter used to obtain them.

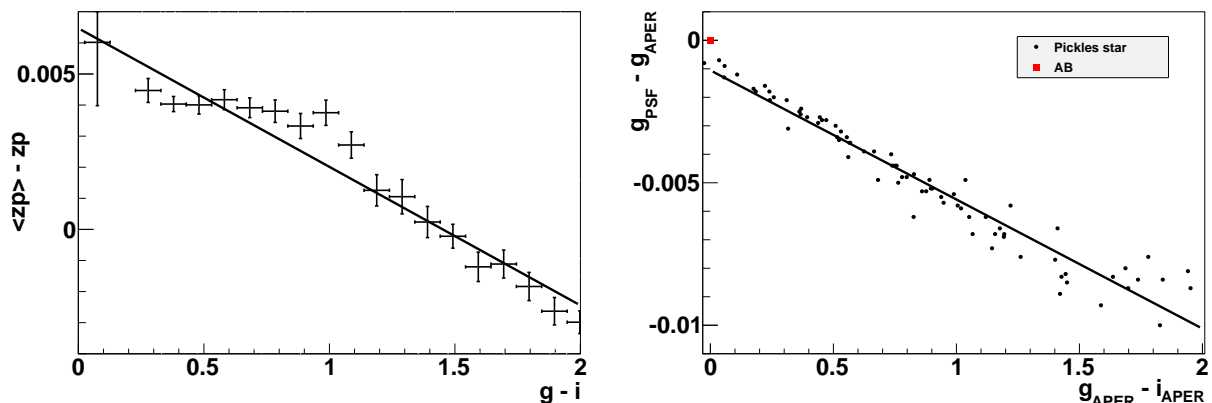
Finally, this means that in fitting a zero point by comparing PSF fluxes to aperture magnitudes we must take care to add a color correction term and equation 5.10 becomes :

$$zp = \left\langle m_{APER} + 2.5 \log_{10} \left(\hat{f}_{PSF} + \hat{s}' \right) + \alpha(c - c_{AB}) + \epsilon \right\rangle \quad (5.15)$$

Table 5.2: Color terms and offsets between PSF and aperture natural magnitude systems in each band. α and ϵ are defined by Eq. 5.12. The λ_0 parameter describes the corresponding additional effective filter of equation 5.14 such that $C(\lambda) = \lambda + \lambda_0$.

Band	$\alpha \times 10^3$	$\epsilon \times 10^3$	λ_0 (Å)
g	-4.7 ± 0.2	-1.1 ± 0.13	19227
r	-0.7 ± 0.2	0.051 ± 0.013	57500
i	-2.4 ± 0.2	0.82 ± 0.12	8206
i2	-3.1 ± 0.2	0.98 ± 0.14	7389
z	0.7 ± 0.2	-0.25 ± 0.03	-48409

Switching spectroscopic libraries changes the value of ϵ by about 10^{-4} magnitude or less depending on the band. There is therefore no significant systematic error associated with this magnitude system transformation.



(a) Zero point residuals as a function of color for real data in g band, for a zero point fit using equation 5.10.

(b) Difference between synthetic aperture and PSF magnitudes as a function of the star (aperture) color, for stars from the Pickles (1998) spectroscopic library. The effective PSF bandpass has been adjusted for the slope to reproduce that of figure 5.7a.

Figure 5.7: Comparison of data with Pickles (1998) spectroscopic library in order to fit an appropriate effective filter, in g band.

Finally, we consider the implications that PSF chromaticity can, in part, be due to atmospheric effects, and that the resulting color term might then vary with IQ. We have fitted the slope of figure 5.7a separately for IQs below and above the median IQ, and have found extremely compatible values. We hence conclude that a single color term can effectively describe the chromatic effects independently of IQ.

Now that we have a trustable averaging scheme for computing zero points, we can finally proceed with an unbiased calibration of the SNLS images. In appendix B we outline the various cuts used and their impact on the final zero point value.

5.3.3 Results of Calibration uncertainty

It is important that none of the uncertainties that arise as a result of zero point fitting become significant relative to the calibration uncertainties themselves, namely those that arise in the calibration process described in section § 5.1.2. These calibration uncertainties are summarized in table 5.3.

Table 5.3: Final calibration uncertainty of the SNLS survey, as obtained by the work of Betoule et al. (2013).

Band	u	g	r	i	i2	z
σ_{zp}	0.0145	0.0035	0.0051	0.0042	0.0043	0.0069

In table 5.4 we see a summary of the results of zero point fitting, focusing on the statistical uncertainties that arise due to the limited number of stars in any given image.

Finally, in table 5.5 we summarize all the systematic uncertainties due to PSF photometry that we have discussed so far (sections § 4.2.3, § 4.3.5.2, § 5.3.1, and § 5.3.2).

Note that both the statistical uncertainties of zero point fitting and the systematic uncertainties of PSF photometry are subdominant relative to the calibration uncertainties of table

band	field	σ_{zp}			RMS across CCDs	RMS per CCD			# stars		
		mean	min	max		mean	min	max	mean	min	max
g	D1	1.1e-03	6.8e-04	1.8e-03	6.9e-03	7.4e-03	4.1e-03	1.0e-02	50	31	67
	D2	9.2e-04	7.1e-04	1.4e-03	6.3e-03	7.4e-03	6.1e-03	9.3e-03	66	46	85
	D3	1.1e-03	7.5e-04	1.5e-03	7.7e-03	7.3e-03	4.9e-03	9.7e-03	49	36	61
	D4	7.4e-04	5.7e-04	9.8e-04	7.0e-03	7.0e-03	5.4e-03	8.5e-03	89	66	106
r	D1	1.1e-03	8.3e-04	1.5e-03	7.7e-03	8.1e-03	6.3e-03	9.9e-03	61	41	89
	D2	9.2e-04	7.0e-04	1.2e-03	7.6e-03	8.4e-03	6.8e-03	1.0e-02	85	60	116
	D3	9.0e-04	6.2e-04	1.3e-03	9.6e-03	7.1e-03	4.8e-03	9.6e-03	64	49	81
	D4	7.1e-04	5.1e-04	8.9e-04	8.9e-03	7.5e-03	5.4e-03	9.4e-03	113	75	133
i	D1	1.0e-03	7.3e-04	1.6e-03	6.9e-03	7.8e-03	5.4e-03	1.1e-02	59	36	79
	D2	8.4e-04	6.0e-04	1.1e-03	4.4e-03	7.8e-03	5.6e-03	1.0e-02	88	68	119
	D3	9.4e-04	6.0e-04	1.4e-03	5.7e-03	7.3e-03	5.3e-03	9.9e-03	64	47	91
	D4	6.8e-04	5.1e-04	8.5e-04	5.4e-03	7.2e-03	5.5e-03	8.6e-03	116	71	139
y	D1	1.1e-03	8.0e-04	1.5e-03	5.6e-03	7.9e-03	5.8e-03	1.0e-02	49	38	58
	D2	9.1e-04	7.3e-04	1.3e-03	6.3e-03	8.3e-03	6.6e-03	1.1e-02	85	64	117
	D3	8.9e-04	5.7e-04	1.2e-03	7.0e-03	6.9e-03	4.4e-03	9.0e-03	62	44	84
	D4	7.9e-04	6.4e-04	9.5e-04	2.8e-03	8.3e-03	6.6e-03	9.8e-03	111	66	130
z	D1	1.0e-03	6.6e-04	1.3e-03	8.6e-03	7.3e-03	4.6e-03	9.3e-03	53	39	72
	D2	9.4e-04	7.0e-04	1.3e-03	1.3e-02	8.6e-03	6.7e-03	1.0e-02	86	61	114
	D3	1.0e-03	5.8e-04	1.5e-03	5.5e-03	7.9e-03	4.8e-03	9.9e-03	61	41	82
	D4	7.3e-04	5.4e-04	9.5e-04	9.1e-03	7.6e-03	5.7e-03	9.0e-03	110	69	134
g	ALL	9.5e-04	5.7e-04	1.8e-03	×	7.3e-03	4.1e-03	1.0e-02	63	31	106
r	ALL	9.0e-04	5.1e-04	1.5e-03	×	7.8e-03	4.8e-03	1.0e-02	81	41	133
i	ALL	8.7e-04	5.1e-04	1.6e-03	×	7.5e-03	5.3e-03	1.1e-02	82	36	139
y	ALL	9.3e-04	5.7e-04	1.5e-03	×	7.8e-03	4.4e-03	1.1e-02	77	38	130
z	ALL	9.3e-04	5.4e-04	1.5e-03	×	7.8e-03	4.6e-03	1.0e-02	78	39	134
ALL	D1	1.1e-03	6.6e-04	1.8e-03	×	7.7e-03	4.1e-03	1.1e-02	54	31	89
ALL	D2	9.0e-04	6.0e-04	1.4e-03	×	8.1e-03	5.6e-03	1.1e-02	82	46	119
ALL	D3	9.6e-04	5.7e-04	1.5e-03	×	7.3e-03	4.4e-03	9.9e-03	60	36	91
ALL	D4	7.3e-04	5.1e-04	9.8e-04	×	7.5e-03	5.4e-03	9.8e-03	108	66	139

Table 5.4: Summary table of statistical uncertainties due to zero point fitting. The mean, min, and max sub-columns correspond to the average, minimal, and maximal values of the quantity in question across all 36 CCDs.

Effect	induced bias	determination	section
linearity	2.72×10^{-4}	simulation	§ 4.3.5.2
PSF color	1.30×10^{-4}	artificial filter	§ 5.3.2
sky residuals	$< 1 \times 10^{-4}$	zero point residuals	§ 5.3.1
refraction	3.00×10^{-4}	comparison to fit	§ 4.2.3

Table 5.5: Summary of systematic uncertainties due to PSF photometry. Note that if the effect is filter dependent, the table shows the maximum uncertainty.

[5.3](#). Thus, the extremely valuable recalibration work of [Betoule et al. \(2013\)](#) is exploited to its fullest potential, and there is no significant loss of photometric accuracy when applying the recalibration to the SNLS data.

Chapter 6

Cosmology Analysis

We finally have all the tools at our disposal to start doing cosmology. In this chapter we present the final steps of the cosmology analysis. Note that the analysis presented here is still preliminary, and some improvements are still planned, in particular for the SALT2 model training. We begin by looking at the supernova sample used for the analysis. We then look at the various corrections and systematics associated with constructing a Hubble diagram. Finally, we present the results of this analysis. The analysis method presented here largely follows that of [Betoule et al. \(2014\)](#), though it has been updated with new available data where this is available.

6.1 Supernova Sample Selection

We split the supernova sample used in constructing the Hubble diagram into 4 categories. At the highest end redshifts, a few supernovae are provided by the **Hubble Space Telescope** (HST). Dominating the high redshift range are our own SNLS supernovae. The intermediate range is dominated by the SDSS supernovae. The low redshift supernovae come from a variety of surveys, but are usually treated similarly in the analysis that follows. So far, in addition to SNLS data, we have included data from the following surveys :

Center for Astrophysics survey (CfA) The CfA lightcurves are described in [Jha et al. \(2006\)](#) and [Matheson et al. \(2008\)](#). Their spectra are described in [Blondin et al. \(2012\)](#).

Carnegie Supernova Project (CSP) The CSP lightcurves are described in [Stritzinger et al. \(2011\)](#). Their spectra are described in [Folatelli et al. \(2013\)](#).

Sloan Digital Sky Survey (SDSS) The complete data release of both SDSS supernova lightcurves and spectra are described in [Sako et al. \(2014\)](#). The photometry of the SNIa are described in [Holtzman et al. \(2008\)](#).

Hubble Space Telescope (HST) Hubble Space Telescope spectra are taken from [Riess et al. \(2007\)](#) and [Suzuki et al. \(2012\)](#).

Various low-z SNIa An assortment of other low redshift supernovae are also included, whose light curves are taken from [Altavilla et al. \(2004\)](#), [Hamuy et al. \(1996\)](#), and [Riess et al. \(1999\)](#).

6.1.1 SALT2 Training Sample

To be included in the training sample, supernovae must satisfy certain conditions. Prior to the latest iteration of the training, the supernovae are fit with the last version of the SALT2 model. We therefore have an estimate of the supernova parameters prior to the training. We can then create cuts using those parameters :

$$\left. \begin{array}{l} -3 < x_1 < 3 \\ -0.3 < c < 0.3 \end{array} \right\} \quad (6.1a)$$

$$E(B - V) < 0.15 \quad (6.1b)$$

$$\left. \begin{array}{l} \sigma_{\text{day max}} < 0.5 \\ \sigma_{x_1} < 0.5 \end{array} \right\} \quad (6.1c)$$

$$\#\text{rise time points} > 0 \quad (6.1d)$$

$$\chi^2 / \#\text{d.o.f} < 2 \quad (6.1e)$$

Restriction 6.1a makes sure we exclude supernovae whose parameters take values that lie outside the bulk of the distribution, as seen in figure 6.12. This ensures that we only fit the model where sufficient data is present. The model is then only trusted within this parameter region, and is considered to be ill defined outside of it. In addition, as we have seen in section § 2.1.3, SNIa that rise very fast or very slowly are thought to be peculiar SNIa. Also, highly reddened supernovae are thought to lie behind dust clouds in their own host galaxies. This dust reddening is separate from the intrinsic differences we are trying to model, and not taken into account by corrections for our own galactic dust, and so we exclude extremely reddened SNIa.

Restriction 6.1b is here to limit the impact of dust uncertainties. As we will see in section 6.3.4, there is some debate as to the reliability of the available Milky Way dust maps. To this end, we completely exclude highly affected supernovae.

The restrictions of 6.1c are a good proxy for excluding poorly sampled supernovae. We also require that at least one light curve point lie in the region between 10 and 1 days before the point of maximum luminosity in rest-frame B-band. This is to ensure that the maximum date fit is indeed reliable. This excludes a significant number of low redshift supernovae. The strategy for low redshift SN does not follow our own rolling search strategy, as such a strategy is nearly impossible for the large areas covered by low redshift searches. Rather, these supernovae are followed up on after a detection has been signaled, usually from other experiments. For this reason, there are few early lightcurve points for their supernovae. We also apply a quality cut based on the χ^2 of the fit.

In addition, because the Malmquist bias is thought to be significant for the SDSS supernovae, we limit inclusion from this survey to those below a redshift of 0.25, where Malmquist bias begins to take effect. Changing this limit by 0.05 has a negligible impact on the final training sample, so we do not worry further about determining the optimal redshift at which the cut should be applied. The total number of light curves and spectra that enter into the training are shown in table 6.1.

6.1.2 For Cosmology

The supernovae that are used for training the SALT2 model are a subset of those used in the cosmology sample. In other words, the inclusion criteria are loosened for the cosmology sample. Note, however, that some criteria are not loosened.

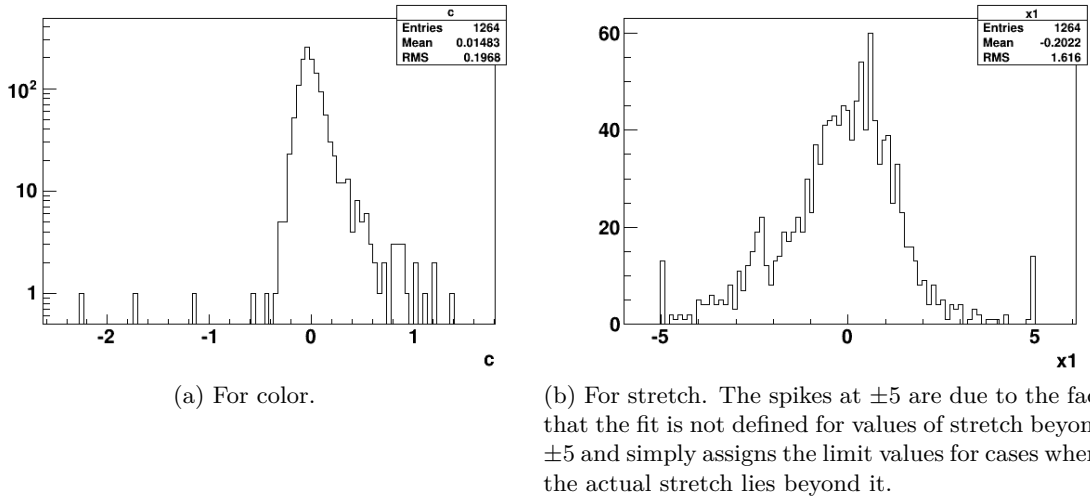


Figure 6.1: Distribution of the full supernova sample (before cuts).

Table 6.1

survey	# LC	# spectra
CfA	76	842
CSP	20	641
SDSS	217	253
SNLS	243	131

The color and stretch requirements remain the same. This ensures that we do not try to extract parameters from a supernova that lies outside the range of model validity. The extinction requirement also remains the same, again to limit the impact of the high uncertainties associated with dust maps. On the other hand, the selections associated with sampling become less stringent. This is because the uncertainty associated with low sampling can be properly propagated to the uncertainty on the light curve parameters. These now become :

$$\begin{aligned}\sigma_{\text{day max}} &< 2 \\ \sigma_{x_1} &< 1\end{aligned}$$

Also, we completely remove the constraint on the number of premax points available. In addition, all light curves that enter the Hubble diagram have been visually inspected. This resulted in the exclusion of a number of SDSS supernova :

- 17 SDSS supernovae were excluded for having poor fit probabilities (under 1%).
- 2 SDSS supernovae were excluded for having been identified as peculiar SNIa by other works (Foley et al. (2013), Stritzinger et al. (2011)).
- 2 SDSS supernovae were excluded due to their odd time sampling, which led to multiple possible dates of maximum.

Finally, after a preliminary fit of the Hubble diagram, we excluded 3 sigma outliers on the Hubble diagram. This excluded four SDSS supernovae and four low redshift supernova. The resulting contributions of each survey are summarized in table 6.2.

Table 6.2: Contributions of each survey to the Hubble Diagram after cuts, including average redshift and residual of each survey after a fit to a Λ CDM model (see section § 6.5.1).

survey	# SN	redshift	residual	RMS
ALL	960	0.34	0.03	0.19
Calan Tololo	16	0.043	0.01	0.17
lowz	10	0.029	0.0041	0.18
CSP	30	0.035	0.071	0.19
CfAI	7	0.028	-0.085	0.19
CfAII	14	0.023	-0.0043	0.22
CfAIII	89	0.028	0.12	0.22
CfAIV	46	0.026	0.15	0.23
SDSS	351	0.21	0.021	0.16
SNLS5	389	0.62	0.0026	0.19
HST	8	1	0.12	0.26

6.1.3 Flux Convention

The final analysis takes place in the SNLS magnitude system. The light curves are written in units of flux, with a corresponding zero point. The CSP and CfA lightcurves are provided in units of magnitude. We convert these to flux by choosing an arbitrary zero point using :

$$F = 10^{0.4 \times (zp - m)} \quad (6.2)$$

Where m is the given magnitude and F is the corresponding flux for a chosen zero point zp . The SDSS lightcurves are also given in magnitudes, but these are asinh magnitudes, which require special treatment. These magnitudes are defined such that :

$$m = \frac{-2.5}{\ln(10)} \times \left[\operatorname{asinh} \frac{F/F_0}{2b} + \ln(b) \right] \quad (6.3)$$

Where F_0 corresponds to the flux of an object of magnitude zero, and b is a dimensionless value which varies by band, which roughly corresponds to the ratio of the noise of the sky in a PSF aperture in $1''$ seeing relative to F_0 . The objective of such a magnitude definition is to circumvent issues relating to negative fluxes. Regardless, these magnitudes must be transformed into fluxes that can be interpreted using equation 5.1. This is done using :

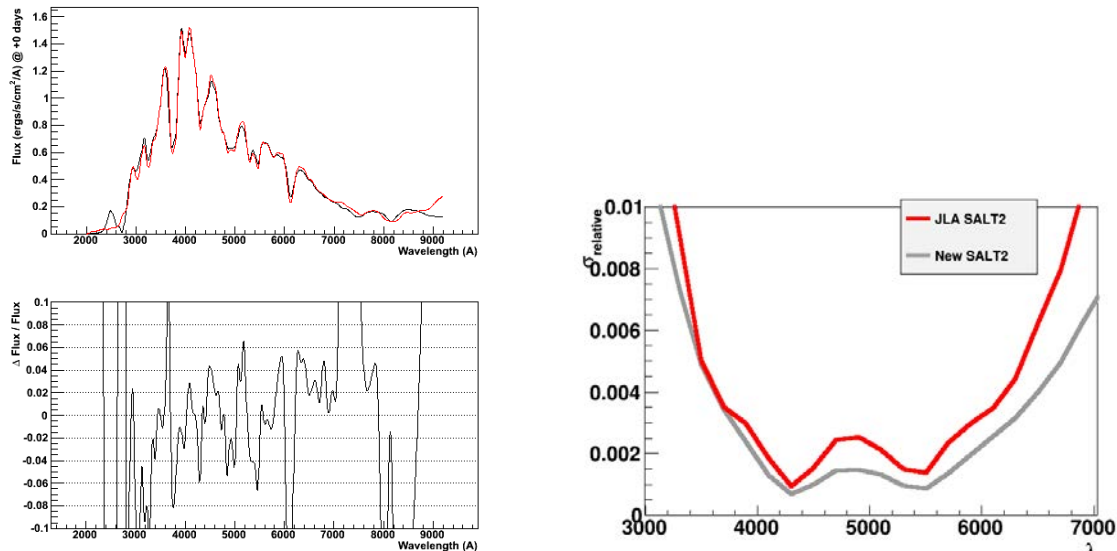
$$F = 2bF_0 \times \sinh(-0.4 \times m \times \ln(10) - \ln(b)) \quad (6.4)$$

6.2 Lightcurve Parameter Extraction

6.2.1 Results of the SALT2 Model

Using the sample described above and the method described in § 2.3, we train the SALT2 model. We use **lambda gradient** regularization for the m_B template, and **full dyadic** regularization for the x_1 template. In figure 6.2a, we compare this new model with that obtained

during the JLA analysis. Notice that while the 2 models closely resemble each other for the bulk of the wavelength range, some significant differences appear near the edges of the model. Note, however, that this area of the model is very poorly constrained, and this is reflected in the model uncertainty shown in figure 6.2b. Hence, these differences are not actually significant when extracting light curve parameters. Note that, unlike for the JLA sample, the SNLS5 spectra have not yet been visually inspected. This work is still in progress.



(a) In red we see the JLA result of the training for the zeroth component of the SALT2 model ($M_0(p, \lambda)$ of equation 2.6). The SNLS5 model is in black. On the bottom we see the relative difference between the two. (b) In red we see the JLA uncertainty for the zeroth component. The SNLS5 uncertainty is in black.

Figure 6.2

The *statistical* uncertainty model produced induces correlations between the parameters of different supernovae. This is because a shift in the model would shift the values of all supernovae parameters. Propagating these uncertainties to the supernovae parameters leads to correlations between them. We call the resulting covariance matrix C_{model} .

6.2.2 Lightcurve Fitting

Now that the model is computed, we can extract the parameters of each individual supernova. The minimization is done using CERN's minuit method. The fit produces an estimator for the date of maximum light, color, stretch, and rest frame blue band magnitude at maximum. In figure 6.3, we look at the evolution of the average values of stretch and color as a function of the redshift. Fitting a slope to both, we find $c = (0.0043 \pm 0.0015) - (0.050 \pm 0.0047) \times z$ and $x_1 = (-0.26 \pm 0.0083) + (0.70 \pm 0.030) \times z$. In both cases we find non-negligible evolution of the average value, though it is far more significant in the case of x_1 . This evolution is, in part, due to the Malmquist bias preferentially selecting higher values of x_1 and lower values of c . The obtained distributions are compatible with predictions from simulations (see Astier et al. (2006) and Kessler et al. (2013)). In addition, there is a significant jump in the values of x_1 between the low- z supernovae and the SDSS ones. This is due to a change in galaxy populations between the

two surveys as a result of different survey strategies. While the SDSS was a rolling search similar to SNLS, low- z surveys periodically revisited specific galaxies, which tended to be particularly massive ones, which in turn tend to have lower values of x_1 .

In addition to producing uncertainties on these estimators, the fit also gives us the covariance between these parameters. There are two sources of *statistical* uncertainty that come into play here. The first is simply due to the statistical fluctuations of the photometric measurements. The second is due to the statistical fluctuations of the intrinsic lightcurve itself. Indeed, even if the lightcurves were perfectly measured, they would be found to fluctuate around the SALT2 templates. This fluctuation is *not* the same as the uncertainty in the model. Rather, the SALT2 model itself accounts for fluctuations in the SED of SNIa in addition to the stretch and color templates. These fluctuations are actually a part of the model.

The uncertainties we've discussed so far are due to *statistical* uncertainties only, and not the calibration uncertainties of the light curves themselves. Their contribution to the final covariance matrix is referred to as C_{stat} . It can be thought of as the sum of a block diagonal matrix that only concerns correlations of parameters for the same supernova, not between supernovae.

At this point, we still need to compute the correlation between different supernovae due to calibration uncertainties. Indeed, because the SALT2 model depends on the calibration parameters, a shift in these will produce a shift in both the model and light curves. This will in turn change the fit values across supernovae in a correlated fashion. In section § 6.4.1 we will describe how we compute these correlations that are due to the *systematic* uncertainties of the SALT2 model.

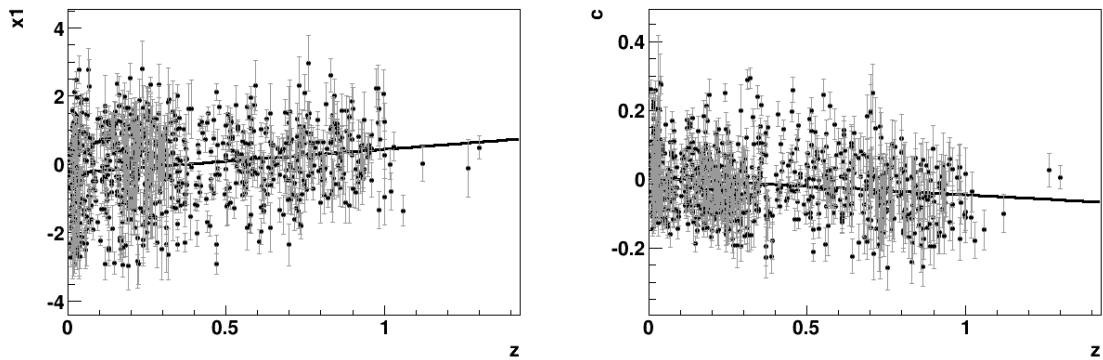
6.2.3 Simulating the SALT2 Uncertainty

The Moshier et al. (2014) paper describes in detail simulations that were run in order to ascertain any potential bias in the SALT2 training model. It consists of a Monte Carlo that uses the SNANA package (Kessler et al. 2009) to simulate both lightcurves and spectra similar to those used by the SALT2 training of Guy et al. (2010). A fiducial cosmology is chosen, and a number of realizations of these artificial datasets are produced. We then fit a SALT2 model, then a cosmology model on these datasets, and compare the output values to the input truth value. By varying the underlying models that generate the datasets and considering their impact on w , one can test for biases. In figure 6.4 we have an overview of this process.

The simulations can test the impact of a number of underlying assumptions in our analysis. For starters, our own analysis models part of the remaining intrinsic scatter in the lightcurves after color and stretch corrections as statistical fluctuations that are **uncorrelated** between passbands. These fluctuations cannot, however, change the absolute luminosity of the supernovae. The remaining intrinsic scatter in absolute luminosity is then interpreted as a coherent (i.e. wavelength independent) scatter in the magnitude of SNIa. One aim of the simulation has been to expand upon the work of Kessler et al. (2013) in an effort to better ascertain the potential impact of this modelization on the measured value of w . The simulations considered 3 models for the input intrinsic variability :

COH The first (called COH) refers to assuming that only a coherent scatter exists beyond the stretch and color templates and is the same magnitude variation at all λ and phases.

G10 The second (called G10) follows the magnitude dispersion model in the SALT2 training of Guy et al. (2010), which models the statistical fluctuations of lightcurves beyond stretch and color corrections. They sample this dispersion every 800Å and construct a complete



(a) Scatter plot of x_1 parameter as a function of redshift. (b) Scatter plot of c parameter as a function of redshift.

Figure 6.3: Evolution of standardization parameters as a function of redshift.

scatter model between the measured point using a sine interpolation. They then add a coherent scatter. This corresponds to the assumptions of the SNLS analysis.

C11 The last model (called C11) uses the magnitude covariance scatter model of described in [Chotard et al. \(2011\)](#), using data from the Supernova Factory. Because the covariances are given for broadband magnitudes, they again draw values at specific points and use a sine interpolation to produce a complete scatter model.

Simply put, the variability of the COH model has no color variations, that of the G10 model has both a colorless and colored component, and that of C11 is entirely color dependent. They also consider variations in the input spectral model of SNIa. Again, three models are considered :

G10 The first, (called G10) is the result of the SALT2 training of [Guy et al. \(2010\)](#).

G10' The second, (called G10') is a version of the latter that has been modified to contain no negative fluxes.

H The third model (called H) is based on the spectral templates of [Hsiao et al. \(2007\)](#). A stretch factor was artificially added to these templates by elongating them in time. This tests SALT2's ability to reproduce a time dilated SED using an additive template (as opposed to multiplicatively stretching its time parameter).

Note that all models use the same color law (that of [Guy et al. \(2010\)](#)) and have the same input range for stretch and color.

The simulations also distinguish between “ideal” and “real” training sets. The “ideal” training set represents a collection of light curves and spectra that should allow the training to reproduce the input model with very high accuracy. It exists to ensure that the SALT2 model can accurately reproduce a given input model given enough data. A “real” training set is one that resembles that of [Guy et al. \(2010\)](#). It is used to take into account the redshift distribution and signal to noise ratios that real experiments have to deal with.

In figure 6.5, we look at the difference between input and recovered distance moduli for different combinations of input models. The impact on cosmology is assessed by considering the impact of these differences on the value of w . The dominant effect is found to be the impact

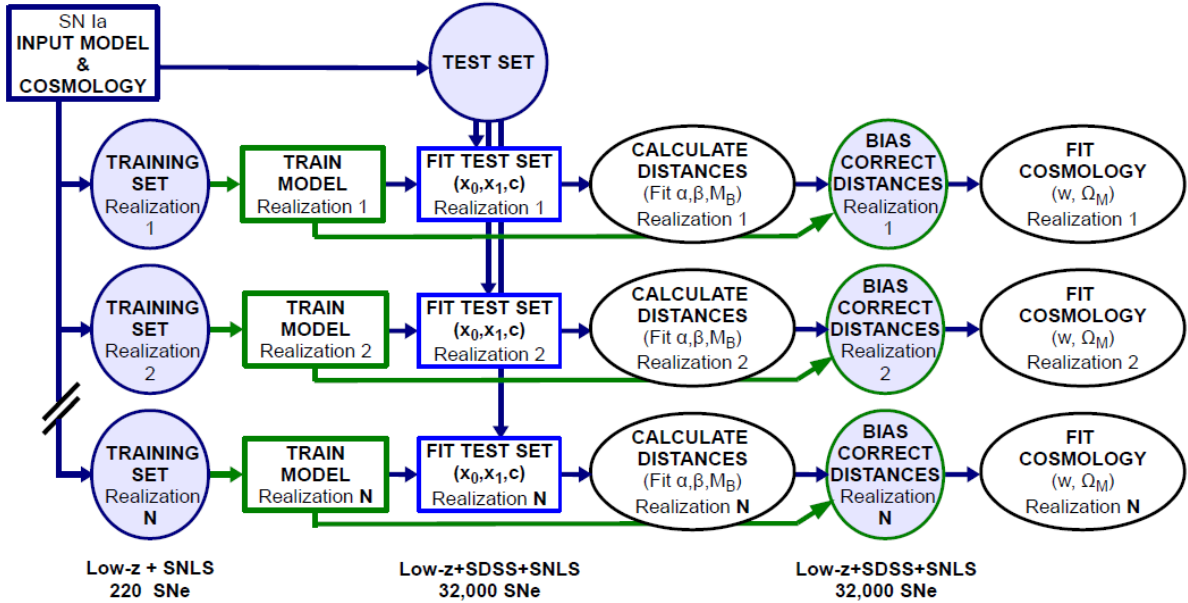


Figure 6.4: Diagrammatic overview of the simulation process. We begin by choosing the underlying input models for both the cosmology and the supernovae. This produces two sets of supernovae : one for SALT2 training, and one for cosmology. Once the training is complete, distance moduli are computed for the cosmology set. In turn, we correct these moduli for Malmquist bias, and fit a cosmology to them. We can then compare the input and output values of the cosmological parameters, in particular w .

of the scatter models. While the bias depends on both the input spectral and intrinsic scatter models chosen, the different results obtained lie within the uncertainty of the simulation results. The average bias is of $\Delta_w = -0.011 \pm 0.007$.

Different regularization models are also tested, though these are not found to change the distance moduli significantly.

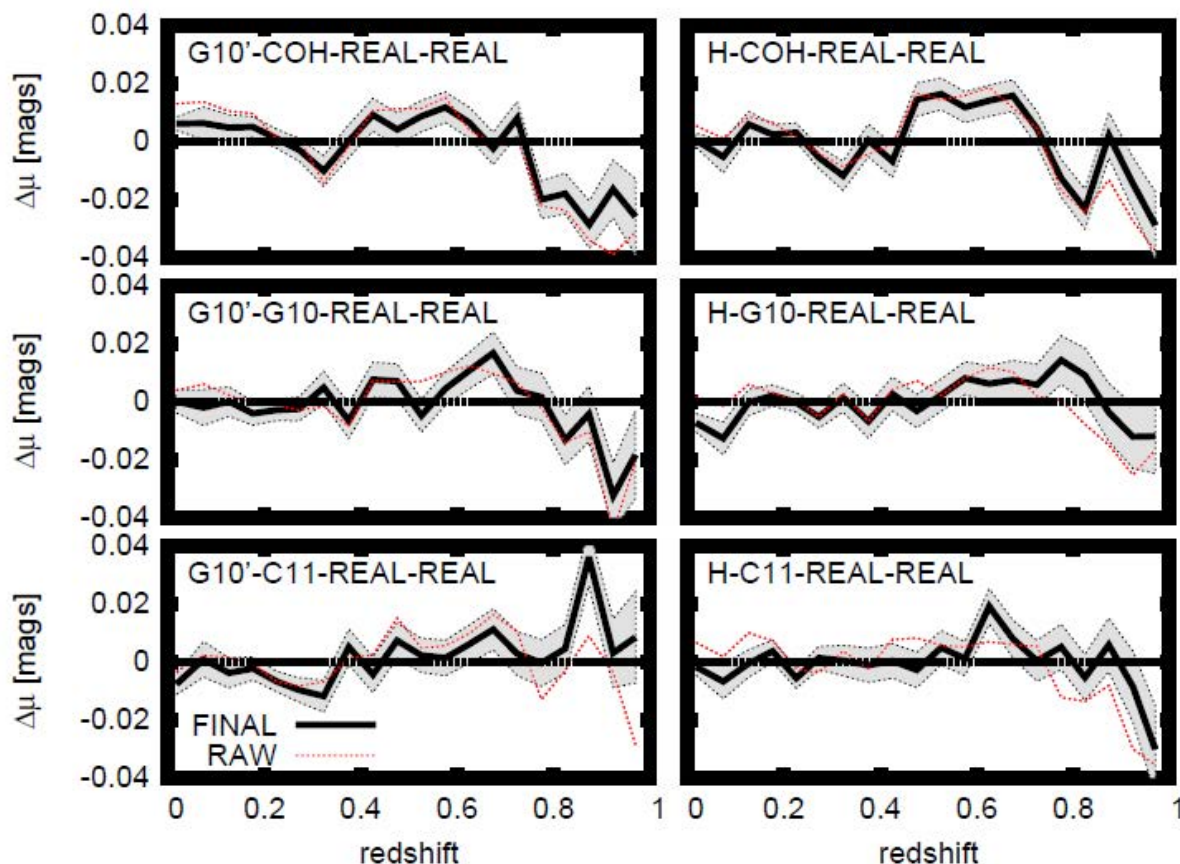


Figure 6.5: Difference between input and recovered distance moduli for various input models. The first two entries in the model name describe the input spectral and intrinsic scatter models. The last two indicate that a “real” training set was used.

6.3 Corrections

6.3.1 Host Galaxy Mass Corrections

As we have seen in section § 2.4.2, it has been repeatedly noticed (Kelly et al. (2010), Lampeitl et al. (2010), Gupta et al. (2011), Johansson et al. (2013), Sullivan et al. (2010), Childress et al. (2013), Pan et al. (2014)) that the distance modulus of a supernova correlates with the mass of its host galaxy. One can think of 2 approaches to take into account this correlation. We can assume that the host mass leaves an imprint in the lightcurve of the supernova, and retrain SALT2 while including this parameter. In other words, we would use the host masses in an attempt to more easily discern a third parameter in our principal component analysis. This work is currently in progress. In this section, we focus on a more straightforward method that directly modifies the distance modulus of equation 2.2 using the host mass. We begin by looking at how those masses are estimated.

6.3.1.1 Mass Estimation

The SNLS survey benefits from precise multiband photometry. In addition, carefully constructed supernova free deep stacks have been produced which allow us to investigate the prop-

erties of the host galaxies. Much like supernova light curves are fit to a model to determine their properties, we can fit the host galaxy’s photometric measurements to a mass dependent model. PEGASE is one such model, described in [Fioc & Rocca-Volmerange \(1997\)](#) and [Fioc & Rocca-Volmerange \(1999\)](#). It is a spectral evolution model of galaxies that can be used to extract galaxy properties given photometric observations of them. Likewise, the SDSS host galaxies benefit from measurements of similar quality, and are also fit to a PEGASE model. The masses are measured in units of $\log_{10} M_{\odot}$. The SNLS and SDSS host masses are measured to a precision of about 0.1.

A similar fit is not available for the collection of low redshift supernovae that enter our Hubble diagram. In most cases, the host galaxy photometry is not publicly available. We must rely instead on publicly available photometry. We choose here to use the photometry from the **2003 2MASS All-Sky Data Release** from the **Two Micron All Sky Survey** ([Skrutskie et al. 2006](#)) or 2MASS for short. The 2MASS survey delivers magnitudes in the K_S band for galaxies across the sky.

In [Bell et al. \(2003\)](#), it is shown that K_S magnitudes are good proxies for galaxy mass, in particular they are (nearly) color independent proxies. Indeed, [Bell et al. \(2003\)](#), using a collection of well determined galaxy masses, fit the following relation :

$$\log_{10}M = -0.4 \times \text{Mag} + c \times \text{color} + b \quad (6.5)$$

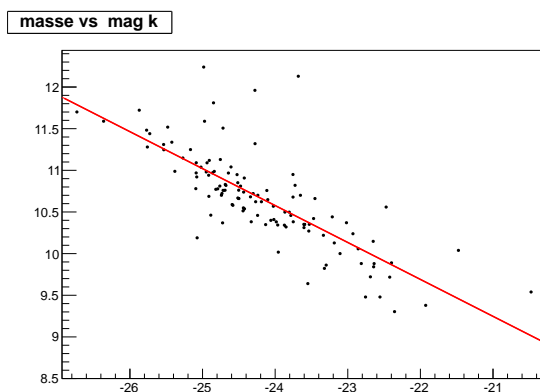
Where c and b are free parameters, M the galaxy mass, and Mag a magnitude in a chosen band. Defining color as $\text{Mag}_g - \text{Mag}_r$, and taking Mag to be the K_S magnitude, they find $(b, c) = (-0.2, 0.2)$. By comparison, taking Mag to be g band magnitudes we obtain $(b, c) = (-0.5, 1.5)$. In other words, the color correction term is roughly 8 times smaller when using the K_S band relative to the g band. This makes K_S magnitudes a better proxy for galaxy mass as they are more robust to uncertainties in the color correction. Using these K_S magnitudes, we fit a similar model to the data we will be using. That is :

$$\log_{10}M_{\text{model}} = a \times K_S + b \quad (6.6)$$

Where K_S is taken to be the **absolute** K_S band magnitudes, computed using a distance modulus given by NED. The distance modulus is computed using the redshift and assuming $h = 0.73$ (thus a redshift cut at $z > 0.008$ is set to ensure that the supernovae are in the Hubble flow), and a K-correction taken from [Bell et al. \(2003\)](#) is applied. The input masses are from [Neill et al. \(2009\)](#). We find $(a, b) = (-0.44, -0.06)$. This is similar to the -0.4 slope of the [Bell et al. \(2003\)](#) model. The slight difference is likely due to the a term incorporating the average color effect that our model does not account for. The value of b merely reflects the choice of calibration. Fitting a gaussian distribution around the fitted slope, we find an RMS of 0.16, which we include in our mass estimation uncertainty.

We also find that galaxy morphology biases the relation of equation 6.6, in that subdividing the sample based on galaxy morphology leads to residuals that, on average, display an offset from the fitted relation. The average residual of elliptical galaxies is of -0.1 , and that of spirals is of 0.1 . Because the morphology of the remaining galaxies will not be available to us, we add in quadrature an uncertainty term of 0.1 to the galaxy masses estimated using equation 6.6.

This work will be released in [Hardin \(2015\)](#), in preparation.

Figure 6.6: Fitting galaxy mass VS K_S magnitudes.

6.3.1.2 Implemented Correction

While a supernova's Hubble residual is clearly correlated with its host galaxy mass, the exact form of this correlation is still unclear. For the time being, we assume it is a step function. In other words, for masses above a certain cutoff, a correction is applied to the distance modulus. As we can see in figure 6.7, this cutoff is in the $10^{10}M_\odot$ range. The M_B term of equation 2.2 therefore becomes :

$$M_B = \begin{cases} M_B^1 & \text{if } M_{galaxy} < 10^{10}M_\odot \\ M_B^1 + \Delta_M & \text{otherwise} \end{cases} \quad (6.7)$$

Where the value of Δ_M is fit using the residuals to a Hubble diagram obtained without the use of a galaxy mass correction. These are the residuals seen in figure 6.7

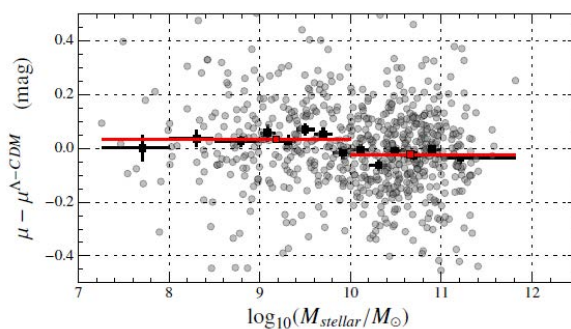


Figure 6.7: Hubble residuals as a function of galaxy mass, before any correction is applied, as obtained in the JLA analysis.

6.3.1.3 Uncertainty and Correlation Estimation

We consider two effects in computing the uncertainty on the galaxy mass corrections. The first is that the value of the mass step position is ill defined. Indeed, the choice of $10^{10}M_\odot$ is rather arbitrary, given that for any value between 10^9M_\odot and $10^{11}M_\odot$ the step in the residuals would have been just as significant. To this end, we assign correlated uncertainties to all supernovae whose inclusion in the high or low mass sample depends on the choice of the step position.

The second effect is that, since the correction is a step function, uncertainties on the galaxy mass only affect galaxies where the uncertainty is such that the galaxy cannot be ascertained to be in the high or low mass sample. The galaxy mass correction contribution to the covariance matrix of the M_B parameter can therefore be written as :

$$\begin{aligned}
 C_{host} &= \Delta_M^2 H_{low} H_{low}^\top + \Delta_M^2 H_{high} H_{high}^\top + \sigma_{correction}^2 & (6.8) \\
 (H_{low})_i &= \begin{cases} 1 & \text{if } 10^9 M_\odot < M_{galaxy} < 10^{10} M_\odot \\ 0 & \text{otherwise} \end{cases} \\
 (H_{high})_i &= \begin{cases} 1 & \text{if } 10^{10} M_\odot < M_{galaxy} < 10^{11} M_\odot \\ 0 & \text{otherwise} \end{cases} \\
 (\sigma_{correction})_{i,j} &= \begin{cases} \Delta_M^2 & \text{if } i = j \text{ and } |M_{galaxy_i} - 10^{10} M_\odot| < \sigma_{M_{galaxy_i}} \\ 0 & \text{otherwise} \end{cases}
 \end{aligned}$$

6.3.2 Peculiar Velocity Corrections

Computing peculiar velocities requires a map of the matter density in our local cosmological neighborhood. The peculiar velocity corrections implemented by the SNLS5 analysis employ the **2M++** (Lavaux & Hudson 2011) data compilation. It consists of a catalog of galaxies covering the entire sky up to a distance of $200\text{Mpc}/h$. It is used to construct a density field of the sky, characterized by the parameter β . This parameter is obviously not the same as the standardization parameter of the distance modulus. Rather, it is the logarithmic growth rate divided by the bias parameter b^1 . A first estimate of β is constructed using the iterative reconstructive method of Pike & Hudson (2005). The measured peculiar velocities of the **First Amendment** (Turnbull et al. 2012) and **SFI++** (Springob et al. 2009) datasets are then used to constrain the relationship between the luminosity density of galaxies and the motion of objects surrounding them. In this way a velocity field is constructed. This velocity field goes up to a redshift of $z = 0.067$.

The uncertainties on the correction lead to corresponding uncertainties on z . Rather than have 2 dimensional uncertainties, we transform σ_z into σ_{m_B} by assuming that the redshift of these supernovae is $z = H_0 \times d_L$, which is true enough for nearby supernovae.

Note that, while this method provides independent uncertainties for each peculiar velocity correction, the uncertainties are actually correlated due to the fact that the uncertainty on β affect all the measurements. Because the velocities are linear in β , we assess these correlations by varying all the velocities by a factor of 10% and computing their impact on the effective m_B . We use the resulting Jacobi matrix to compute a covariance matrix associated with this correction. We call this matrix C_{pecvel} .

In addition, it has been pointed out in Hui & Greene (2006) that interpreting magnitudes for moving supernovae is not a trivial task. Indeed, for a supernovae moving at speed v (where a positive v represents motion away from us), we must shift the observed magnitude by :

$$\Delta_{mag} = -5 \times \log_{10} \left(1 + \frac{v}{c} \right) \quad (6.9)$$

Note that there is some disagreement on what the actual magnitude shift should be due to peculiar velocities. For example, Davis et al. (2011) distinguishes the contributions due

¹The bias parameter b of a matter tracer x relates its density contrast to the total matter density contrast : $b = (\rho_x / \langle \rho_x \rangle) / (\rho_{matter} / \langle \rho_{matter} \rangle)$. $b = 1$ corresponds to a perfect matter tracer.

to Doppler shifts (which includes our own motion relative to the CMB) from the relativistic beaming due to the motion of the supernova. Fortunately, this correction is so small for the supernovae in our survey that differences in its application have a negligible impact on the final cosmology. Indeed, the shift in cosmological parameters when excluding peculiar velocity corrections altogether is imperceptibly small, as we shall see in section § 6.5.3.1.

Finally, we also take into account the possibility of an unmeasured bulk flow of 150km/s. To do this, we add an uncertainty on the distance modulus by assuming a constant $H = H_0$, which is only approximately true for low redshift supernovae. This is not a problem given that the uncertainty is only significant for these low redshift supernovae. The added uncertainty on μ therefore takes the form :

$$\sigma_{\text{bulk flow}}(z) = \left(\frac{5\sigma_z}{z \log 10} \right)^2 \quad (6.10)$$

$$c \times \sigma_z = 150\text{km/s}$$

6.3.3 Malmquist Bias Correction

To estimate the value of the Malmquist bias² for each survey at each redshift, we employ Monte Carlo simulations that use the SNANA simulation package (Kessler et al. 2009). A number of artificial SNIa are created, with a known distance modulus. We then fit these supernovae using SALT2, and compute their distance modulus using an α and β fit on a combined simulated sample of low redshift, SDSS, and SNLS data. Obviously, which supernovae are included in the fit depends on a survey dependent selection function, which is what reproduces the Malmquist bias. This bias is computed in any chosen redshift bin as the average difference between the input value of μ and the one recovered by the fit. As we will see, the question of determining selection functions is an ill defined problem.

For the SNLS and SDSS surveys, while the searches were somewhat automated, which supernovae were slated for spectroscopy ultimately depends on a combination of human factors that are hard to simulate. This introduces uncertainties to our selection function. In addition, even if we could approximate these surveys as purely automated flux limited surveys, the impact of Malmquist bias depends on the SNIa model used to compute it, whose own uncertainty therefore propagates to the selection function.

Still, the decision making processes of these surveys are regular enough that their selection function are essentially equivalent to their spectroscopic efficiency function. We model these as a functional form in peak i band magnitudes for SNLS, and in peak r and $g-r$ color magnitudes for SDSS, whose parameters are chosen such that they reproduce the observed redshift distribution of supernova parameters in their respective surveys (this is done in Kessler et al. (2013) for SDSS). The uncertainty on these parameters is mainly statistical, determined by the limited number of supernovae whose redshift distribution these functions are trying to reproduce.

The low redshift surveys, on the other hand, are not flux limited. They rely on a strategy of periodically revisiting selected galaxies. One might assume that this implies that such a sample does not suffer from Malmquist bias, but the fact that the average supernova color evolves with redshift in this sample suggests otherwise. To this end, while we employ the same method for low redshift supernovae as we do for SNLS and SDSS supernovae, we compare the results to the case where we assume that no bias exists. The difference between the two is added as an uncertainty

²The Malmquist bias is the tendency for flux limited surveys to detect objects whose brightness is higher than the average population of that object, in particular near the flux limit of that survey.

to the obtained parameters of the selection function. Note that assuming no bias whatsoever on low redshift supernovae shifts the value of Ω_m by 10 times less than the uncertainty on Ω_m , so the impact of its existence or lack thereof is marginal.

Using these selection functions, we can use Monte Carlos to determine the expected bias in each redshift bin. Fitting a polynomial to these bins, we can now correct the bias of any supernova given its redshift and survey. These polynomial fits can be seen in figure 6.8. The uncertainty on the polynomial coefficients is propagated as an uncertainty on the correction, itself added as an uncertainty on m_B in the final covariance matrix. The covariance matrix corresponding to this correction alone is referred to as C_{bias} .

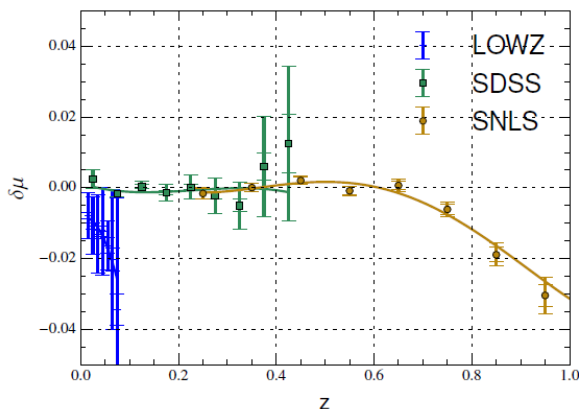


Figure 6.8: Expected Malmquist bias for each survey as a function of redshift. The smaller error bars represent the Monte Carlo statistical limitation alone, while the larger ones include the uncertainty on the selection function. Taken from [Betoule et al. \(2014\)](#).

Incidentally, such a correction will also correct any redshift dependent fitting bias when extracting the SALT2 parameters. Finally, the high redshift HST supernovae are argued to be bias free in [Conley et al. \(2011\)](#).

6.3.4 Dust Correction

All supernovae are corrected for Milky Way extinction due to local galactic dust. The correction uses the **Cardelli-Clayton-Mathis** (CCM) law detailed in [Cardelli et al. \(1989\)](#). To understand this law we introduce a few definitions :

$A(\lambda)$ This is simply the dust extinction (in magnitude) at a given wavelength λ .

$E(B-V)$ This is the difference in dust extinction between the B and V bands. In other words : $E(B-V) = A(B) - A(V)$. We use the maps of $E(B-V)$ provided by [Schlegel et al. \(1998\)](#).

R_V This is defined as $A(V)/E(B-V)$. We introduce this quantity because it characterizes the CCM law, as we shall see in equation 6.11.

The CCM law models the dust extinction at any wavelength as :

$$A(\lambda) = R_V \times f(R_V, \lambda) \times E(B-V) \quad (6.11)$$

Where $f(R_V, \lambda)$ is a function of wavelength that changes with R_V . We follow the prescription of [Cardelli et al. \(1989\)](#) and take $R_V = 3.1$.

Associated with this correction is an uncertainty on the value of $E(B - V)$. As such, we can expect that the covariance matrix associated with this correction is purely diagonal. However, the very relation between dust column density and extinction is itself uncertain. An error in this relation will affect all corrections similarly, introducing correlations. The [Schlegel et al. \(1998\)](#) paper estimates an uncertainty of 10% when converting dust density to extinction. To this end, we vary the value of $E(B - V)$ by 10% for all supernovae. Again, we use the resulting Jacobian to determine the corresponding covariance matrix. There is, however, some debate as to the accuracy of the maps used by [Schlegel et al. \(1998\)](#) (see, for example, the discussion in [Schlafly & Finkbeiner \(2011\)](#)). To ensure that we do not underestimate the resulting uncertainties, we conservatively decide to double their value. The covariance matrix associated to this effect alone is referred to as C_{dust} .

6.4 Fitting the Hubble Diagram

6.4.1 Correlated Calibration Systematics

To take into account the correlative effect of calibration uncertainties, we vary the values of all calibration quantities by a small amount, and produce SALT2 parameters for each supernova at each variation. The zero points are shifted by 0.01 in magnitude, and the central wavelength of each band shifted by $1nm$. At each variation, a new SALT2 model is produced and the supernova lightcurves, which have also been shifted accordingly, are fit to that model. By comparing the results of the variations with the results of the unvaried sample, we compute the Jacobian of the SALT2 parameters with respect to the calibration quantities. The contribution of calibration quantities with respect to the covariance matrix of the supernova parameters is then considered to be :

$$C_{cal} = JC_{\kappa}J^T \quad (6.12)$$

Where C_{κ} is the covariance matrix of the calibration quantities themselves, and J is the computed Jacobian. Note that C_{κ} is mostly diagonal, except for some correlations between the SDSS and SNLS zero points due to the intercalibration discussed in the previous chapter.

6.4.2 Determining σ_{coh}

Despite correcting for stretch and color, some intrinsic scatter remains in SNIa luminosities. As we have seen in the G10 model of section § 6.2.3, we assume that the remaining variability after stretch and color corrections can be modeled as the combination of two factors :

- One is a statistical fluctuation about the SALT2 model that doesn't alter the SNIa luminosity. This fluctuation is independent from one wavelength to the next.
- The other is a wavelength independent scatter (i.e. that is coherent across the SED).

We can therefore summarize the scatter about the Hubble diagram with a single degree of freedom denoted σ_{coh} . We need to account for these when computing the χ^2 of the fit. One

unfortunate consequence of this is that the χ^2 of the cosmology fit loses some of its power as a test of the statistical validity of the data and its uncertainty. However, as we shall see in the next paragraph, we actually fit one σ_{coh} per survey. This means that the fit χ^2 is actually a consistency check between the different surveys that ensures that all surveys are indeed measuring the same cosmology.

A simplistic model would have only one σ_{coh} for all supernovae in the sample. However, the residual scatter will depend on the accuracy with which each survey has determined its own magnitude uncertainties. To this end, we fit one σ_{coh} per survey by fitting a Hubble diagram to the survey data using a very general cosmology model, then finding one σ_{coh} per survey such that the survey's contribution to the distance modulus χ^2 (which we will see in equation 6.19) is equal to the number of supernovae in that survey (i.e. $\chi^2/d.o.f = 1$).

In figure 6.9, we split the JLA sample into multiple subsamples and compute a σ_{coh} for each. While a visual trend in redshift may seem apparent, the results are actually consistent with a redshift independent σ_{coh} .

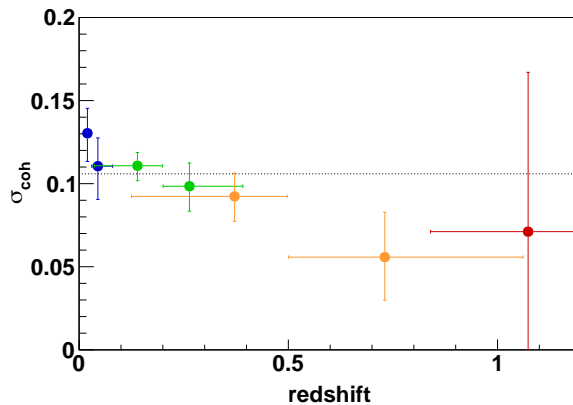


Figure 6.9: In order of redshift, the samples are the low- z subsample at $z < 0.03$ and $z > 0.03$, the SDSS subsample at $z < 0.2$ and $z > 0.2$, the SNLS subsample at $z < 0.5$ and $z > 0.5$, and the HST subsample. Despite appearances, the points are consistent with a redshift independent σ_{coh} .

As stated, the σ_{coh} model implies that scatter in brightness represents a wavelength independent scatter. We have already investigated the reliability of this assumption in section § 6.2.3.

It has been noted (Kronborg et al. 2010) that gravitational lensing may also be a contributing factor to the observed dispersion of SNIa luminosities. In our analysis, we follow the recommendations of Jönsson et al. (2010) and add a term to take these effects into account. The added uncertainty on μ is $\sigma_{lens} = 0.055$.

6.4.3 Constraints from Other Cosmological Probes

As we have seen in section 1.3.3.1, CMB observations provide constraints on the value of Ω_b , Ω_{CDM} , and θ^* , the angular size of the sound horizon. This information is used to construct a prior that will contribute to the χ^2 of the cosmology fit. The CMB constrains physical densities, and not their values relative to the critical density. Therefore, rather than constrain Ω_b and Ω_{CDM} , it instead constrains $\omega_b = \Omega_b h^2$ and $\omega_{CDM} = \Omega_{CDM} h^2$ (where h is defined such that $H_0 = h \times 100 km.s^{-1}.Mpc^{-1}$). We take the uncertainties and covariances of these parameters provided by Planck Collaboration et al. (2013b) to construct a covariance matrix C_{CMB} . However, since

our own supernova observations do not constrain H_0 , we marginalize over its value during the fit.

Defining ν_{CMB} to be the vector of values delivered by [Planck Collaboration et al. \(2013b\)](#), we define the CMB contribution to the χ^2 as :

$$\chi_{CMB}^2 = (\nu_{model} - \nu_{CMB})^T C_{CMB}^{-1} (\nu_{model} - \nu_{CMB}) \quad (6.13a)$$

$$\nu_{CMB} = (\omega_b, \omega_c, 100 \times \theta^*) = (0.022065, 0.1199, 1.041) \quad (6.13b)$$

$$C_{CMB} = 10^{-7} \begin{pmatrix} 0.79039 & -4.0042 & 0.80608 \\ -4.0042 & 66.950 & -6.9243 \\ 0.80608 & -6.9243 & 3.9712 \end{pmatrix} \quad (6.13c)$$

For the BAO prior, as we have seen in equation 1.28 of section 1.3.3.2, the measured observable comes in the form of an angular distance d_z for each redshift bin. Here we follow the scheme of [Planck Collaboration et al. \(2013b\)](#) and consider measurements in 3 redshift bins given by [Beutler et al. \(2011\)](#), [Padmanabhan et al. \(2012\)](#), and [Anderson et al. \(2012\)](#), considered to be independent measurements. The corresponding measurements are contained in the vector \mathbf{d}_z^{BAO} . We can now define the BAO contribution to the χ^2 as :

$$\chi_{BAO}^2 = (\mathbf{d}_z^{BAO} - \mathbf{d}_z^{model})^T C_{BAO}^{-1} (\mathbf{d}_z^{BAO} - \mathbf{d}_z^{model}) \quad (6.14a)$$

$$\mathbf{d}_z^{BAO} = (d_{0.106}^{BAO}, d_{0.35}^{BAO}, d_{0.57}^{BAO}) = (0.336, 0.1126, 0.07315) \quad (6.14b)$$

$$C_{BAO}^{-1} = \begin{pmatrix} 4444 & & \\ & 215156 & \\ & & 721487 \end{pmatrix} \quad (6.14c)$$

6.4.4 Overview of the Fit Method

The final covariance matrix used is a $(3\#SN) \times (3\#SN)$ matrix, where the 3 represents the number of light curve parameters per supernova (m_b , x_1 , and c). It is the sum of all the previously discussed covariances :

$$C_{total} = C_{stat} + C_{cal} + C_{model} + C_{bias} + C_{host} + C_{dust} + C_{pecvel} \quad (6.15)$$

Here we recall equation 2.2 which defines the distance modulus of the supernovae as a function of its light curve parameters. The estimator of this distance modulus is given by :

$$\hat{\mu} = m_B^* - M_B + \alpha \times x_1 - \beta \times c \quad (6.16)$$

In order to compare the distance modulus estimator with a model, it would be useful to propagate C_{total} to C_μ . If η is the $3 \times \#SN$ matrix of light curve parameters, then one can write :

$$\begin{aligned} \hat{\mu} &= A\eta - M_B \\ A &= (1, \alpha, -\beta) \end{aligned} \quad (6.17)$$

Where A encodes the relationship between μ and the light curve parameters of equation 2.2. Note that the values for α and β are updated at each step of the fit. M_B is the absolute

magnitude of SNe corrected for the galaxy mass. In addition to propagating C_{total} to C_μ , we also add the σ_z term discussed in equation 6.10 of section § 6.3.2, and the σ_{coh} and σ_{lens} terms discussed in section § 6.4.2, .

$$C_\mu = AC_{total}A^T + \left(\frac{5\sigma_z}{z \log 10}\right)^2 + \sigma_{lens}^2 \times z + \sigma_{coh}^2 \quad (6.18)$$

Note that α and β are part of the fit parameters, and A depends on these parameters. In other words, C_μ is recalculated at every step. We can now define the χ^2 we seek to minimize. For example, when fitting a flat Λ CDM model with fixed H_0 , this is :

$$\chi^2 = (\hat{\mu}(\alpha, \beta) - \mu_{model}(z; \Omega_m, \alpha, \beta))^T C_\mu^{-1} (\hat{\mu}(\alpha, \beta) - \mu_{model}(z; \Omega_m, \alpha, \beta)) + \chi_{prior}^2 \quad (6.19)$$

The variables on which μ_{model} depends will vary depending on the cosmological fit. Note that the parameter space includes all cosmological parameters, as well α and β . As we have seen, the distance modulus of the supernovae depends on the value of α and β . It is interesting to note that this means that one cannot construct a model free Hubble parameter using supernovae by merely placing each supernovae on the redshift VS distance modulus plane, because the value of the distance modulus will depend on the cosmological model we are fitting. This is not of particular concern given that the values of α and β are uncorrelated with those of the cosmological parameters, as can be seen in figure 6.10. This means that we can release a cosmology independent Hubble diagram by marginalizing over their values and binning the values of μ . Thus, we can provide outside parties with a vector of values of μ evenly spaced in redshift with a corresponding covariance matrix. This enables them to minimize the χ^2 of equation 6.19 directly, without having to sift through the intricate details of the analysis. This is detailed in appendix E of [Betoule et al. \(2014\)](#).

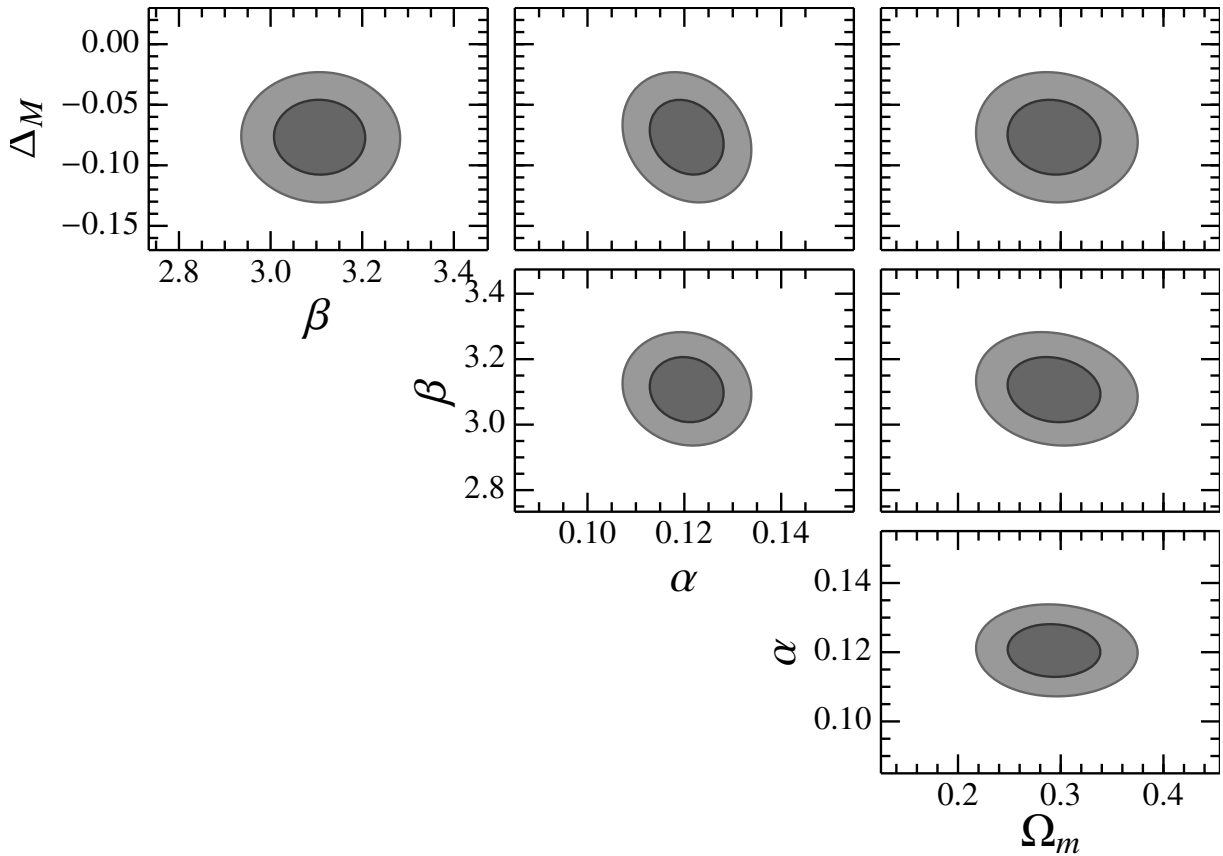


Figure 6.10: Confidence contours of the nuisance parameters and Ω_m . Note that the contours in nuisance parameter VS Ω_m space lack significant diagonal tilts.

6.5 Cosmological Results

6.5.1 A Blinded Analysis

The analysis was actually run **blindly**. What this means is that another member of the research group has artificially changed the values of the supernovae fluxes so as to alter the cosmology they describe. This is so as to finalize the analysis without knowing the impact of any tweak to the pipeline on the final values of the cosmology, thus avoiding confirmation bias.

However, a downside to this is that the uncertainties given on these cosmological parameters can't be compared to those of previous analyses, in particular that of JLA. This is because inferred cosmological parameters are not a linear function of the distance moduli and hence, for fixed errors on distance moduli, the uncertainties on the cosmological parameters will depend on their best fit value. To get around this, we used a trick dubbed **semi-deblinding**, in which the values of the distance moduli are artificially reinflated so as to recuperate the same cosmology as JLA. To do this, we simply added to our values of m_B the difference between the JLA cosmology and our fit cosmology. Note that despite this the data is still blinded, as this process does not allow us to infer what the blinding offsets were. For this section, one is to assume that the data discussed are the completely blinded data, except when stated otherwise.

In addition, we note that the cosmological model we fit to is that of a flat w CDM model. In other words, we assume a flat universe, but leave open the question of Ω_m and the equation of state of dark energy as characterized by the parameter w .

6.5.2 Comparison with JLA Analysis

As a consistency check, we directly compare the residuals of our Hubble diagram with those of the JLA analysis. Obviously, we can only do this for the subset of supernovae that are in both analyses, but this is a total of 687 supernovae, a sizeable portion of our own total of 960 supernovae. To do this, we look at the histogram of differences between the two residuals divided by their JLA uncertainty to get an idea of the spread between the two, as seen in figure 6.11. Because we are comparing residuals to the Hubble diagram and not values of μ , the blinding has no impact on this comparison. Unsurprisingly, 96.2% of differences lie within one sigma of each other, and 80.5% lie within half a sigma of each other, indicating that the two are indeed strongly correlated, and that no significant shift has been introduced.

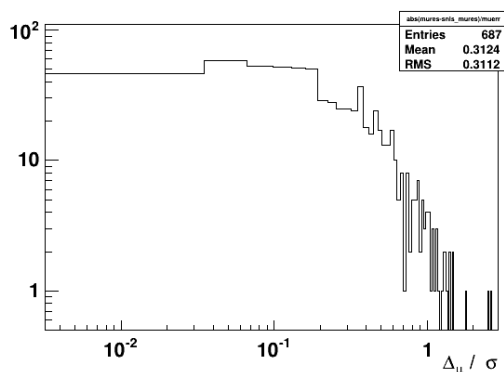


Figure 6.11: Histogram of difference in Hubble residual relative to JLA uncertainty, in absolute value.

6.5.3 Impact of Corrections

We investigate the effect of the corrections implemented by refitting the cosmology without the tested correction. We again remind the reader that the shifts in w discussed below concern the *blinded* values. These shifts are also given as a relative value to the blinded σ_w so as to get an idea of their significance.

6.5.3.1 Peculiar Velocity Corrections

The impact of peculiar velocity corrections are found to be completely negligible. When they are ignored, none of the cosmological parameters move in a remotely significant way. Indeed, ignoring them shifts the value of w from -0.8568 to -0.8573 . This represents a shift 1% of σ_w . This means that our analysis is highly robust to peculiar velocity effects. This has not always been the case for SNLS cosmology analyses, and is due to the addition of the SDSS supernovae that reduce the relative weight of nearby SNIa in the hubble diagram.

6.5.3.2 Host Galaxy Mass Correction

The mass step is found to be 8% in magnitude. Ignoring this correction shifts the value of w by 0.009, which is almost 20% of σ_w , making it a noticeable correction. As future experiments decrease σ_w , this impact will become more significant. It is therefore critical for the future of supernova cosmology that we gain a better understanding of the host mass/luminosity correlation. In particular, the crude mass step model may no longer suffice for experiments hoping to

reach percent precision on w , and a host mass correction may no longer be a useful model if it is found to be a poor proxy at the subpercent level for some other underlying correlation.

6.5.3.3 Selection Effects

Finally, we explore what happens if we ignore the supernovae that were removed by either visual inspection or 3-sigma clipping. This represents 22 supernovae in total. Including them shifts the value of w by 10% of σ_w . While this may seem worrisome, keep in mind that 2 of these outliers were over 5-sigma, and many were identified as peculiar type Ia in other works.

6.5.4 Preliminary Analysis Results

The results of the w CDM fit for the blinded data are seen in table 6.3. The corresponding Hubble diagram is seen in figure 6.12a.

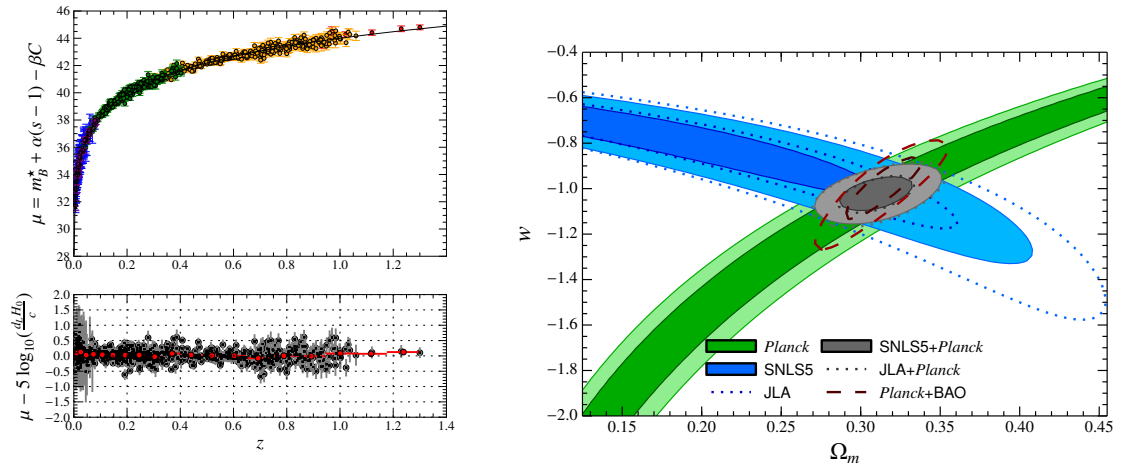
Table 6.3: Results of fit for flat w CDM model, for blinded data.

Parameter	Value	σ
α	0.146	0.00584
β	2.99	0.0593
Mass step	0.0809	0.0204
Ω_m	0.335	0.0129
w	-0.860	0.0502
$\Omega_b \times h^2$	0.0223	0.000268
H_0	64.5	1.21

We semi-deblind the data and fit the cosmology again in order to compare the resulting uncertainty on w . The JLA uncertainty on w was of 0.055. The new and improved uncertainty is of 0.048, an increase of about 0.01 in precision. Much of this improvement comes from the new SALT2 model. Indeed, fitting the same data with the old model only brings the uncertainty down to 0.053. We recall that JLA had also implemented the new calibration, and therefore most of the improvement comes from the new SALT2 model.

After semi-deblinding, we also plot confidence contours in the w VS Ω_m plane, alongside the contours of the available constraints from other probes, seen in figure 6.12b. Note that the two contours are very complementary. In addition, the figure makes clear that SNIa are still the single most constraining probe when studying the nature of dark energy.

In preparation for my thesis, I ran simple simulations whose objective it was to estimate the expected gain in precision as a result of the upcoming improvements in SNLS. The simulations worked by constructing a Fisher matrix that corresponded to the weight of all supernovae, as well as including a few entries for the cosmological parameters. Given the structure of the Fisher matrix used, one could quickly compute the resulting uncertainty on the cosmological parameters without having to invert the entire matrix. In figure 6.13, we explore a number of different scenarios and the expected uncertainty on w that would result from them. Comparing our current results to point 4 on the figure ($\sigma_w = 0.058$), we can see that we have exceeded our expectations in terms of gain in precision. This is mostly due to the recalibration, as the JLA analysis had already surpassed this mark. On the other hand, the increase in precision from JLA to SNLS5 (which roughly corresponds to a jump from point 2 to point 3) led to the expected gain of 1% in uncertainty on w .



(a) Hubble diagram for flat w CDM fit for semi-blinded data.

(b) Confidence contours in the Ω_m VS w plane for semi-deblinded data. We also plot the JLA contours for comparison.

Figure 6.12: Distribution of the full supernova sample (before cuts).

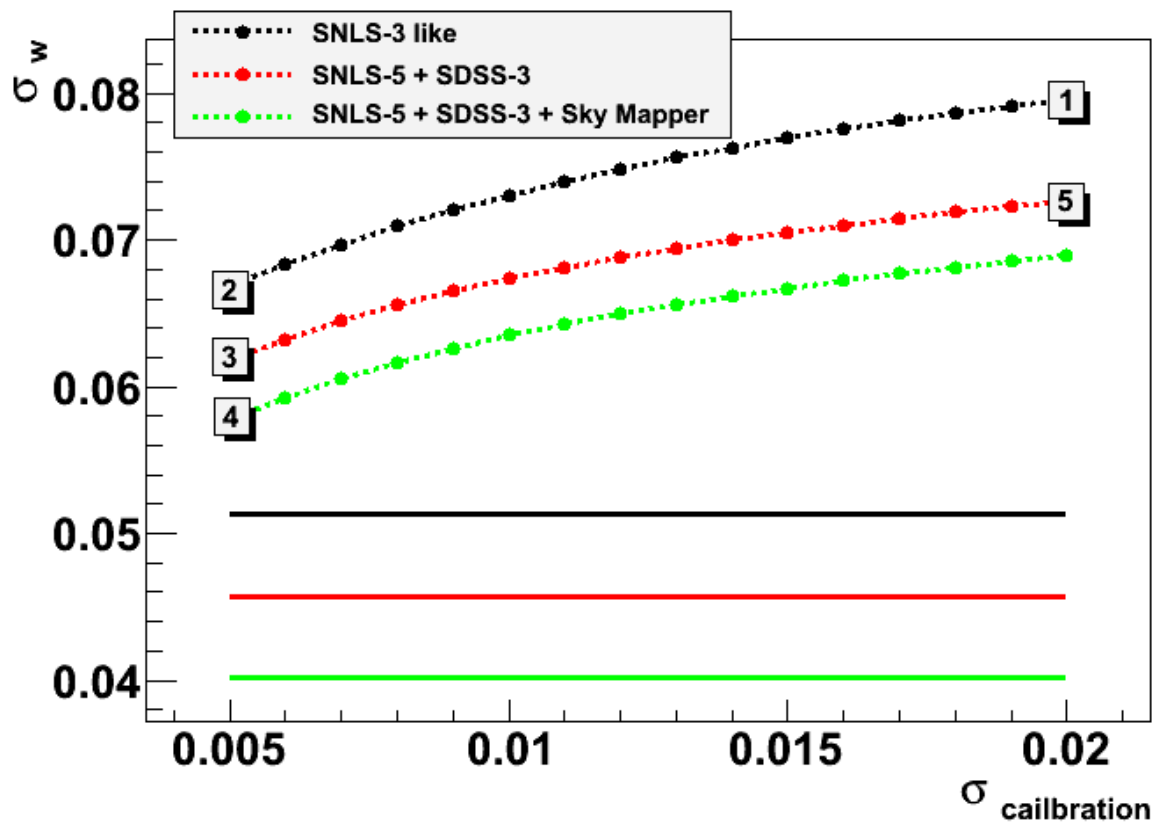


Figure 6.13: Expected uncertainty on w for various scenarios computed using an artificial Fisher matrix. The x-axis represents a change in the zero point uncertainty in all bands. The solid lines represent the statistical uncertainty on w for various color coded data samples : black corresponds to the SNLS3 data sample, red corresponds to the addition of the final SNLS and SDSS data, and green represents the addition of 300 low redshift supernovae. Points 1 and 2 represent the SNLS3 analysis, before and after recalibration. Points 5 and 3 represent the addition of new supernovae to both the SNLS and SDSS samples, again before and after recalibration. Point 4 represents the addition of new low- z data, after recalibration.

Conclusion

We have presented the current state of the preliminary SNLS5 analysis. This analysis has benefited greatly from past work, and is the direct successor of the JLA analysis. In this manuscript I have presented the novelties that my own thesis work has contributed to the final analysis. These are :

- Monte Carlo simulations meant to validate the photometry.
- A new scheme for the computation of zero points and a better understanding of the biases involved therein.
- Data processing of the SNLS5 images.
- A new training of the SALT2 model.
- The cosmology analysis of the final supernova sample.

The combination of these improvements is expected to lead to a decrease on the uncertainty on w from 0.055 to 0.048. While these results are promising, there are actually still a few things that may be done to increase the precision of the SNLS5 analysis. For starters, we must take better care in selecting the data that enters the SALT2 training sample. As it stands, the SALT2 spectral inputs have only undergone minimal quality cuts, and in particular have not yet been visually inspected. In addition, the SALT2 algorithm itself may be modified to take into account flux calibrated spectra, as opposed to recalibrating them using corresponding light curves. This could prove especially useful when exploiting the data available for the very nearby 2011fe. Finally, exploiting data from the recent **PAN Starrs** survey could prove invaluable in validating our calibration measurements. We hope to accomplish these improvements in the near future. The SNLS5 analysis is slated to be published in 2015, and according to what we have seen thus far it will provide the most precise measurement of w to date.

In presenting the current state of the SNLS5 analysis, we have shown the reader the current state of the art of supernova cosmology. SNIa remain the most important tool at our disposal for ascertaining the nature of dark energy. To remain competitive in the coming generations of cosmology experiments, some challenges lie ahead for those working in the field.

The upcoming **Large Synoptic Survey Telescope** ([LSST Science Collaboration et al. 2009](#)) is expected to observe over a hundred thousand SNIa every year. Confirming such a large number of supernovae spectroscopically will be prohibitively expensive. Indeed, these

observations require a lot of time (roughly an hour per SN) on very large telescopes, and are therefore very expensive. To this end, methods are currently in development that can confirm a supernova’s type using only photometric confirmation. This research is ongoing within both the SNLS (Bazin et al. 2011) and SDSS (Sako et al. 2011) collaborations. Note that these methods can count on having spectroscopic redshifts of the host galaxies, as those can be measured using multiplexed observations of many host galaxies using wide field multi-objects spectrographs, as described in Lidman et al. (2013).

In addition, such a large SNIa sample will not yield the cosmological constraints that it otherwise could if the systematic uncertainties in play are dominant. The current most significant systematic uncertainty comes from the calibration errors seen in table 5.3 of chapter § 5. These will have to be reduced if we are to take advantage of ever larger samples of SNIa. One such effort to reduce calibration uncertainties is to use certain types of white dwarves whose spectra are exceptionally close to perfect black bodies (Fix et al. 2014). This will greatly reduce the uncertainties incurred as a result of modeling the SED of the primary calibration stars.

As the calibration uncertainties decrease, it will become ever more crucial to better understand SNIa properties, as these will become a comparable source of systematic error. The most worrying aspect of supernova cosmology is the indistinguishability between an unstandardized redshift evolution of supernova luminosity and new cosmology. Since galaxy masses evolve with redshift, our current uncertainty on the galaxy mass correction of section § 6.3.1 acts as a proxy for the uncertainty on this evolution. It is likely that the galaxy masses are themselves proxies for some another more physically motivated underlying correlation. If we are to reduce the uncertainties due to SNIa properties, it is important that we move past this logic of “proxies” and gain a proper understanding of the real correlations that are in play. As we have seen in section § 2.4, research is ongoing on this front.

Finally, even assuming all these efforts were to come to fruition, they would mostly serve to constrain the *present day* nature of dark energy. If the value of w is consistently found to be compatible with -1 , then the next challenge for observers will be to ascertain if this is the case throughout the history of the universe. As we have already seen in figure 1.6 of chapter § 1, the redshift evolution of w is almost completely unconstrained by the current data. This will prove challenging because it requires extending the Hubble diagram to higher redshifts with a similar or even superior level of accuracy in our measurements given that dark energy becomes subdominant at higher redshifts. This will require space based observations in order to avoid the infrared cutoff of the atmosphere for high redshift observations. The upcoming space based EUCLID mission (Laureijs et al. 2011) will provide such observations. Simulations presented in Astier et al. (2011) suggest that such observations could constrain w_a on the order of 0.4. While this is far from the few percent level of constraint on present day w , it is a step in the right direction. It should be noted that the jump from SNLS3 to JLA only reduced the uncertainty on w_a from 0.563 to 0.552. There is therefore little hope in improving this uncertainty using ground based observations.

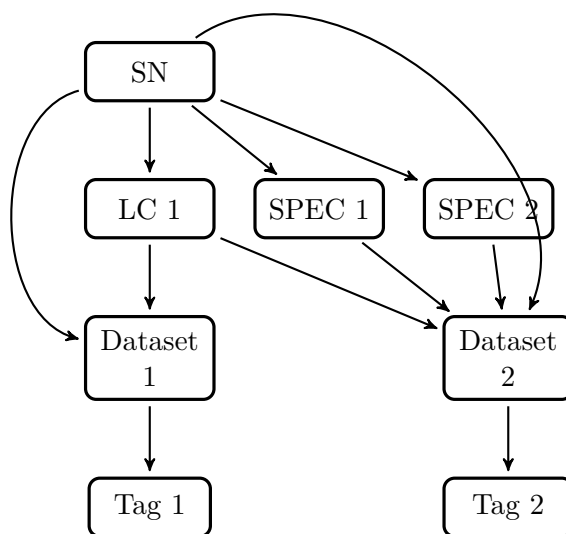
These challenges should not be taken as an indictment of supernova cosmology. On the contrary, they present the many avenues of research that promise to keep supernovae relevant in the 21st century. Supernova cosmology is in the peculiar position of being both a mature science and one with much room to evolve. As my own career progresses, I will likely not remain in this field and move on to other probes of dark energy. It will, however, be reassuring to have my future findings be in accordance with a tried and tested method that is the most direct measurement of expansion one can ever think of : comparing distances to redshifts.

Appendices

Appendix A

The Supernova Database

All the supernovae from all the surveys used have been added to a local database. This database will be made accessible online with the release of the final analysis paper. Each of the samples used, be it the purely photometric sample used for the cosmology or the mixed photometry/spectroscopy sample used for model training, corresponds to a database tag, which will also contain any and all configuration associated with the sample. This will make it easier for outside researchers to reproduce our analysis.



The database is designed so as to tag the variety of data available for each supernova depending on the required use of the tag. In the example above, tag 1 corresponds to the cosmology sample, containing only the light curve data, whereas tag 2 corresponds to the training sample as it contains the spectroscopic data as well.

Appendix B

Zero Point Robustification

The values for m_{APER} used in equation 5.15 are those given by the calibration catalogs produced by (Betoule et al. 2013). It is of note that certain measurements of m_{APER} are thought to be biased. In order to understand this, we note that during aperture photometry, only objects past a certain brightness are detected and measured. Similarly, only objects below the saturation threshold are measured. For stars that are particularly dim, this will select only such images where the statistical fluctuation was positive. Conversely, for bright stars, negative fluctuations will be privileged. Also, stars that have been measured in a particularly low number of images can fall into either category. To avoid being biased by these measurements, we define an acceptable magnitude and number of measurements ranges. To do this, we consider the patterns observed in the magnitude VS number of measurements plane, seen in figure B.2. These figures are scatter plots where each point represents one series of calibration measurements for a given tertiary star. The effects of saturation are seen as a sudden drop in the number of measurements of low magnitude stars. The effects of detection (or lack thereof) of dim stars are seen as a kink in the distribution of number of measurements of high magnitude stars. The position of these features are used to determine the lower and upper magnitude bounds within which tertiary calibration stars are thought to be unbiased. We also include a minimum number of observations that excludes stars whose number of observations falls outside the bulk of the distribution.

The values for \hat{f}_{PSF} used in equation 5.15 are obtained by first computing lightcurves for the tertiary stars, then by averaging the values across time, thus obtaining a single value of flux for each star. The only cut applied during this averaging is a clipping of outliers beyond 3.5σ . Note that in assigning a single value of flux we are assuming that the stars are not variable. If the observed RMS of the light curve is beyond 2%, however, we conclude that this assumption is unwarranted and exclude this star when computing zero points. Recall also that, because they are computed after a flat field is applied, the saturation maps obtained are flawed (see section § 3.5.1). For this reason, it is entirely possible that the photometry of certain bright stars was computed on saturated pixels. Given that this severely skews the shape of the measured object, we expect a particularly large number of clipped pixels during the photometry. To this end, we exclude stars below a magnitude of 18 where more than one pixel per image has been clipped. Finally, when computing the zero point, we clip outliers beyond 3.5σ .

Examples of all of these cuts for a single zero point fit can be seen in figure B.1. In table B.2, we summarize the effect of each cut. The table details the fraction of measurements excluded by each cut, along with the corresponding shift in zero point.

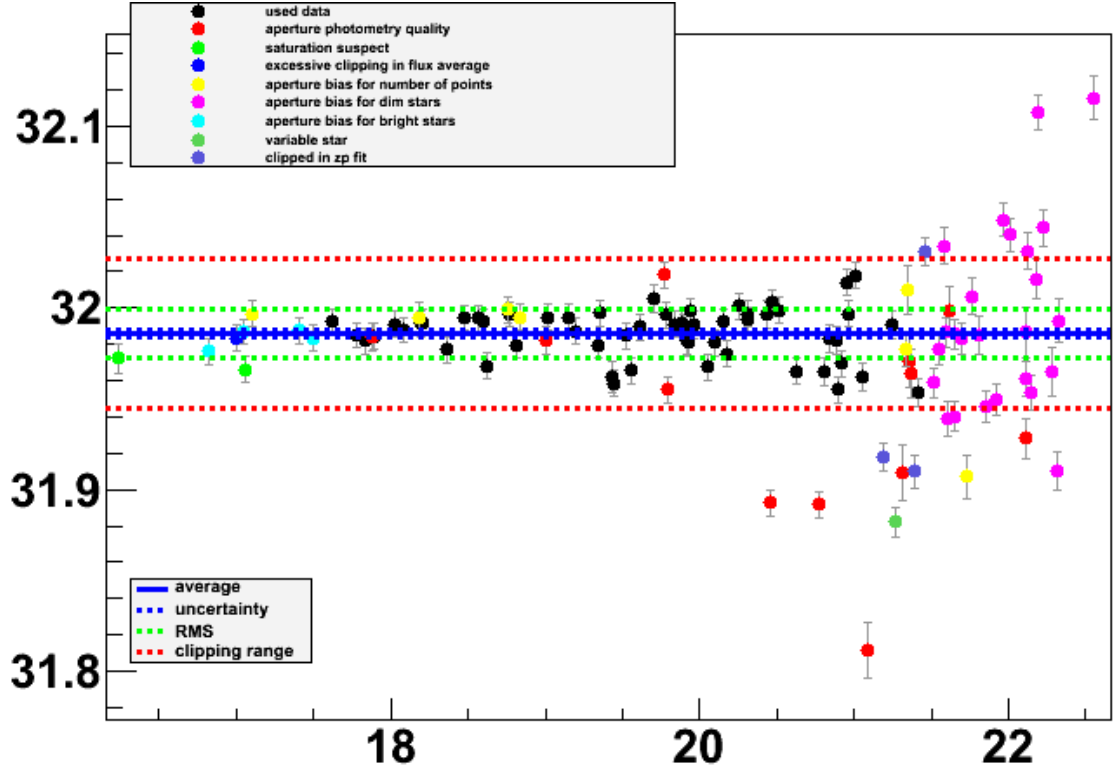


Figure B.1: Example of cuts for a single zero point fit.

Band	mag_{min}	mag_{max}	Minimum number of measurements
u	18.0	22.5	2
g	18.0	22.0	100
r	17.5	21.5	100
i	18.0	21.0	50
y	18.0	21.0	20
z	16.0	20.0	50

Table B.1: Description of aperture bias cuts. These are chosen by considering the patterns observed in figure B.2.

Rank	Description	Conditions	Ratio in g	r	i	y	z	δ_{zp} in g	r	i	y	z	figures
1	Cut for low quality aperture photometry	χ^2 greater than 5 in any band	6.96%	6.79%	6.56%	6.42%	6.8%	-0.83‰	-0.82‰	-0.69‰	0.22‰	-0.64‰	B.3 & B.4
2	Clip potentially un-flagged saturated stars	$mag < 18$ & more than 1 clipped pixel per image on average during psf photometry	0.6% 11.65%*	1.37% 13.43%*	2.71% 14.88%*	1.21% 8.98%*	1.33% 5.14%*	-0.03‰ -0.04‰ [†]	-0.07‰ -0.12‰ [†]	0.24‰ 0.08‰ [†]	0.09‰ -0.13‰ [†]	0.14‰ 0.13‰ [†]	B.5 & B.6
3	Excessive clipping during flux averaging	clipping in excess of 5%	2.26%	2.14%	2.44%	5.28%	3.09%	-0.3‰	-0.58‰	-0.19‰	-0.21‰	-0.18‰	B.7 & B.8
4	Aperture bias for stars with too few points	Described in table B.1	3.6%	2.32%	1.81%	3.07%	0.67%	-0.89‰	-0.38‰	-0.05‰	-0.12‰	-0.14‰	B.9 & B.10
5	Aperture bias for stars that are too dim	Described in table B.1	33.18%	27.34%	21.61%	21.36%	31.22%	-0.52‰	-0.97‰	-0.4‰	0.36‰	-1.19‰	B.11 & B.12
6	Aperture bias for stars that are too bright	Described in table B.1	4.83%	5.05%	10.93%	10.71%	0.65%	-0.01‰	-0.07‰	-0.13‰	-0.21‰	-0.01‰	B.13 & B.14
7	Variable stars	RMS in excess of 2% of flux	0.99%	0.52%	0.27%	0.11%	3.78%	-0.14‰	-0.13‰	-0.08‰	-0.01‰	-0.1‰	B.15 & B.16
8	Zero point clipping	3.5σ clipping during zero point averaging using the data point error bars	1.82%	2.18%	1.11%	1.14%	1.02%	-0.83‰	-0.84‰	-0.36‰	0.06‰	-0.21‰	B.17 & B.18

* The second row of ratios for the saturation cuts corresponds to the percentage of stars cut for which the residue is less than 2% in magnitude and of magnitude less than 18 *including bright stars cut for aperture bias*. This is an upper bound on the number of wrongly clipped stars.

† The second row of zero point shifts for saturation cuts corresponds to the shift *also including bright stars cut for aperture bias*. This is to quantify the effect of these stars should they remain unclipped and should the magnitude range used for zero point fitting come to include them.

Table B.2: Description of cuts on stars used during zero point fitting. We show the fraction of stars each cut eliminates as a percentage of the total sample. We also show the shift in zero point had it been computed excluding this cut. The referenced figures correspond to the distribution in magnitude of the cut stars, and their residues as a function of magnitude. The combination of all cuts can be seen in figure B.19. An example of these cuts for a single zero point fit can be seen in figure B.1

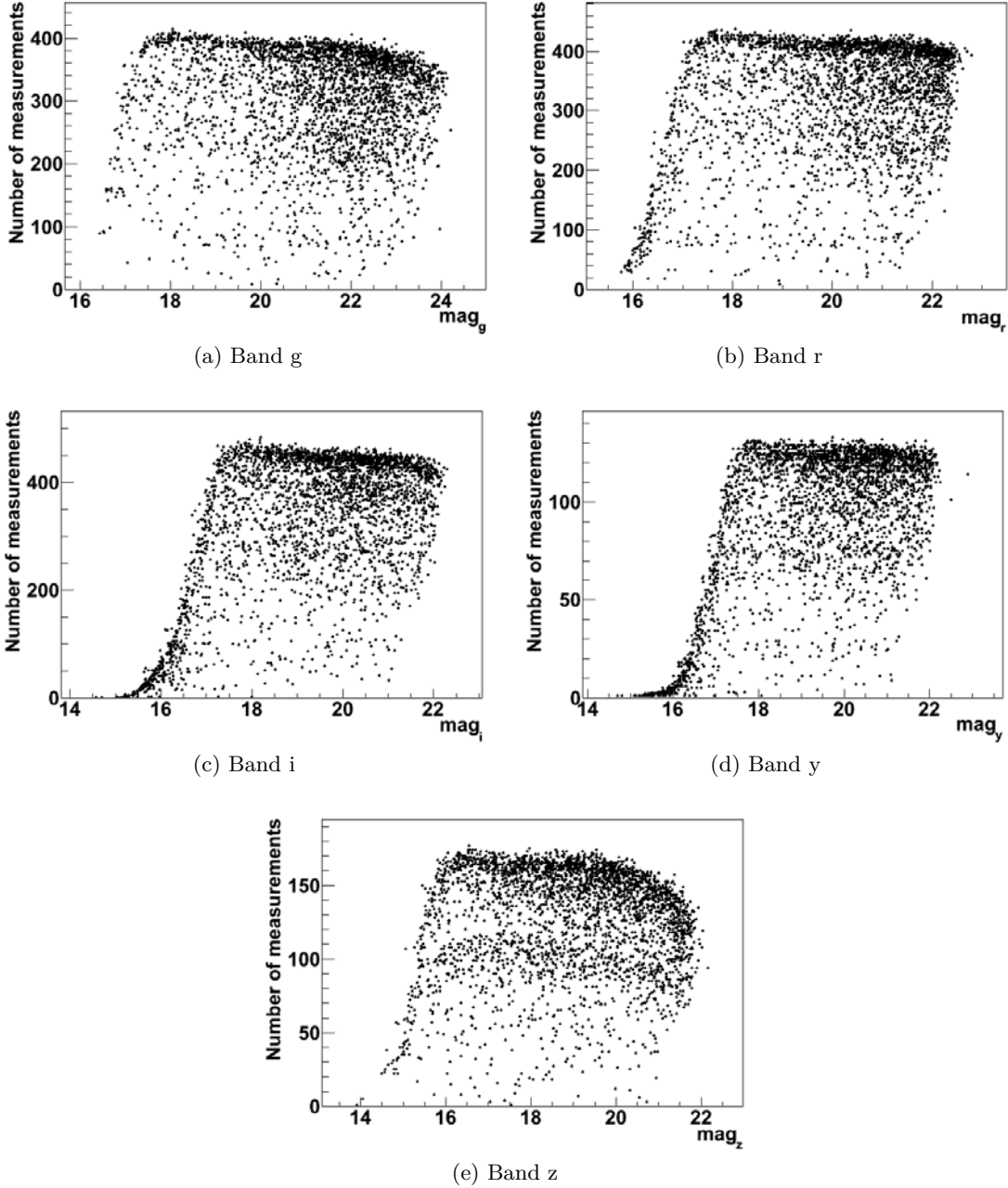


Figure B.2: Scatter plot of calibration stars for field D1

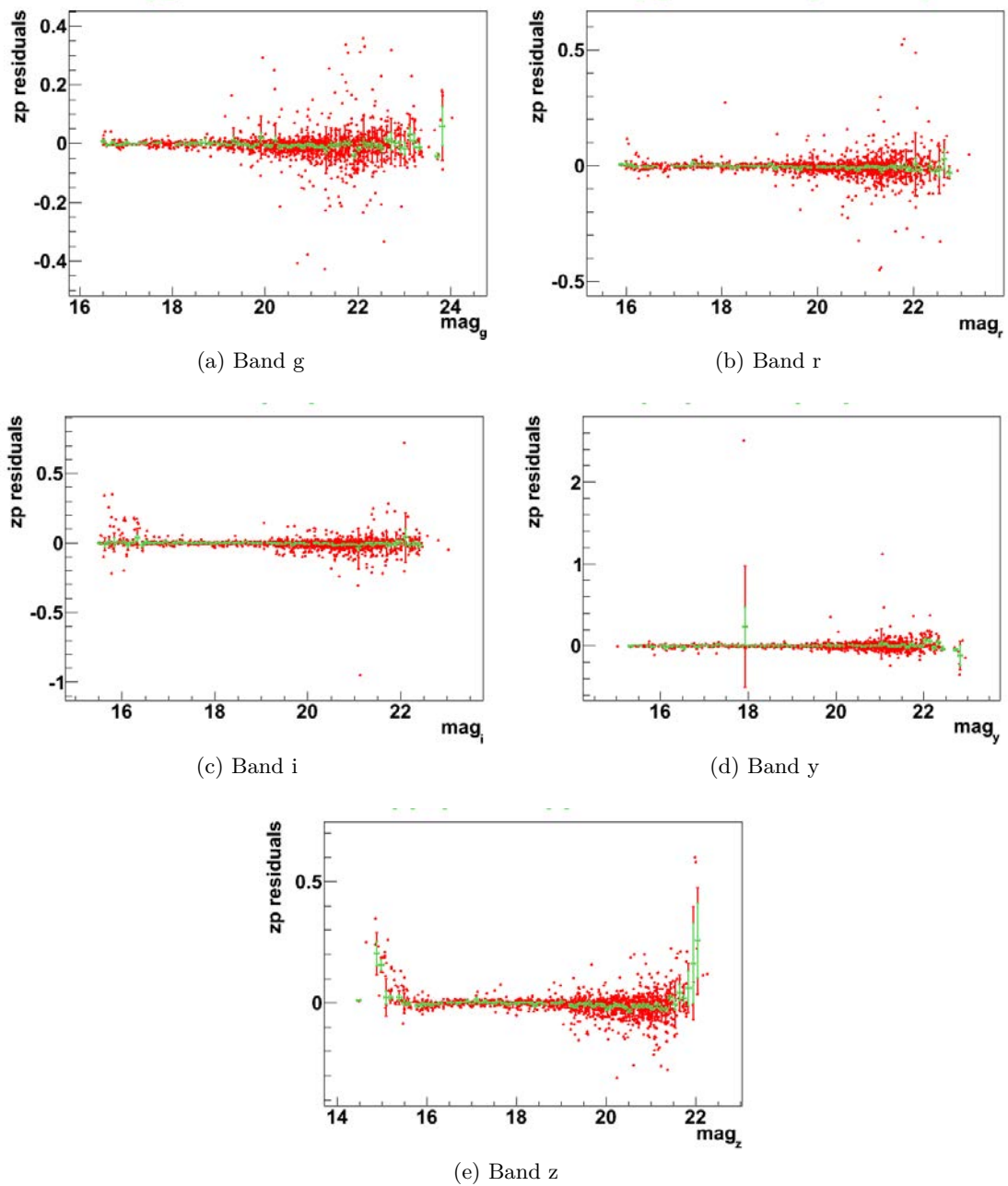


Figure B.3: Residuals of zero point for cut aperture photometry quality

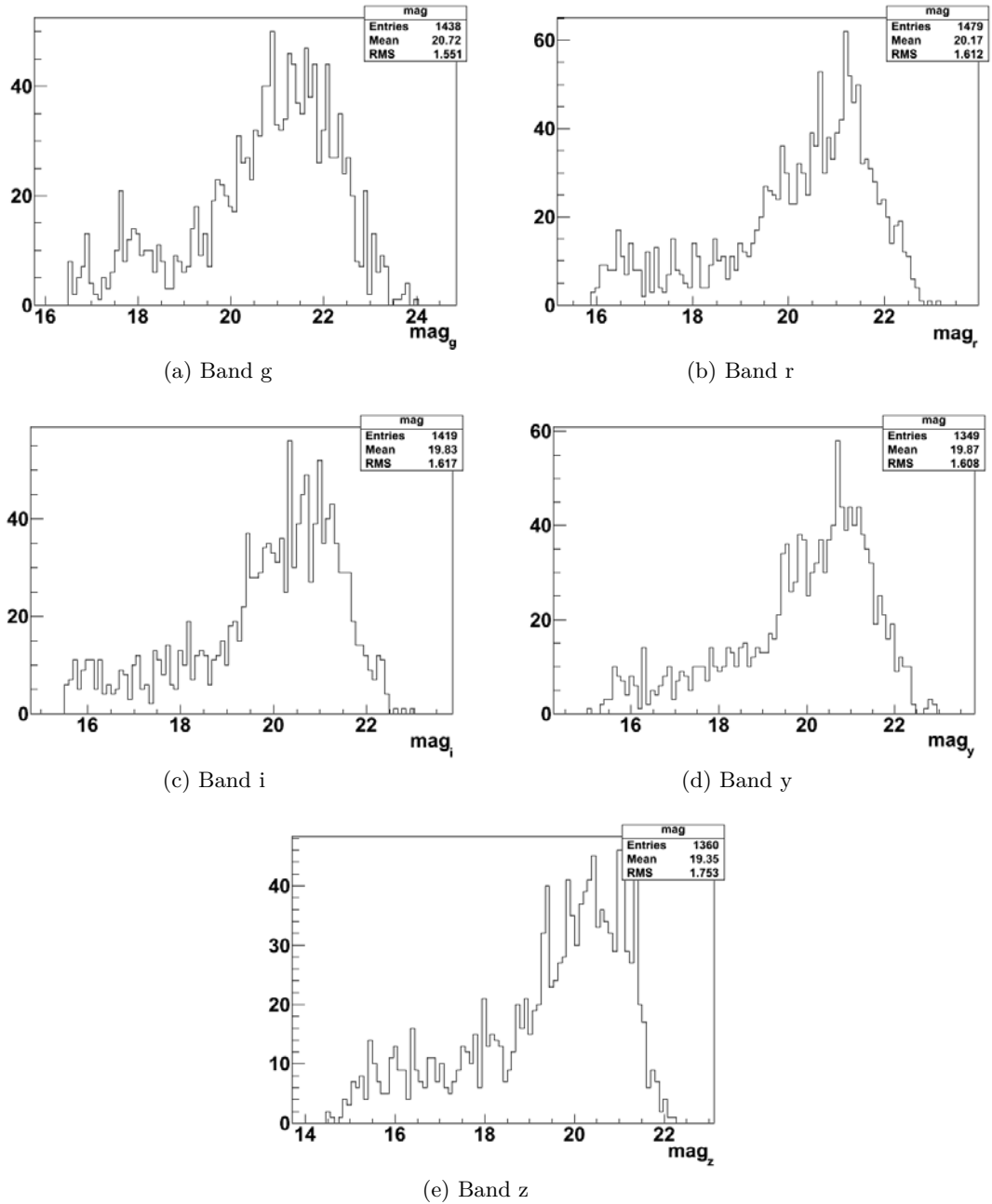


Figure B.4: Distribution in magnitude for cut aperture photometry quality

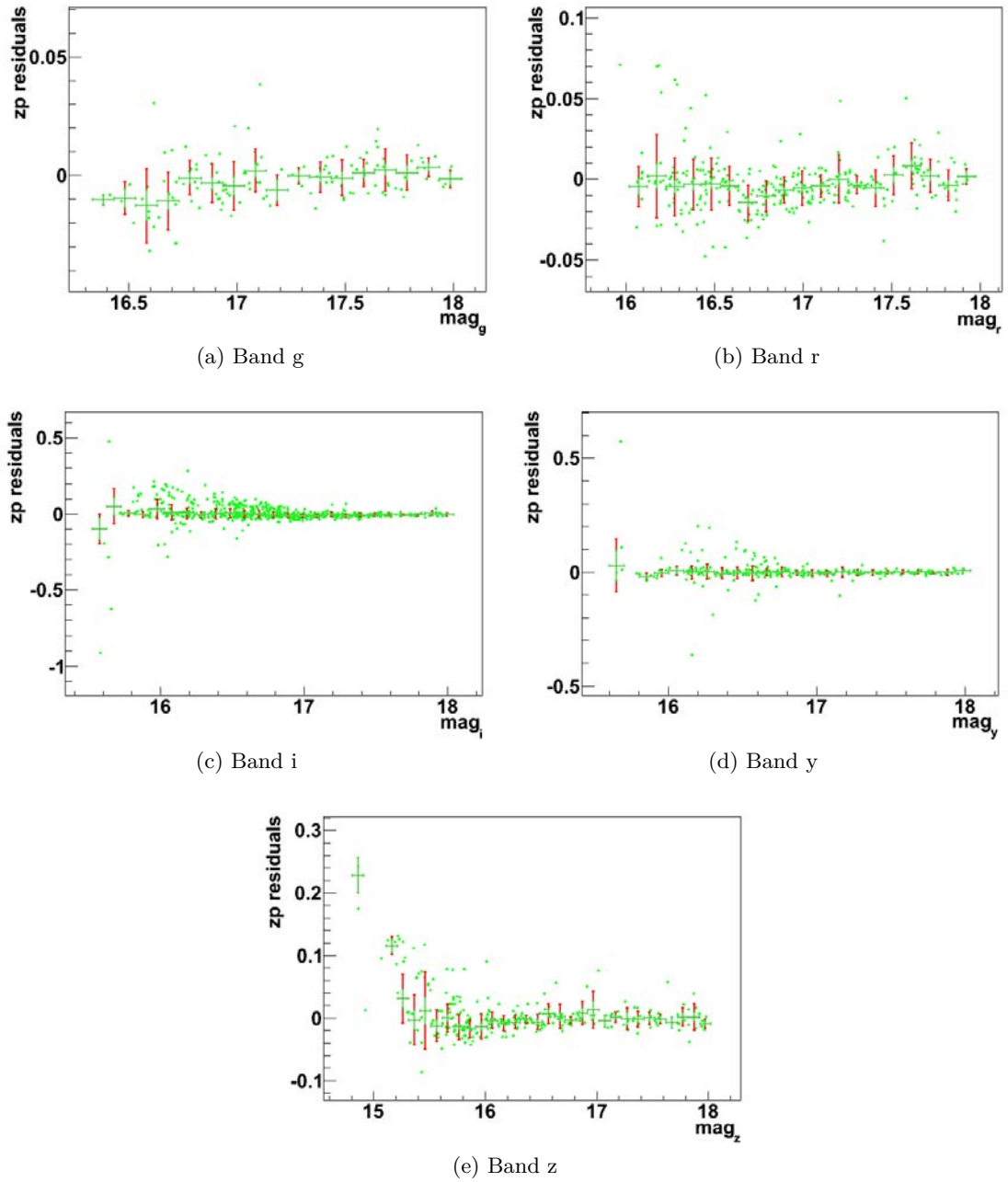
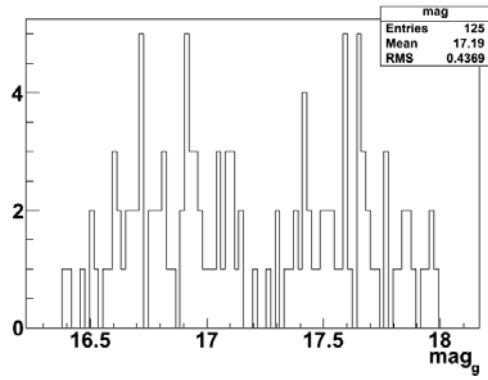
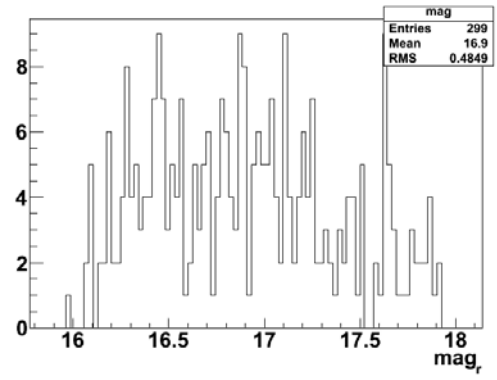


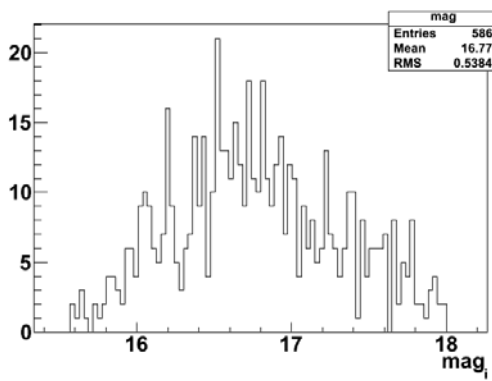
Figure B.5: Residuals of zero point for cut saturation suspect



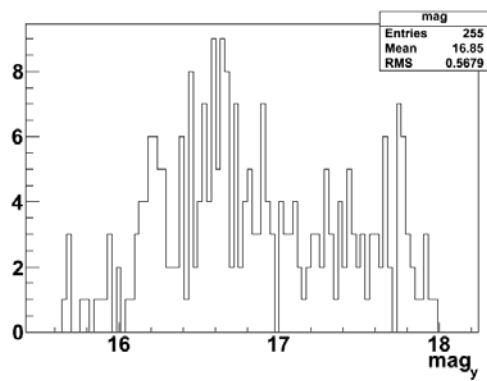
(a) Band g



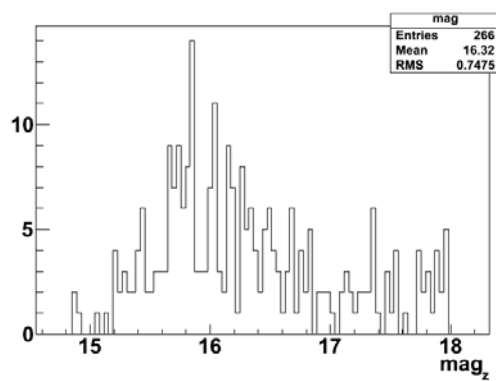
(b) Band r



(c) Band i



(d) Band y



(e) Band z

Figure B.6: Distribution in magnitude for cut saturation suspect

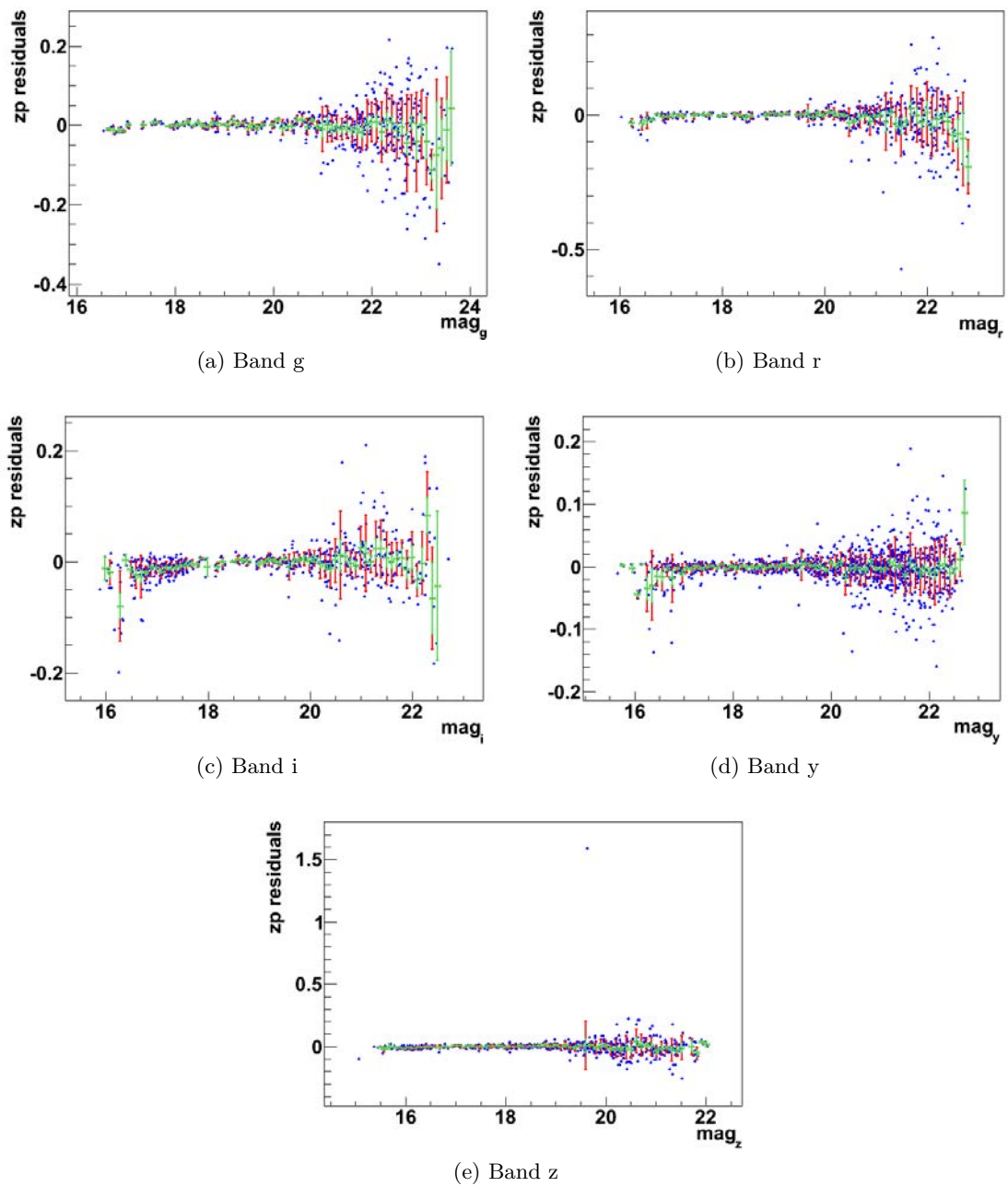


Figure B.7: Residuals of zero point for cut excessive clipping in flux average

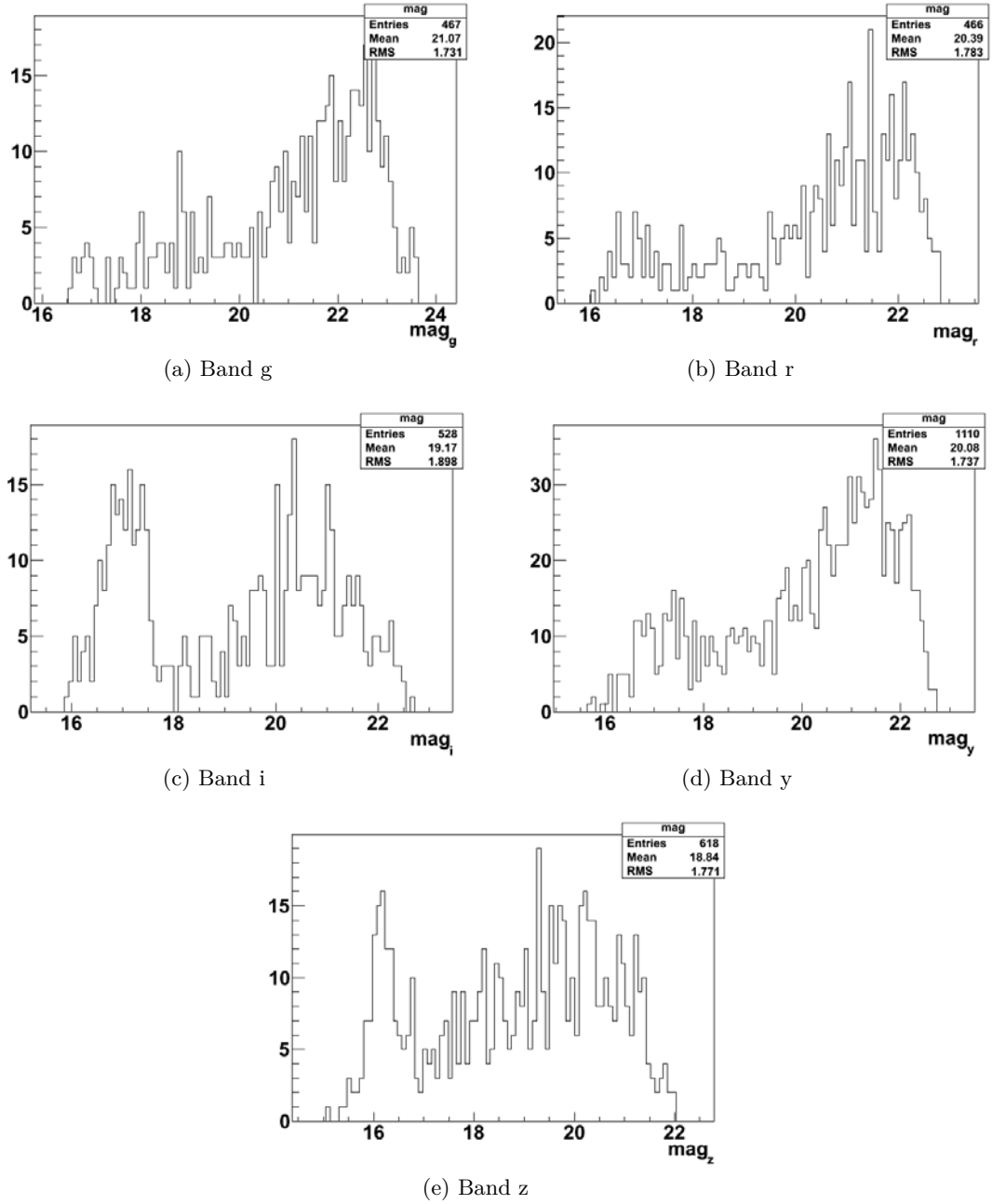


Figure B.8: Distribution in magnitude for cut excessive clipping in flux average

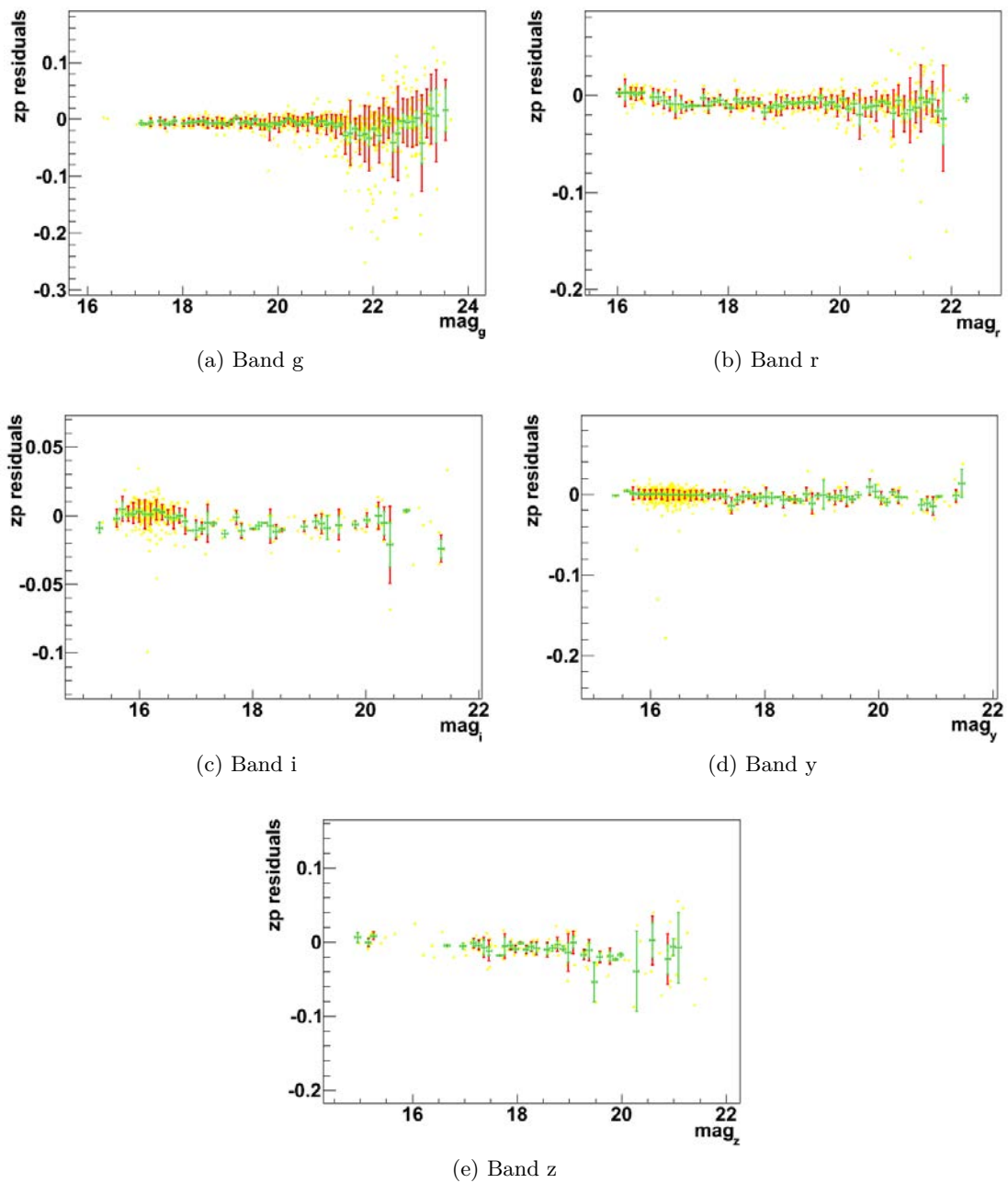
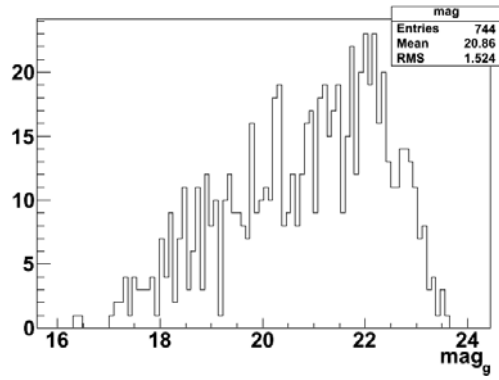
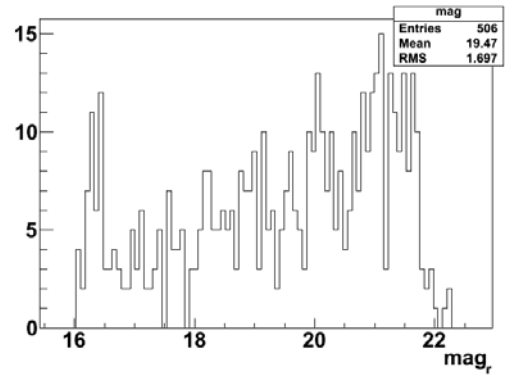


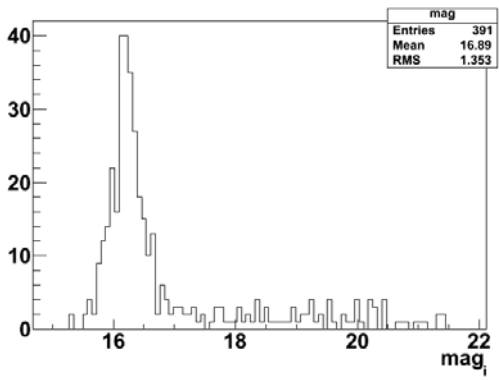
Figure B.9: Residuals of zero point for cut aperture bias points



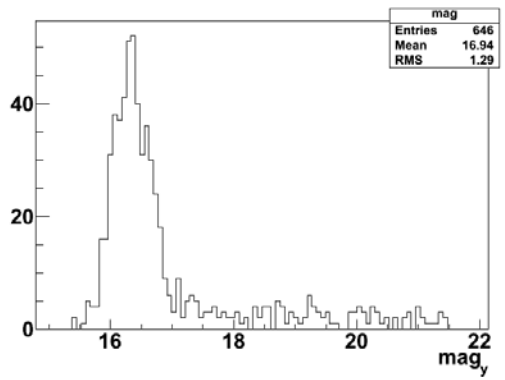
(a) Band g



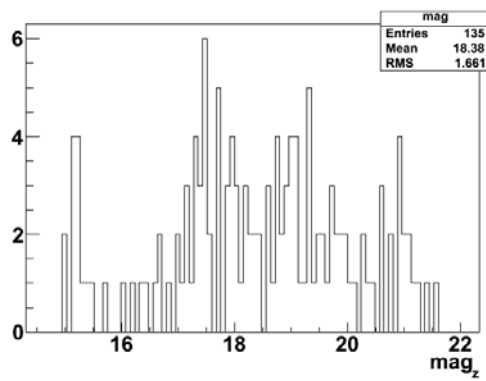
(b) Band r



(c) Band i



(d) Band y



(e) Band z

Figure B.10: Distribution in magnitude for cut aperture bias npoints

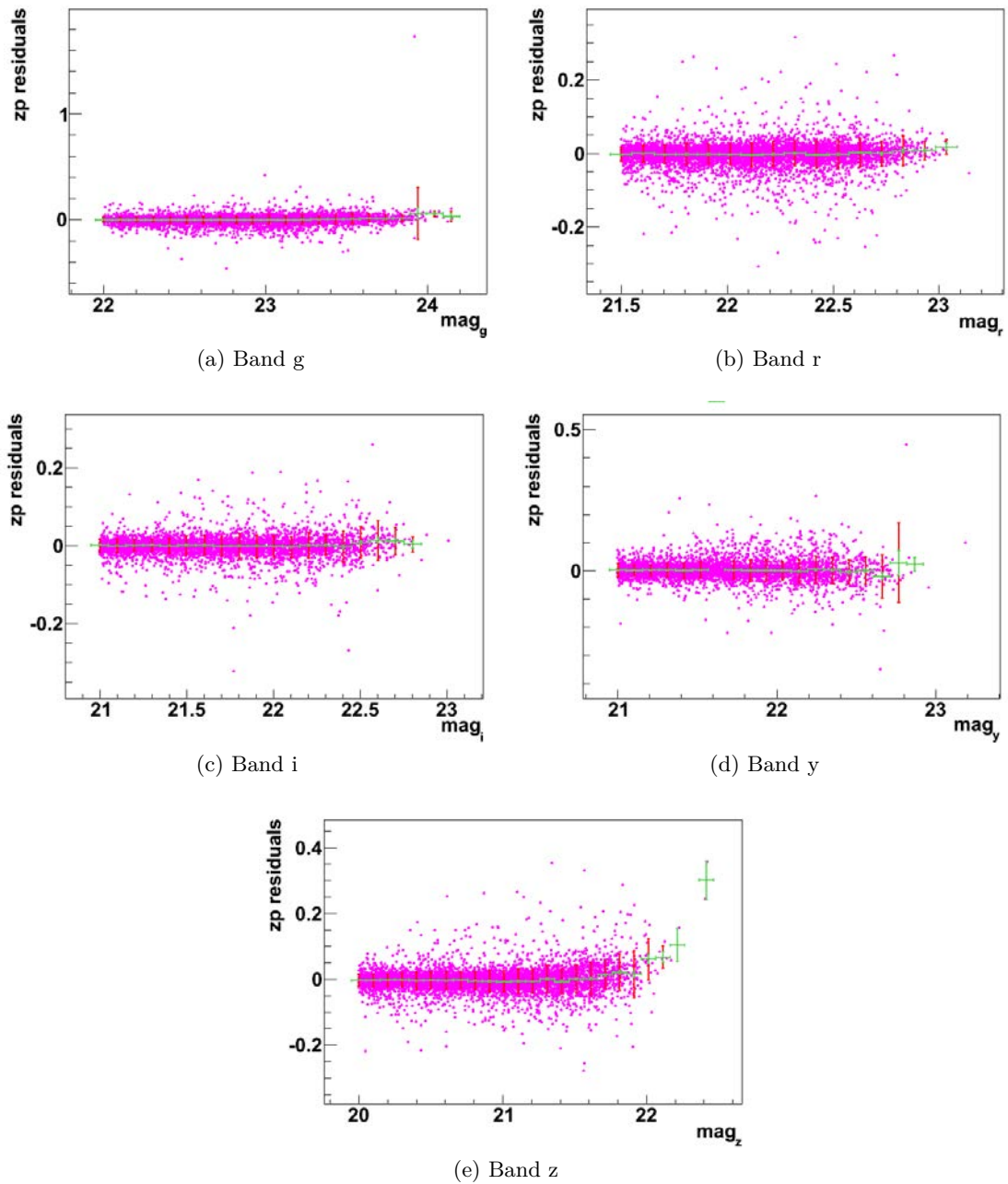
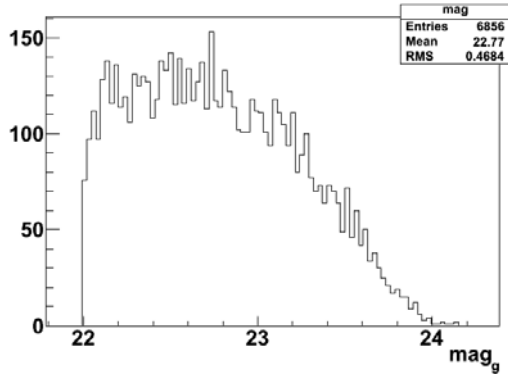
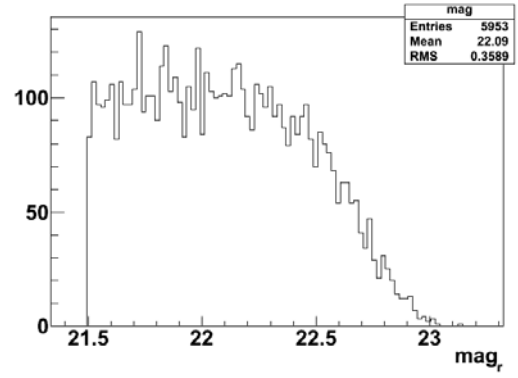


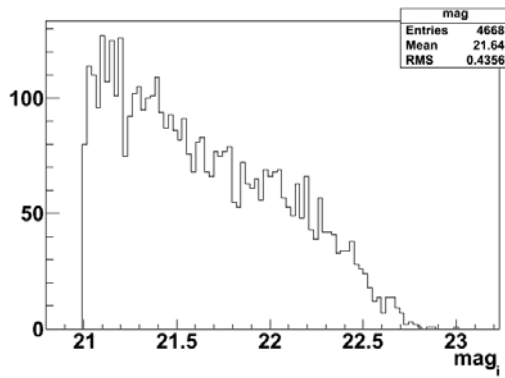
Figure B.11: Residuals of zero point for cut aperture bias dim



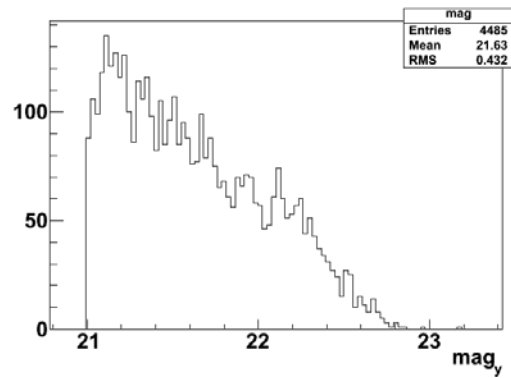
(a) Band g



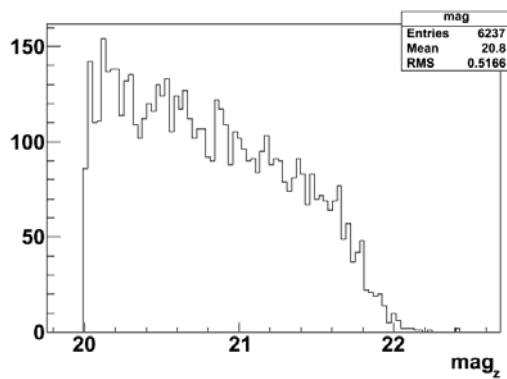
(b) Band r



(c) Band i



(d) Band y



(e) Band z

Figure B.12: Distribution in magnitude for cut aperture bias dim

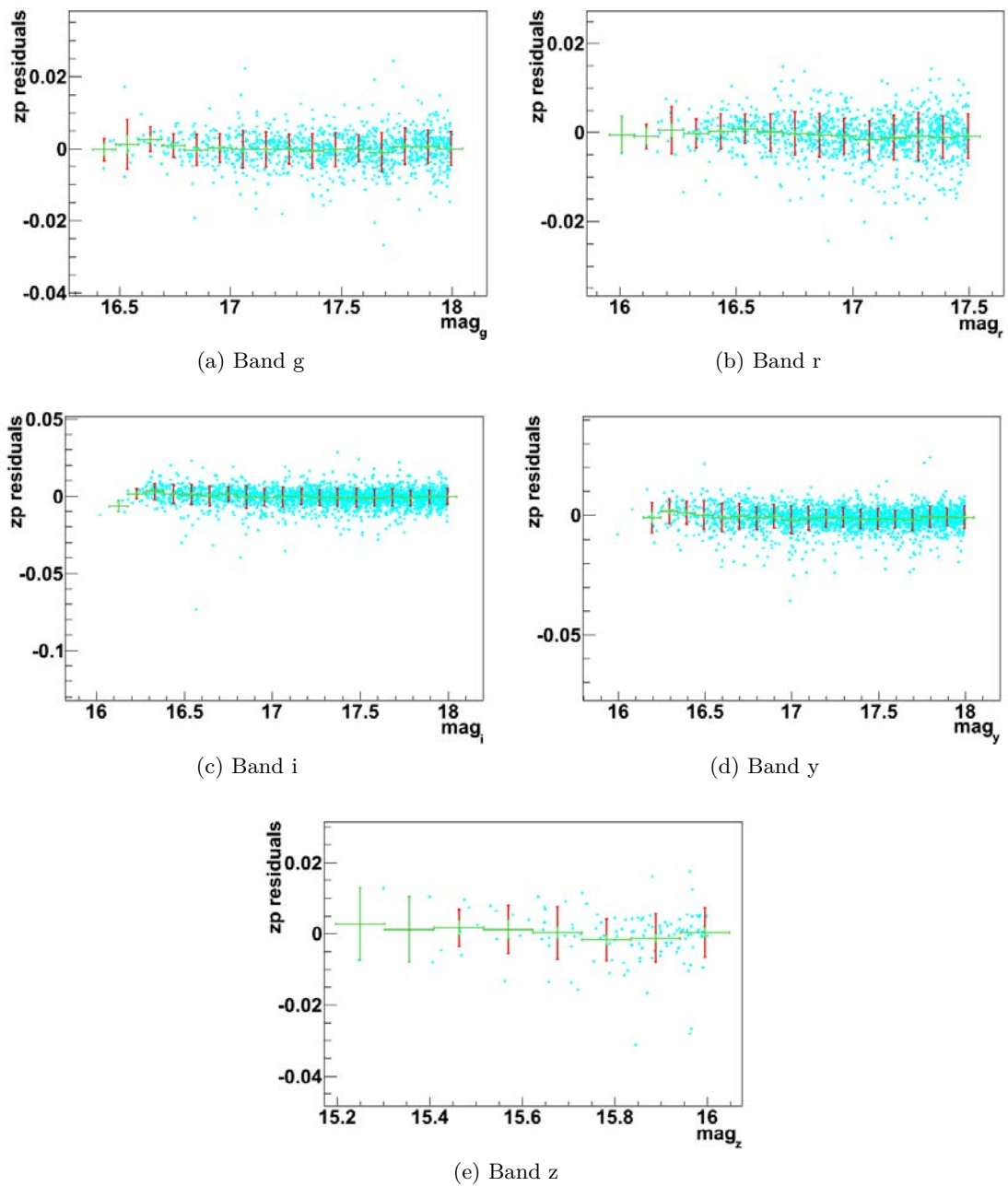


Figure B.13: Residuals of zero point for cut aperture bias bright

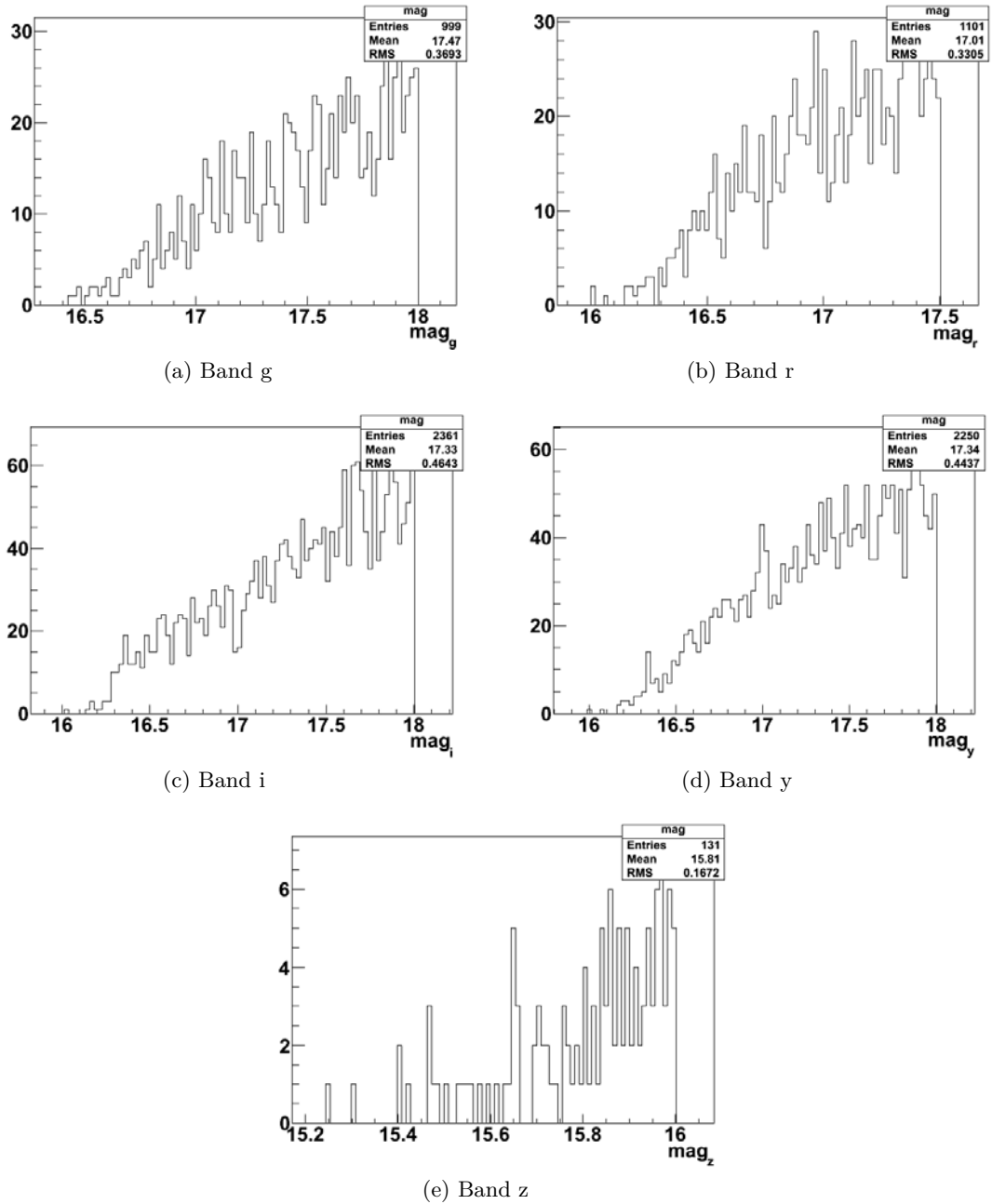


Figure B.14: Distribution in magnitude for cut aperture bias bright

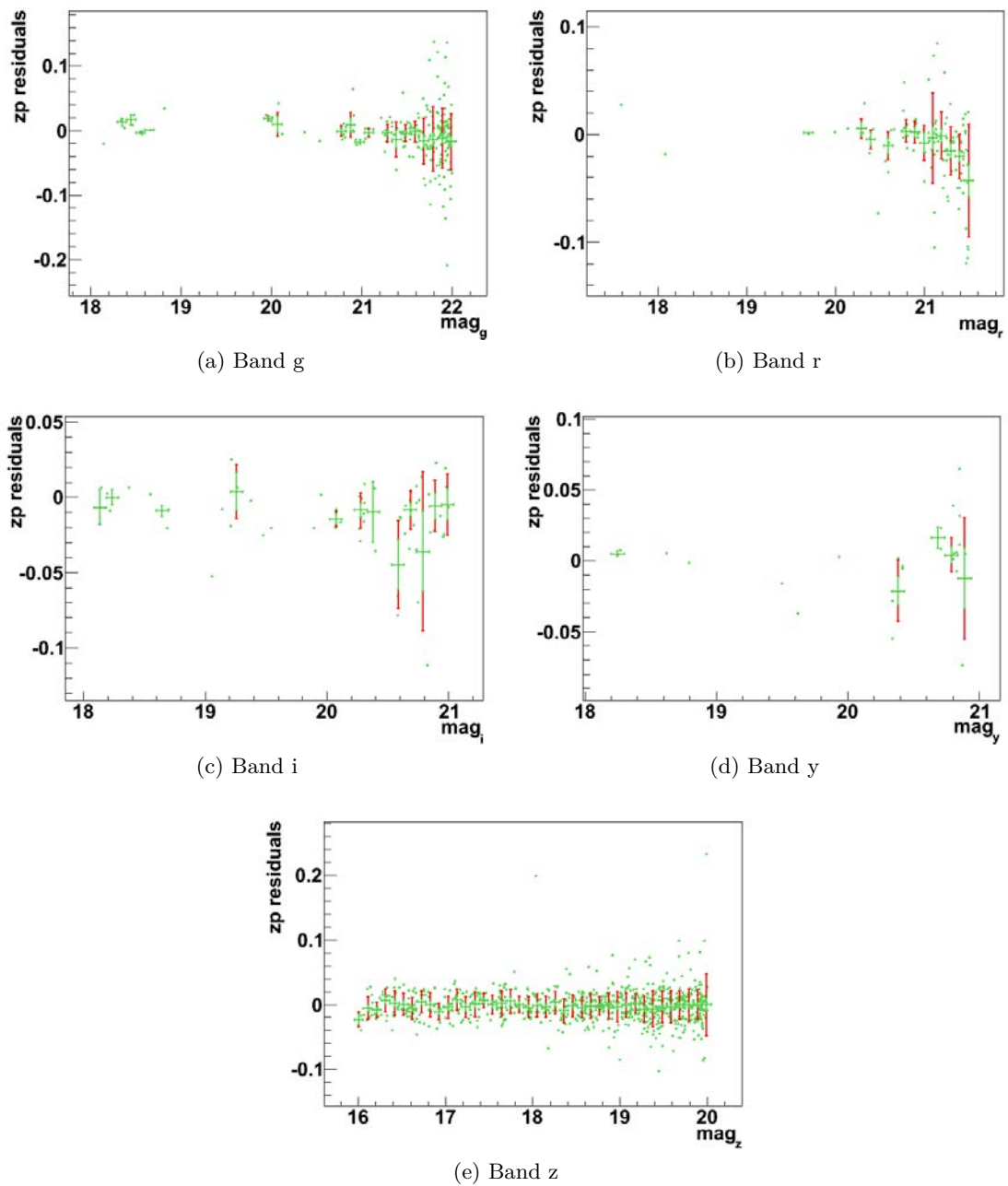


Figure B.15: Residuals of zero point for cut variable star

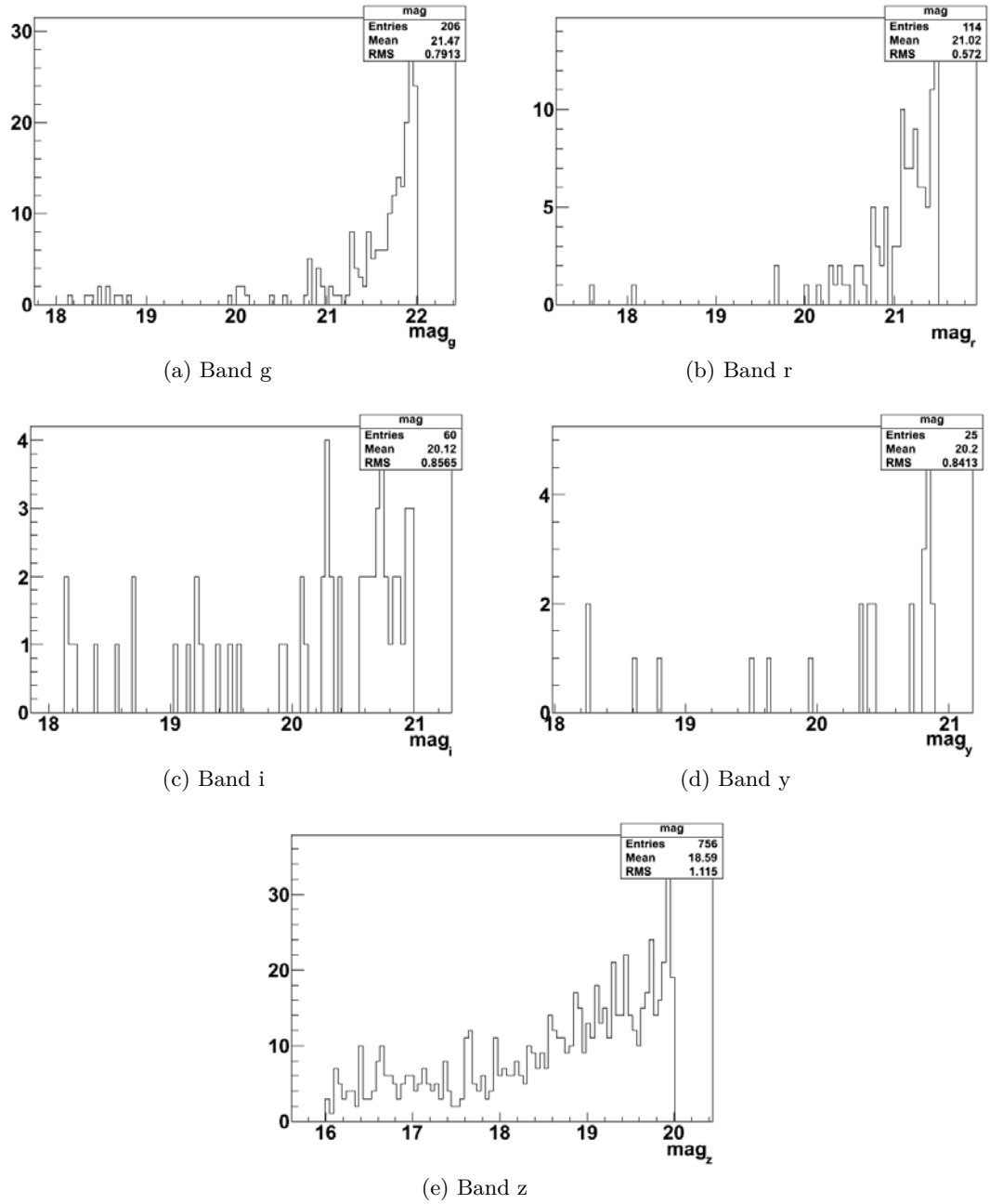


Figure B.16: Distribution in magnitude for cut variable star

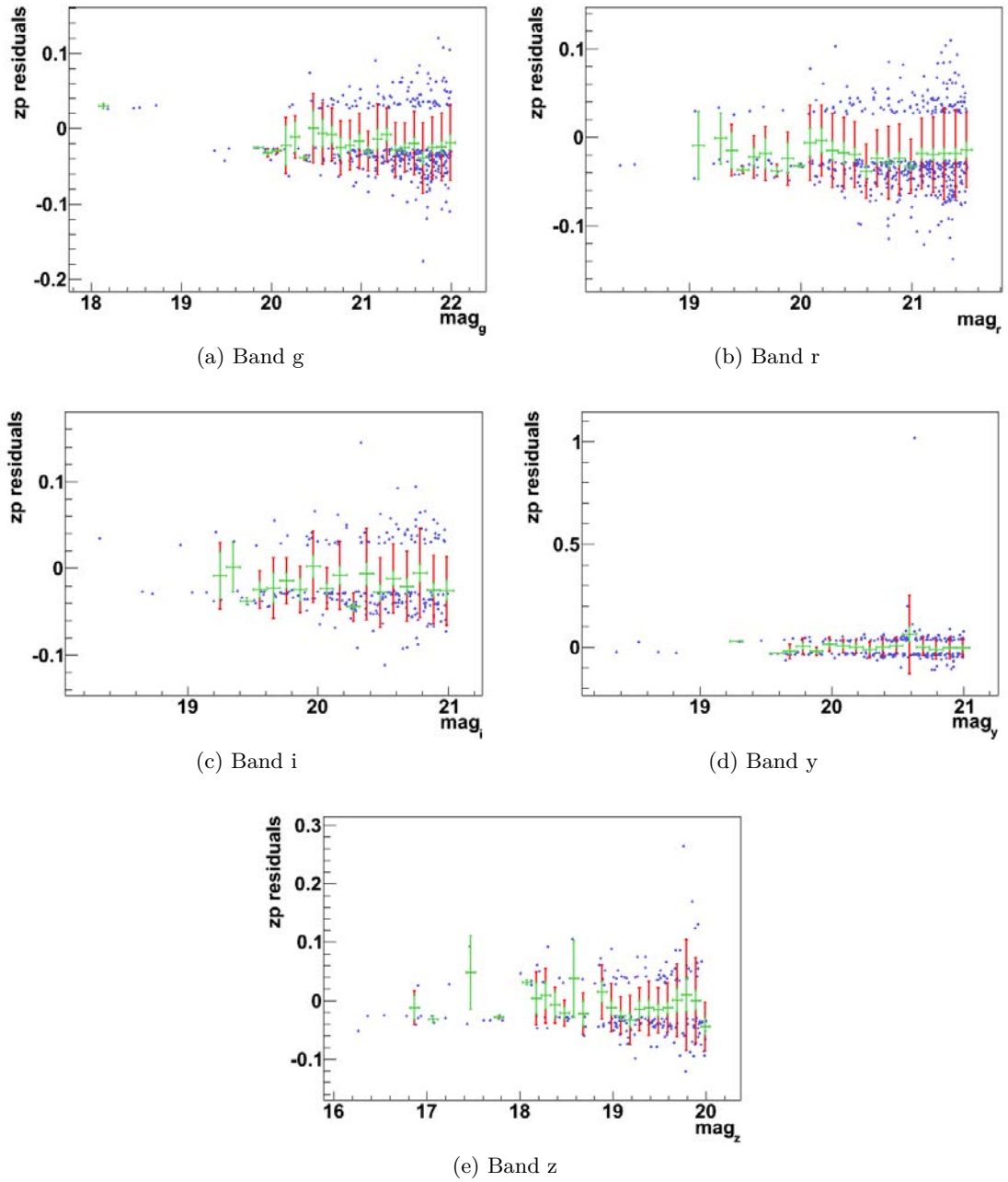


Figure B.17: Residuals of zero point for cut clipped in zp fit

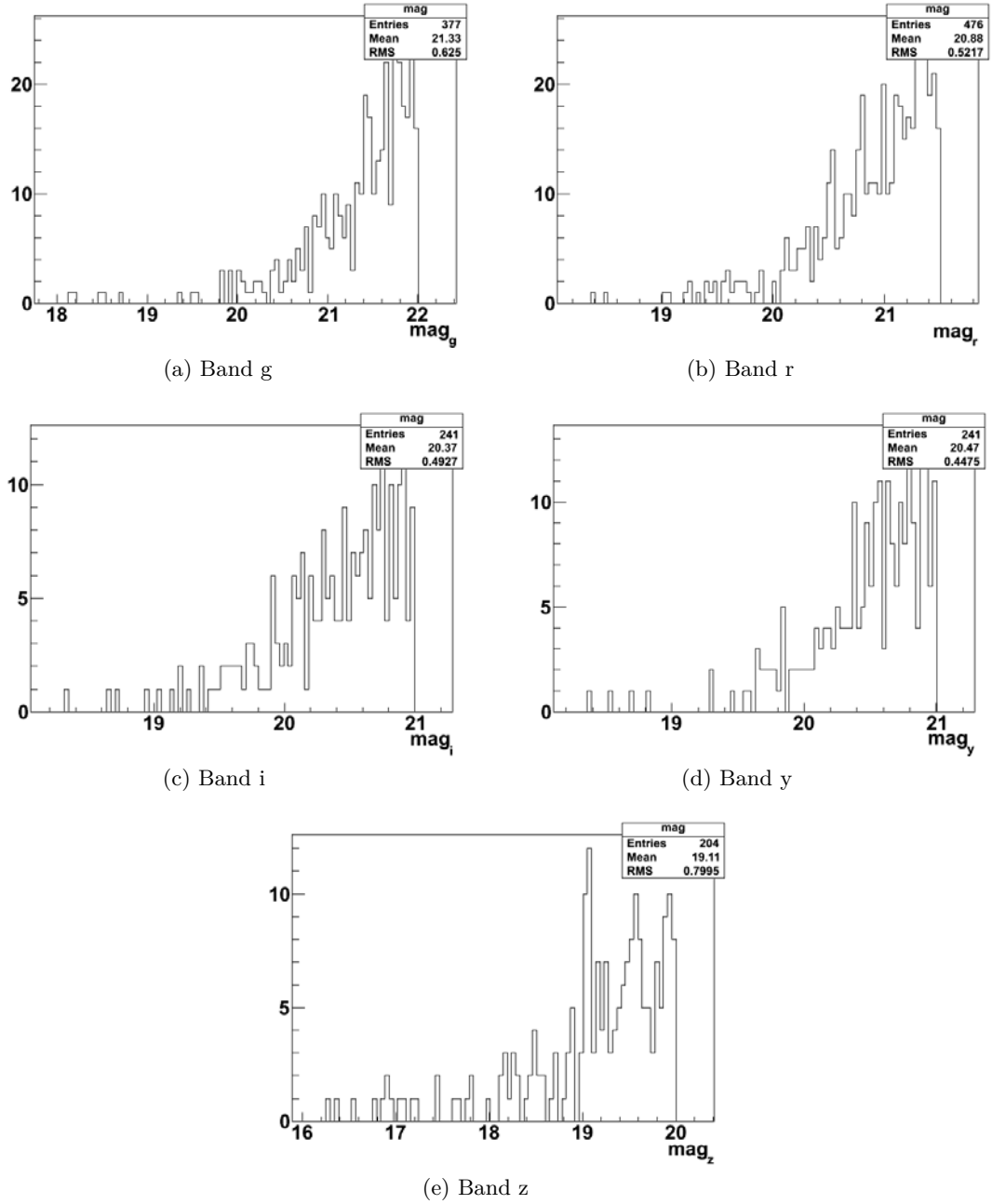


Figure B.18: Distribution in magnitude for cut clipped in zp fit

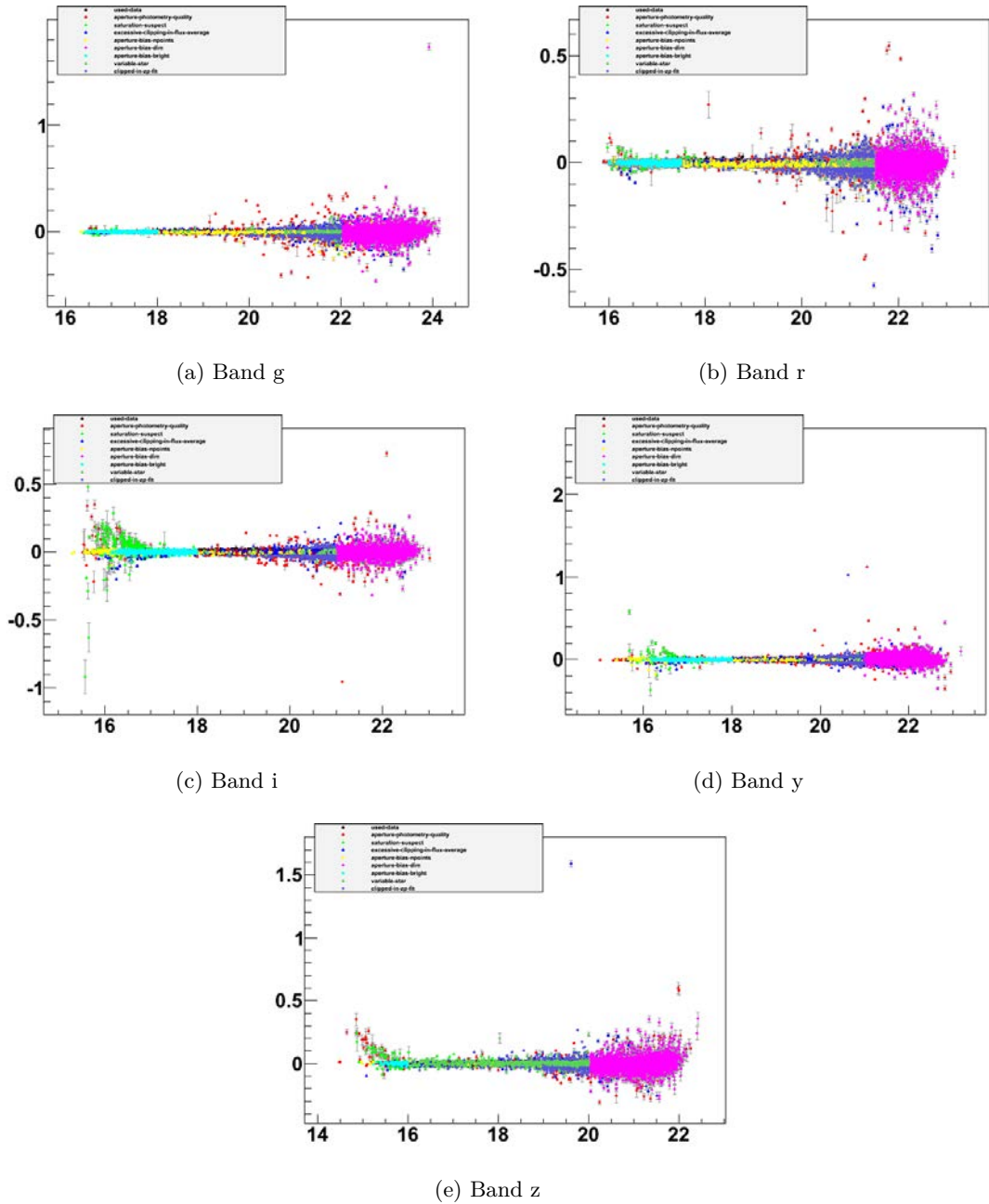


Figure B.19: Residuals of zero point for all cuts combined

Bibliography

- Alard, C. & Lupton, R. H. 1998, APJ, 503, 325
- Altavilla, G., Fiorentino, G., Marconi, M., et al. 2004, MNRAS, 349, 1344
- Anderson, L., Aubourg, E., Bailey, S., et al. 2012, MNRAS, 427, 3435
- Astier, P. 2012, ArXiv e-prints
- Astier, P., El Hage, P., Guy, J., et al. 2013, AAP, 557, A55
- Astier, P., Guy, J., Pain, R., & Balland, C. 2011, AAP, 525, A7
- Astier, P., Guy, J., Regnault, N., et al. 2006, AAP, 447, 31
- Bailey, S., Aldering, G., Antilogus, P., et al. 2009, AAP, 500, L17
- Balland, C. 2013, MÃ©moire d'habilitation Ã diriger des recherches : Spectroscopie des Supernovae Ia distantes pour la cosmologie
- Balland, C., Baumont, S., Basa, S., et al. 2009, AAP, 507, 85
- Barbon, R., Benetti, S., Rosino, L., Cappellaro, E., & Turatto, M. 1990, AAP, 237, 79
- Bazin, G., Ruhlmann-Kleider, V., Palanque-Delabrouille, N., et al. 2011, AAP, 534, A43
- Bell, E. F., McIntosh, D. H., Katz, N., & Weinberg, M. D. 2003, APJS, 149, 289
- Bertin, E. & Arnouts, S. 1996, AAPS, 117, 393
- Betoule, M., Kessler, R., Guy, J., et al. 2014, AAP, 568, A22
- Betoule, M., Murriner, J., Regnault, N., et al. 2013, AAP, 552, A124
- Beutler, F., Blake, C., Colless, M., et al. 2011, MNRAS, 416, 3017
- Blondin, S., Matheson, T., Kirshner, R. P., et al. 2012, AJ, 143, 126
- Branch, D., Lacy, C. H., McCall, M. L., et al. 1983, APJ, 270, 123
- Bronder, T. J., Hook, I. M., Astier, P., et al. 2008, AAP, 477, 717
- Brown, H. R. 2003, Michelson, FitzGerald and Lorentz: the origins of relativity revisited
- Buton, C., Copin, Y., Aldering, G., et al. 2013, AAP, 549, A8

Bibliography

- Calabretta, M. & Greisen, E. W. 2000, in *Astronomical Society of the Pacific Conference Series*, Vol. 216, *Astronomical Data Analysis Software and Systems IX*, ed. N. Manset, C. Veillet, & D. Crabtree, 571
- Cardelli, J. A., Clayton, G. C., & Mathis, J. S. 1989, *APJ*, 345, 245
- Cellier-Holzem, F. 2013, PhD thesis, *Particules, Noyaux, Cosmologie (ED 517)*
- Chandrasekhar, S. 1931, *APJ*, 74, 81
- Childress, M., Aldering, G., Antilogus, P., et al. 2013, *APJ*, 770, 108
- Chotard, N., Gangler, E., Aldering, G., et al. 2011, *AAP*, 529, L4
- Conley, A., Guy, J., Sullivan, M., et al. 2011, *APJS*, 192, 1
- D'Andrea, C. B., Gupta, R. R., Sako, M., et al. 2011, *APJ*, 743, 172
- Daniel Kasen's webpage. , "<http://www.ucolick.org/~kasen>"
- Davis, T. M., Hui, L., Frieman, J. A., et al. 2011, *APJ*, 741, 67
- Einstein, A. 1905, *Annalen der Physik*, 322, 891
- Einstein, A. 1915, *Sitzungsberichte der Königlich Preußischen Akademie der Wissenschaften (Berlin)*, Seite 844-847., 844
- Einstein, A. 1917, *Sitzungsberichte der Königlich Preußischen Akademie der Wissenschaften (Berlin)*, Seite 142-152., 142
- Eisenstein, D. J. & Hu, W. 1998, *APJ*, 496, 605
- Ellis, R. S., Sullivan, M., Nugent, P. E., et al. 2008, *APJ*, 674, 51
- Filippenko, A. V. 1997, *Annual Review of Astronomy and Astrophysics*, 35, 309
- Filippenko, A. V., Richmond, M. W., Branch, D., et al. 1992a, *AJ*, 104, 1543
- Filippenko, A. V., Richmond, M. W., Matheson, T., et al. 1992b, *APJL*, 384, L15
- Fioc, M. & Rocca-Volmerange, B. 1997, *AAP*, 326, 950
- Fioc, M. & Rocca-Volmerange, B. 1999, *ArXiv Astrophysics e-prints*
- Fix, M., Smith, J., Tucker, D. L., Wester, W., & DES. 2014, in *American Astronomical Society Meeting Abstracts*, Vol. 223, *American Astronomical Society Meeting Abstracts 223*, 254.14
- Folatelli, G., Morrell, N., Phillips, M. M., et al. 2013, *APJ*, 773, 53
- Foley, R. J., Challis, P. J., Chornock, R., et al. 2013, *APJ*, 767, 57
- Foley, R. J., Chornock, R., Filippenko, A. V., et al. 2009, *AJ*, 138, 376
- Friedmann, A. 1922, *Zeitschrift für Physik*, 10, 377
- Fukugita, M., Ichikawa, T., Gunn, J. E., et al. 1996, *AJ*, 111, 1748

- Glazebrook, K. & Bland-Hawthorn, J. 2001, *PASP*, 113, 197
- Gunn, J. E. & Stryker, L. L. 1983, *APJS*, 52, 121
- Gupta, R. R., D'Andrea, C. B., Sako, M., et al. 2011, *APJ*, 741, 127
- Guy, J., Astier, P., Baumont, S., et al. 2007, *AAP*, 466, 11
- Guy, J., Astier, P., Nobili, S., Regnault, N., & Pain, R. 2005, *AAP*, 443, 781
- Guy, J., Sullivan, M., Conley, A., et al. 2010, *AAP*, 523, A7
- Guyonnet, A. 2012, PhD thesis, Particules, Noyaux, Cosmologie (ED 517)
- Hamuy, M., Phillips, M. M., Suntzeff, N. B., et al. 1996, *AJ*, 112, 2408
- Hardin, D. 2015
- Hildebrandt, H. & on behalf of the CFHTLenS collaboration. 2014, ArXiv e-prints
- Holtzman, J. A., Marriner, J., Kessler, R., et al. 2008, *AJ*, 136, 2306
- Hook, I. M., Jørgensen, I., Allington-Smith, J. R., et al. 2004, *PASP*, 116, 425
- Howell, D. A., Sullivan, M., Brown, E. F., et al. 2009, *APJ*, 691, 661
- Howell, D. A., Sullivan, M., Nugent, P. E., et al. 2006, *NAT*, 443, 308
- Howell, D. A., Sullivan, M., Perrett, K., et al. 2005, *APJ*, 634, 1190
- Hoyle, F. & Fowler, W. A. 1960, *APJ*, 132, 565
- Hsiao, E. Y., Conley, A., Howell, D. A., et al. 2007, *APJ*, 663, 1187
- Hubble, E. 1929, *Proceedings of the National Academy of Science*, 15, 168
- Hui, L. & Greene, P. B. 2006, *PRD*, 73, 123526
- Humphrey, P. J., Liu, W., & Buote, D. A. 2009, *APJ*, 693, 822
- Iben, Jr., I. & Tutukov, A. V. 1984, *APJS*, 54, 335
- Jha, S., Kirshner, R. P., Challis, P., et al. 2006, *AJ*, 131, 527
- Johansson, J., Thomas, D., Pforr, J., et al. 2013, *MNRAS*, 435, 1680
- Jönsson, J., Sullivan, M., Hook, I., et al. 2010, *MNRAS*, 405, 535
- Kamionkowski, M. 1998, in *High Energy Physics and Cosmology, 1997 Summer School*, ed. E. Gava, A. Masiero, K. S. Narain, S. Randjbar-Daemi, G. Senjanovic, A. Smirnov, & Q. Shafi, 394
- Kasen, D. 2006, *APJ*, 649, 939
- Kelly, P. L., Hicken, M., Burke, D. L., Mandel, K. S., & Kirshner, R. P. 2010, *APJ*, 715, 743
- Kessler, R., Bernstein, J. P., Cinabro, D., et al. 2009, *PASP*, 121, 1028

Bibliography

- Kessler, R., Guy, J., Marriner, J., et al. 2013, APJ, 764, 48
- Khoury, J. 2013, *Classical and Quantum Gravity*, 30, 214004
- Kirshner, R. P., Jeffery, D. J., Leibundgut, B., et al. 1993, APJ, 415, 589
- Komatsu, E., Smith, K. M., Dunkley, J., et al. 2011, APJS, 192, 18
- Kronborg, T., Hardin, D., Guy, J., et al. 2010, AAP, 514, A44
- Lampeitl, H., Smith, M., Nichol, R. C., et al. 2010, APJ, 722, 566
- Landolt, A. U. 1992, AJ, 104, 340
- Laureijs, R., Amiaux, J., Arduini, S., et al. 2011, ArXiv e-prints
- Lavaux, G. & Hudson, M. J. 2011, MNRAS, 416, 2840
- Li, W., Bloom, J. S., Podsiadlowski, P., et al. 2011, NAT, 480, 348
- Li, W., Filippenko, A. V., Chornock, R., et al. 2003, PASP, 115, 453
- Li, W., Filippenko, A. V., Gates, E., et al. 2001a, PASP, 113, 1178
- Li, W., Filippenko, A. V., Treffers, R. R., et al. 2001b, APJ, 546, 734
- Lidman, C., Ruhlmann-Kleider, V., Sullivan, M., et al. 2013, PASA, 30, 1
- Livio, M. 2000, in *Type Ia Supernovae, Theory and Cosmology*, ed. J. C. Niemeyer & J. W. Truran, 33
- LSST Science Collaboration, Abell, P. A., Allison, J., et al. 2009, ArXiv e-prints
- Magnier, E. A. & Cuillandre, J.-C. 2004, PASP, 116, 449
- Maoz, D. & Mannucci, F. 2008, MNRAS, 388, 421
- Martin, J. 2012, *Comptes Rendus Physique*, 13, 566
- Matheson, T., Kirshner, R. P., Challis, P., et al. 2008, AJ, 135, 1598
- Mazure, A., Adami, C., Pierre, M., et al. 2007, AAP, 467, 49
- Mazzali, P. A., Chugai, N., Turatto, M., et al. 1997, MNRAS, 284, 151
- Mazzali, P. A., Danziger, I. J., & Turatto, M. 1995, AAP, 297, 509
- Moffat, A. F. J. 1969, AAP, 3, 455
- Mosher, J., Guy, J., Kessler, R., et al. 2014, APJ, 793, 16
- Neill, J. D., Sullivan, M., Howell, D. A., et al. 2009, APJ, 707, 1449
- Newton, I. 1760, *Philosophiae naturalis principia mathematica*, vol. 1 - 4
- Nordin, J., Östman, L., Goobar, A., et al. 2011, APJ, 734, 42
- observer statistics of MegaPrime observations. , "<http://www.cfht.hawaii.edu/Instruments/Imaging/MegaPrime>

-
- Padmanabhan, N., Xu, X., Eisenstein, D. J., et al. 2012, MNRAS, 427, 2132
- Pan, Y.-C., Sullivan, M., Maguire, K., et al. 2014, MNRAS, 438, 1391
- Patat, F., Benetti, S., Cappellaro, E., et al. 1996, MNRAS, 278, 111
- Penzias, A. A. & Wilson, R. W. 1965, APJ, 142, 419
- Perlmutter, S., Aldering, G., Goldhaber, G., et al. 1999, APJ, 517, 565
- Petit, J.-M., Kavelaars, J. J., Gladman, B. J., et al. 2011, AJ, 142, 131
- Phillips, M. M., Li, W., Frieman, J. A., et al. 2007, PASP, 119, 360
- Pickles, A. J. 1998, VizieR Online Data Catalog, 611, 863
- Pike, R. W. & Hudson, M. J. 2005, APJ, 635, 11
- Planck Collaboration, Ade, P. A. R., Aghanim, N., et al. 2013a, ArXiv e-prints
- Planck Collaboration, Ade, P. A. R., Aghanim, N., et al. 2013b, ArXiv e-prints
- Regnault, N., Conley, A., Guy, J., et al. 2009, AAP, 506, 999
- Riess, A. G., Filippenko, A. V., Challis, P., et al. 1998, AJ, 116, 1009
- Riess, A. G., Kirshner, R. P., Schmidt, B. P., et al. 1999, AJ, 117, 707
- Riess, A. G., Strolger, L.-G., Casertano, S., et al. 2007, APJ, 659, 98
- Rigault, M., Copin, Y., Aldering, G., et al. 2013, AAP, 560, A66
- Roukema, B. F., Ostrowski, J. J., & Buchert, T. 2013, JCAP, 10, 43
- Rubin, V. C., Thonnard, N., & Ford, Jr., W. K. 1978, APJL, 225, L107
- Sachs, R. K. & Wolfe, A. M. 1967, APJ, 147, 73
- Sako, M., Bassett, B., Becker, A. C., et al. 2014, ArXiv e-prints
- Sako, M., Bassett, B., Connolly, B., et al. 2011, APJ, 738, 162
- Schaefer, B. E. & Pagnotta, A. 2012, NAT, 481, 164
- Schlafly, E. F. & Finkbeiner, D. P. 2011, APJ, 737, 103
- Schlegel, D. J., Finkbeiner, D. P., & Davis, M. 1998, APJ, 500, 525
- Schmidt, B. P., Suntzeff, N. B., Phillips, M. M., et al. 1998, APJ, 507, 46
- Semboloni, E., Mellier, Y., van Waerbeke, L., et al. 2006, AAP, 452, 51
- Sesar, B., Jurić, M., & Ivezić, Ž. 2011, APJ, 731, 4
- Skrutskie, M. F., Cutri, R. M., Stiening, R., et al. 2006, AJ, 131, 1163
- Smoot, G. F., Bennett, C. L., Kogut, A., et al. 1992, APJL, 396, L1

Bibliography

Springob, C. M., Masters, K. L., Haynes, M. P., Giovanelli, R., & Marinoni, C. 2009, APJS, 182, 474

Stetson, P. B. 1987, PASP, 99, 191

Stritzinger, M. D., Phillips, M. M., Boldt, L. N., et al. 2011, AJ, 142, 156

Sullivan, M., Conley, A., Howell, D. A., et al. 2010, MNRAS, 406, 782

Sullivan, M., Guy, J., Conley, A., et al. 2011, APJ, 737, 102

Suzuki, N., Rubin, D., Lidman, C., et al. 2012, APJ, 746, 85

Terapix. , "<http://terapix.iap.fr/cplt/T0007/doc/T0007-doc.html>"

the CFHTLS paper repository. , "<http://www.cfht.hawaii.edu/Science/CFHLS/cfhtlspublications.html>"

the CFHTLS website. , "<http://www.cfht.hawaii.edu/Instruments/Imaging/MegaPrime/megaprimecomponents>"

Turnbull, S. J., Hudson, M. J., Feldman, H. A., et al. 2012, MNRAS, 420, 447

van den Bergh, S. 1999, PASP, 111, 657

Villa, F. 2012, PhD thesis, Particules, Noyaux, Cosmologie (ED 517)

Walker, E. S., Hook, I. M., Sullivan, M., et al. 2011, MNRAS, 410, 1262

Webbink, R. F. 1984, APJ, 277, 355

Weinberg, S. 1989, Reviews of Modern Physics, 61, 1

Will, C. M. 2006, Living Reviews in Relativity, 9

Yoo, J. & Watanabe, Y. 2012, International Journal of Modern Physics D, 21, 30002

Résumé : L'un des plus grands défis de la cosmologie moderne est d'expliquer l'accélération de l'expansion de l'univers dans son histoire récente. La découverte de cette accélération s'est faite grâce à des mesures de supernovae, ces dernières restant les sondes les plus puissantes pour caractériser cette accélération. Cette thèse vise à présenter l'analyse finale du **Supernova Legacy Survey** (SNLS) qui sera publiée en 2015. Nous commençons par présenter les fondements théoriques de la cosmologie moderne, en nous focalisant en particulier sur les défis théoriques que présente cette accélération. Nous introduisons ensuite les **supernovae de type Ia** (SNIa) et justifions leur usage en tant que sonde cosmologique. Par la suite, nous donnons un aperçu global de l'expérience SNLS. Nous abordons alors les aspects techniques de l'analyse. Nous commençons par l'exploration du processus de **photométrie**, utilisé pour la mesure des supernovae. Nous détaillons alors la nouvelle méthode de photométrie implémentée par SNLS qui évite le rééchantillonnage des images. Nous explorons aussi les simulations mise en oeuvre dans le but de garantir la linéarité de la méthode au dessous de 1%. Nous explorons ensuite la procédure de calibration associée à ces mesures utilisant des étoiles de champ dont la précision de calibration atteint les 3.5%. Enfin, nous terminons avec une description détaillée de la mise en oeuvre de tous les outils présentés, afin d'extraire des paramètres cosmologiques des données. Afin d'estimer la capacité de SNLS à contraindre les paramètres cosmologiques, nous contruisons un diagramme de Hubble grâce à une analyse préliminaire des données incluant 960 supernovae, dont 450 provenant du SNLS. La combinaison de ce diagramme de Hubble avec des contraintes apportées d'autres sondes cosmologiques mène à une incertitude sur le paramètre de l'équation d'état de l'énergie noire de 0.048, la mesure la plus précise jusqu'à nos jours.

Mots-clés : Cosmologie, Énergie Noire, Supernovae de Type Ia, SNLS, Photométrie, K-Corrections

Abstract: A significant open question of modern cosmology is explaining the accelerated expansion of the universe in late times. The discovery of this acceleration was made using supernova measurements, which continue to be the most significant probe with which to characterize this acceleration. This thesis concerns itself with presenting the final analysis of the **Supernova Legacy Survey** (SNLS) which will be published in 2015. We begin by presenting the theoretical foundations of modern cosmology, with special emphasis on the challenges presented by acceleration. We then introduce **type Ia supernovae** (SNIa) and motivate their use as probes of cosmic expansion. Afterwards, we give an overview of the SNLS experiment. We then move on to the technical aspects of the analysis that was carried out. We start by exploring the process of **photometry**, with which supernova measurements are made. Here we look at the newly implemented photometry method that avoids resampling images. We also explore simulations aimed at ensuring the method's linearity up to less than 1%. We then explain the calibration process associated with these measurements using field stars calibrated up to the 3.5% level. Finally, we end with an in depth look at the cosmology analysis itself, which utilizes all the tools we have explored to extract cosmological parameters from the data. To estimate the constraining power of the SNLS experiment, we undertake a preliminary analysis of the data by constructing a Hubble diagram using 960 supernovae, of which 450 come from the SNLS. Combining this Hubble diagram with constraints from other cosmological probes leads to an uncertainty on the equation of state parameter of **dark energy** of 0.048, its most precise constraint to date.

Key words: Cosmology, Dark Energy, Type Ia Supernovae, SNLS, Photometry, K-Corrections
